

## 9. SITE 1081<sup>1</sup>

### Shipboard Scientific Party<sup>2</sup>

#### HOLE 1081A

**Position:** 19°37.1818'S, 11°19.1598'E

**Start hole:** 0200 hr, 9 September 1997

**End hole:** 2115 hr, 11 September 1997

**Time on hole:** 67.25 hr

**Seafloor (drill pipe measurement from rig floor, mbrf):** 805.5

**Total depth (drill pipe measurement from rig floor, mbrf):** 1258.2

**Distance between rig floor and sea level (m):** 11.4

**Water depth (drill pipe measurement from sea level, m):** 794.1

**Penetration (mbsf):** 452.7

**Coring totals:**

Type: APC

Number: 17

Cored: 145.50 m

Recovered: 151.18 m (103.90%)

Type: XCB

Number: 32

Cored: 307.20 m

Recovered: 242.30 m (78.87%)

**Lithology:**

Unit I (0–390 mbsf): clay with varying amounts of diatoms, nannofossils, foraminifers, and radiolarians

Unit II (390–452.7 mbsf): clayey nannofossil ooze

#### HOLE 1081B

**Position:** 19°37.1981'S, 11°19.1588'E

**Start hole:** 2115 hr, 11 September 1997

**End hole:** 0925 hr, 12 September 1997

**Time on hole:** 12.17 hr

**Seafloor (drill pipe measurement from rig floor, mbrf):** 804.5

**Total depth (drill pipe measurement from rig floor, mbrf):** 992.1

**Distance between rig floor and sea level (m):** 11.4

**Water depth (drill pipe measurement from sea level, m):** 793.1

**Penetration (mbsf):** 187.6

**Coring totals:**

Type: APC

Number: 21

Cored: 187.6 m

Recovered: 195.87 m (104.41%)

**Lithology:**

Unit I: clay with varying amounts of diatoms, nannofossils, foraminifers, and radiolarians

#### HOLE 1081C

**Position:** 19°37.2128'S, 11°19.1620'E

**Start hole:** 0925 hr, 12 September 1997

**End hole:** 2015 hr, 12 September 1997

**Time on hole:** 10.83 hr

**Seafloor (drill pipe measurement from rig floor, mbrf):** 805.2

**Total depth (drill pipe measurement from rig floor, mbrf):** 960.4

**Distance between rig floor and sea level (m):** 11.4

**Water depth (drill pipe measurement from sea level, m):** 793.8

**Penetration (mbsf):** 155.2

**Coring totals:**

Type: APC

Number: 17

Cored: 155.2 m

Recovered: 160.94 m (103.7%)

**Lithology:**

Unit I: clay with varying amounts of diatoms, nannofossils, foraminifers, and radiolarians

**Principal results:** Three holes were cored with the advanced hydraulic piston corer/extended core barrel (APC/XCB) at Site 1081 to a maximum depth of 452.7 meters below seafloor (mbsf), which recovered an apparently continuous hemipelagic sedimentary section spanning the Holocene to upper Miocene (0–9 Ma). Hole 1081A was cored with the APC to 134.0 mbsf and extended with the XCB to a depth of 452.7 mbsf. At Hole 1081B, 21 cores were taken with the APC to 187.6 mbsf. Hole 1081C was cored with the APC to 155.2 mbsf. Detailed comparisons between the magnetic susceptibility and the gamma-ray attenuation porosity evaluator (GRAPE) density records generated on the multisensor track (MST) demonstrated complete recovery of the sedimentary sequence down to 215 meters composite depth (mcd).

Sediments from Site 1081 consist of two lithostratigraphic units. Unit I is composed of olive-gray to black clays that contain varying amounts of diatoms, nannofossils, foraminifers, and radiolarians. Three subunits are defined based on the various abundances and types of microfossils in the sediments: nannofossil- and foraminifer-rich clay (0–77 mbsf), diatom-rich clay (77–230 mbsf), and nannofossil-rich clay (230–390 mbsf). Lithostratigraphic Unit II (390–452 mbsf) is composed of olive-gray clayey nannofossil ooze. The detrital component of the sediments is clay with rare silt-sized, angular and subangular, mono- and polycrystalline quartz grains, feldspar, and mica. Muscovite and biotite are also present in trace amounts. The biogenic component is represented by varying abundances of foraminifers, nannofossils, and diatoms. Varying amounts of particulate organic matter were observed. Authigenic minerals, such as glauconite, rare framboidal pyrite, and dolomite, were observed. Sedimentation rates are fairly constant within the upper Miocene and lower

<sup>1</sup>Wefer, G., Berger, W.H., Richter, C., et al., 1998. *Proc. ODP, Init. Repts.*, 175: College Station, TX (Ocean Drilling Program).

<sup>2</sup>Shipboard Scientific Party is given in the list preceding the Table of Contents.

Pliocene (40 m/m.y.) sequences. Sedimentation rates within the upper Pliocene sequence are the highest recorded at this site (90–150 m/m.y.) but are reduced at the Pliocene/Pleistocene boundary (70 m/m.y.).

Fine biostratigraphic resolution was achieved by integrating datums from all microfossil groups. All microfossil groups, except for planktonic foraminifers, show marked coeval fluctuations in abundance, which are reflected in the lithology. Planktonic foraminifers are barren, rare, or replaced by pyrite from 105 mbsf to the bottom of the hole. Calcareous nanofossils are abundant and well preserved within the upper (0–77 mbsf) and lower (147–452 mbsf) parts of the section. Samples between 77 and 147 mbsf are commonly barren or poor in calcareous nanofossils, although some nanofossil-rich sediments are occasionally found within short intervals. The biostratigraphy of the Neogene is poorly constrained because of the scarcity of index species. Diatom abundance shows a substantial increase in upper Pliocene and lower Pleistocene sediments and reaches a maximum in the upper Pliocene interval, whereas overall abundance levels remain low in upper Miocene and lower Pliocene sediments. This pattern resembles that of Deep Sea Drilling Project (DSDP) Site 532. The diatom assemblage consists of a mixture of upwelling-related and oceanic species. Upwelling-related species dominate the diatom assemblage during highest abundance times in the upper Pliocene interval. They are not common in lower Pliocene and Miocene sediments where oceanic species tend to dominate. The diatom content in the sediments possibly reflects a varying nutrient supply that could be related to upwelling of nutrient-rich deeper waters and high biological productivity over the Walvis Ridge, especially in the late Pliocene.

After alternating-field (AF) demagnetization at 20 mT, a complete magnetostratigraphy was determined in the uppermost 120 mbsf of the APC section at Site 1081. All chrons from the Brunhes (C1n) to the termination of the Olduvai (C2n) at 1.77 Ma could be identified.

Well-developed nanofossil ooze-clay cycles, in which concentrations of calcium carbonate and organic carbon vary between 1 and 53 wt% and between 1.4 and 8.2 wt%, respectively, reflect fluctuations in the elevated marine production associated with the Benguela Current. Higher concentrations of organic carbon from 0 to 200 mbsf record higher productivities during the last 2 m.y. than earlier in the history of this upwelling system. The interstitial water chemical profiles at this deeply drilled site record a relatively shallow (0–80 mbsf) region affected by the diagenetic degradation of organic matter, which results in sulfate consumption as well as increases in alkalinity, ammonium, and phosphate. These changes are accompanied by calcite dissolution and dolomite precipitation, which are recorded by increases in dissolved strontium and decreases in dissolved magnesium and calcium. Additionally, the diatomaceous sequence in lithostratigraphic Subunit IB causes an increase in dissolved silica and a second peak in dissolved phosphate deeper in the sediments.

Physical sediment properties were determined both by high-resolution MST core logging and index properties measurements. Magnetic susceptibility and GRAPE signals reveal pronounced cyclicities, which were used for high-quality stratigraphic correlation in conjunction with digital color data.

The geophysical downhole logs show well-identified levels of high velocity, resistivity, and density attributed mainly to dolomitic layers. The Formation MicroScanner (FMS) shows dolomitic layers and numerous conductive horizons that might be related to high-porosity assemblages of diatomaceous microfossils. Porosity, density, and natural gamma radiation logs show high-frequency cyclical patterns that will be used as valuable indicators of paleoclimatic history and will provide age estimates for the sedimentary section.

Site 1081, in 793-m deep water on the Walvis Ridge, is the shallow-water drill site of the Walvis Ridge/Walvis Basin transect. The other anchors are DSDP Sites 532 and 362 in 1300 m water depth and Ocean Drilling Program (ODP) Sites 1082 and 1083. The DSDP sites are seaward of the upwelling center but contain an upwelling signal that has been transported by the Benguela Current. Site 1081 will give a better record of the upwelling itself. The transect, located above the calcite compensation

depth (CCD) in a passive-margin area of high sedimentation rates, will provide high-resolution records of these important processes and add important new dimensions to the records now available. This transect, situated on the only topographic high over which the Benguela Current passes, is central to the reconstruction of the history of the current.

## BACKGROUND AND OBJECTIVES

Site 1081, in 794 m water depth on the Walvis Ridge, is the shallowest of the sites drilled on the Walvis Ridge/Walvis Basin transect. The transect consists of DSDP Sites 532 and 362 (Legs 75 and 40) in ~1300 m water depth and ODP Sites 1081–1083. The DSDP sites are seaward of the upwelling center but contain an upwelling signal that has been transported by the Benguela Current. At DSDP Sites 362 and 532, the effects of glacial/interglacial cycles appear as carbonate dissolution, productivity, and continental sedimentation cycles. Both sea-level and climatic changes are recorded in these cycles. Site 1081, at the other end of the transect, will give a better record of the upwelling itself. Located above the CCD in a passive-margin area of high sedimentation rates, the transect can provide high-resolution records of these important processes and add important new dimensions to the records now available. Site 1081 is situated on the only topographic high over which the Benguela Current passes; thus, it is central to the reconstruction of the history of the current.

The upwelling off southwest Africa is centered, at present, on the inner shelf and at the shelf edge. The Benguela Current flows roughly parallel to the coast and stays within ~180 km of it south of 25°S; then it turns west over the Walvis Ridge between 23° and 20°S (Fig. 1). At about 20°S, warm, tropical water masses from the north meet the cold Benguela Current and generate eddies. Eddies of cold, upwelled water contain radiolarian and diatom skeletons that are transported from the upwelling area to the northern part of the Walvis Ridge, where they have been sampled at DSDP Sites 532 (Hay, Sibuet, et al., 1984) and 362 (Bolli, Ryan et al., 1978).

During the Last Glacial Maximum (LGM), the eddy formation took place farther north, and the Benguela Current flowed parallel to the coast and over the Walvis Ridge to reach the Angola Basin, finally bearing to the west at about 17°S. Sediments deposited at DSDP Site 532 during the LGM confirm the absence of upwelling eddies by containing very few or no opal skeletons (Hay, Sibuet, et al., 1984; Diester-Haass, 1985). Upwelling may have continued to occur on the African shelf, but the Benguela Current did not transport that upwelling signal to the Walvis Ridge. In contrast, from the distribution of foraminiferal assemblages at DSDP Site 532, it was suggested that the northeastern Walvis Ridge was characterized by intensified upwelling and a westward expansion of coastal upwelling cells at glacial periods during the last 500 k.y. (Oberhänsli, 1991).

Judging from opal sedimentation, the influence of the Benguela Current first makes itself felt on the Walvis Ridge about 10 m.y. ago (Bolli, Ryan et al., 1978; Diester-Haass, 1988; Diester-Haass et al., 1990; see Fig. 2). From 10 to ~6 Ma, maximum opal contents occurred during glacial periods, and opal minima coincided with interglacials. According to Diester-Haass and Rothe, (1987), the pattern of the opal signal changed at 5.2 Ma to become what has continued into the Quaternary: high opal concentrations during interglacial times and low concentrations during glacial intervals. The results from DSDP Sites 362 and 532 have been used to reconstruct the evolution of the Benguela Current during the past 10 m.y. (Fig. 2). Apparently, the 5.2-m.y. transition between the two upwelling regimes marks an important event. At this time (presumably) the dynamics dominating at present were established, perhaps in response to the simultaneous migration of the polar front to its modern position.

Another explanation for the transient increase and decrease in organic carbon and opaline silica-rich sediments at DSDP Sites 362 and 532 (Walvis Ridge) and DSDP Site 530 (Southern Angola Basin) is

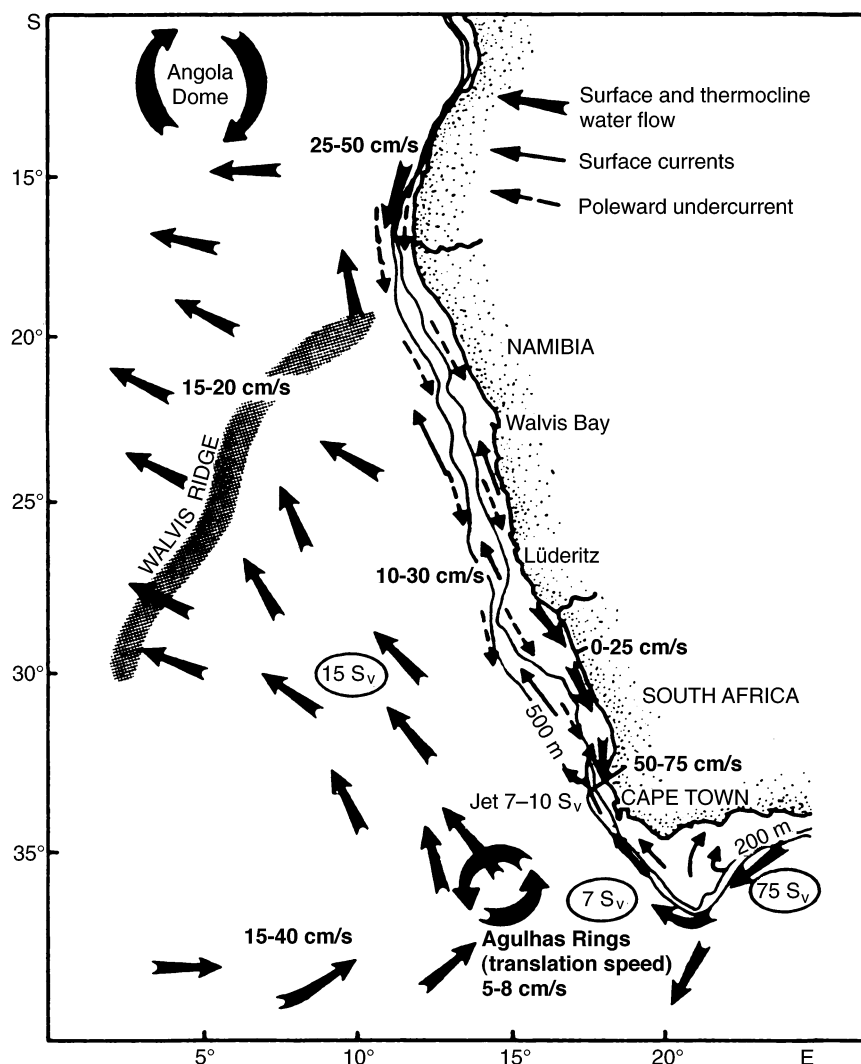


Figure 1. Schematic flow field of surface and thermocline waters. Current speeds refer to surface values. Transports (circled) refer to total transport above 1500 db (i.e., includes AAIW; Shannon and Nelson, 1996).

proposed by Hay and Brook (1992). They suggest that the enhanced upwelling during interglacials is a response to intensification of the Angola Dome, a cyclonic gyre off the Angola coast at 10°S that brings Antarctic Intermediate Water (AAIW) to within 50 m of the surface.

The shift in correlation from high opal deposition during glacials before 5.2 Ma to increased deposition during interglacials is thought by Hay and Brook (1992) to be related to changes in the production of AAIW. Although AAIW has a low salinity, the rate of production and the silicate content of AAIW presumably depends on the upwelling of North Atlantic Deep Water (NADW). If the production of NADW is reduced, the production of AAIW might also weaken because its salinity would become too low for vigorous sinking from the surface. If the production of AAIW diminished, sterile North Atlantic Intermediate Water formed from mixing of North Atlantic and Mediterranean water masses could become the dominant source of thermocline water in the northern South Atlantic during glacials. Thus, water upwelled from the Angola Dome would be nutrient poor, and hence there would be no record of enhanced biological productivity in the sediment, even if upwelling increased.

Clay mineralogical results at DSDP Site 362 give indications for a precursor to the modern Benguela Current in the middle Miocene (14 Ma), which was too weak to produce upwelling but reached the Walvis Ridge during glacial periods and transported montmorillonite

northward from the Orange River. In interglacial periods of the middle Miocene, the local source of illite (the Namib Desert) overwhelmed the distant montmorillonite supply (Diester-Haass et al., 1990).

The upwelling signal recorded in the opal content in the Pliocene–Pleistocene section at DSDP Site 532 is not only driven by glacial/interglacial cycles; large-scale changes also occur (Diester-Haass and Rothe, 1987). These changes can be explained either by east–west migrations of the axis of the Benguela Current or by changes in the intensity of the current. A strong increase in the upwelling signal at 2.4 Ma is synchronous with both a northward shift of the polar front in the South Atlantic and a lowering of the sea level.

Two ~11-m-long cores (Geosciences Bremen [GeoB] 1705-1, water depth 642 m and GeoB 1706-2, water depth 980 m) taken near Site 1081 showed sedimentation rates of 4–7 cm/k.y.

## OPERATIONS

### Hole 1081A (Proposed Site WR-1A)

The 184-nmi voyage to Site 1081 was impeded by rough seas and the northward-flowing Benguela Current. The vessel steered into 1.5-m swells generating up to 5° of pitch angle, which combined with the countercurrent, slowed the forward progress to 8 kt. By the time the

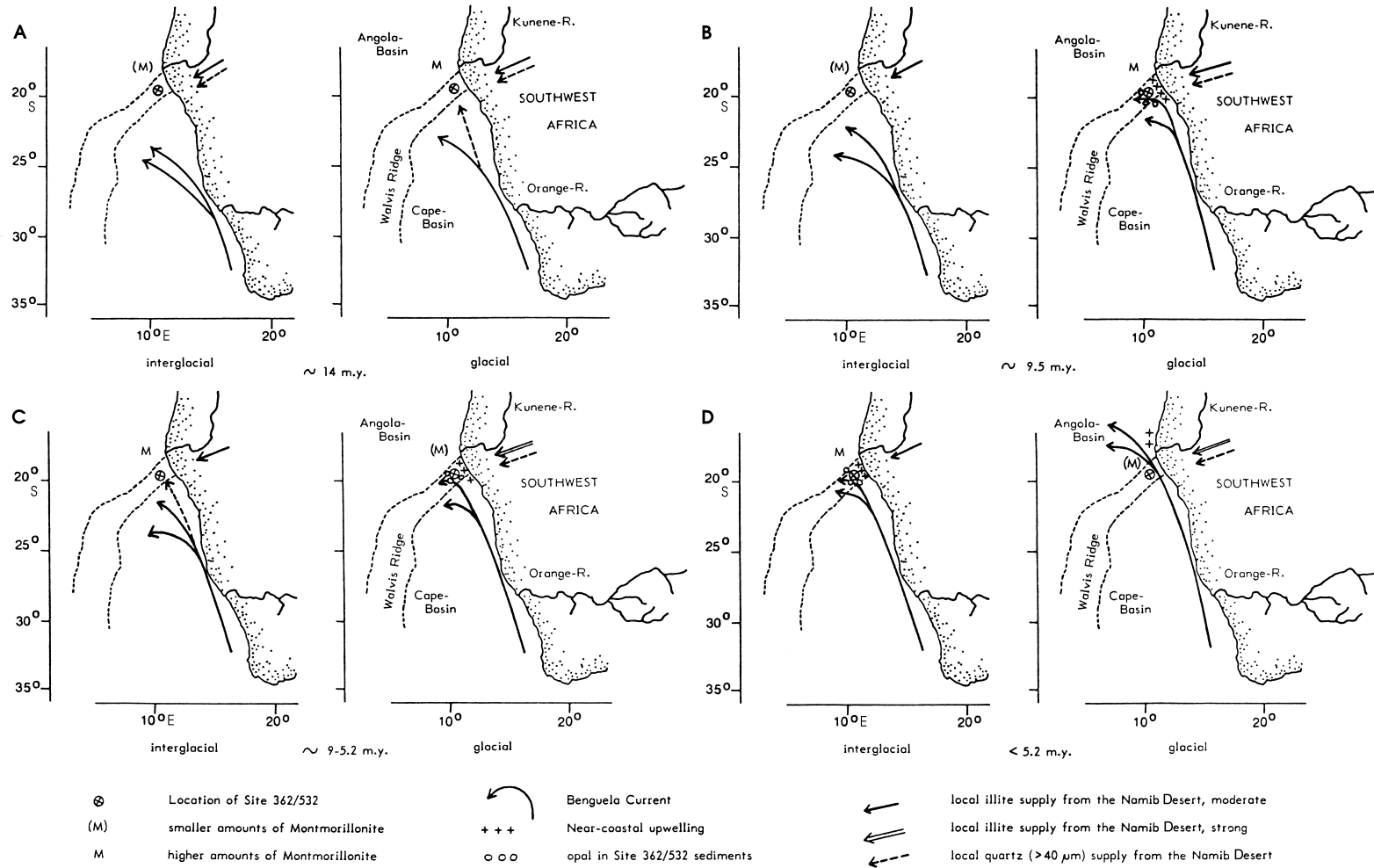


Figure 2. Evolution of the Benguela Current from about 15 Ma to the present (from Diester-Haass et al., 1990). **A.** ~14 Ma. **B.** ~9.5 Ma. **C.** ~9–5.2 Ma. **D.** <5.2 Ma.

*JOIDES Resolution* reached Site 1081, the seas had flattened, and the average speed had increased to 9.4 kt. The vessel proceeded directly to the Global Positioning System coordinates of the site, and a beacon was deployed at 0200 hr on 9 September. Hole 1081A was spudded with the APC at 0530 hr on 9 September. The seafloor depth was established at 796.1 meters below sea level (mbsl) by drill-pipe measurement (DPM). APC coring advanced without incident to 134.0 mbsf (Cores 175-1081A-1H through 15H; Table 1; also see the expanded core summary table on CD-ROM, back pocket, this volume). Core 175-1081A-16H advanced only 3 m, and coring operations were switched to the XCB system. The XCB penetrated through a 1-m-thick firm horizon and then quickly advanced into softer sediments. Operations were switched back to APC coring. Core 175-1081A-18H advanced the hole to 154.5 mbsf using advancement by recovery. Core 175-1081A-19H failed to advance because of stiffer sediments, and XCB coring was initiated again. Total penetration with the APC was 145.5 m, with 103.9% recovery (Table 1). Cores were oriented starting with Core 4H. Adara heat-flow measurements were taken at 29.5 mbsf (4H), 58.0 mbsf (7H), 86.5 mbsf (10H), 115.0 mbsf (13H), and 137.0 mbsf (16H). XCB coring advanced to 452.7 mbsf (49X), which was the revised depth objective at Site 1081. The penetration with the XCB was 307.2 m, with 78.9% recovery. The total recovery at Hole 1081A was 86.9%.

### Logging Operations in Hole 1081A

In preparation for logging, an aluminum go-devil was dropped to ensure the opening of the lockable float valve. After the hole was

flushed with a high-viscosity mud, the drill string was pulled back to 403.7 mbsf, where the top drive was set back. The drill bit was then placed at the logging depth of 101.2 mbsf. Hole 1081A was logged with a full suite of sensors to continuously characterize the sedimentary changes as a proxy for the paleoclimatic record and to provide data for core-log integration. For each run, the pipe was set at 101 mbsf and pulled back to 71 mbsf during logging. The wireline logging heave compensator was started when the logging tools reached the mudline.

Logging operations began at 0200 hr on 9 September. The first log was conducted with the seismostratigraphic suite (25.8 m long). This suite was made up of the spectral gamma-ray (NGT), long-spacing sonic (LSS), phasor dual-induction (DITE), and Lamont-Doherty high-resolution temperature (TLT) sondes. This tool string was deployed in the pipe at 0245 hr and logged the hole up from 450.5 mbsf. The tool string was recovered at 0550 hr. The second log was conducted with the lithoporosity suite (19.5 m long) and included the hostile environment gamma spectrometry (HNGS), accelerator porosity (APS), lithodensity (LDS), and TLT sondes. The tool string was deployed at 0655 hr and logged the hole up from 450.5 mbsf. The third log was made with the FMS suite (12.10 m long) and included the NGT, general purpose inclinometer, and FMS sondes. This tool logged the hole up from 450.5 mbsf. The tool string was recovered at 1425 hr. The fourth and last log was made with the magnetic susceptibility suite (11.8 m long) and included the NGT, magnetic susceptibility, and the nuclear resonance magnetometer sondes. The tool string was deployed in the pipe at 1455 hr and logged the hole up from 450.5 mbsf. It was retrieved at 1740 hr. The logging equipment

**Table 1. Coring summary for Site 1081.**

Core	Date (Sept 1997)	Time (UTC)	Interval (mbsf)	Length cored (m)	Length recovered (m)	Recovery (%)
175-1081A-						
1H	9	0540	0.0-1.0	1.0	0.94	94.0
2H	9	0610	1.0-10.5	9.5	7.27	76.5
3H	9	0635	10.5-20.0	9.5	9.60	101.1
4H	9	0725	20.0-29.5	9.5	9.98	105.1
5H	9	0755	29.5-39.0	9.5	9.67	101.8
6H	9	0820	39.0-48.5	9.5	9.57	100.7
7H	9	0905	48.5-58.0	9.5	9.63	101.4
8H	9	0930	58.0-67.5	9.5	9.76	102.7
9H	9	1000	67.5-77.0	9.5	9.27	97.6
10H	9	1040	77.0-86.5	9.5	9.36	98.5
11H	9	1105	86.5-96.0	9.5	9.67	101.8
12H	9	1135	96.0-105.5	9.5	9.10	95.8
13H	9	1225	105.5-115.0	9.5	9.37	98.6
14H	9	1310	115.0-124.5	9.5	9.55	100.5
15H	9	1345	124.5-134.0	9.5	10.21	107.5
16H	9	1430	134.0-137.0	3.0	9.69	323.0
17X	9	1630	137.0-146.0	9.0	7.50	83.3
18H	9	1710	146.0-154.5	8.5	8.54	100.5
19X	9	1945	154.5-164.1	9.6	9.72	101.3
20X	9	2015	164.1-173.8	9.7	8.85	91.2
21X	9	2045	173.8-183.5	9.7	8.63	89.0
22X	9	2120	183.5-193.1	9.6	9.91	103.2
23X	9	2150	193.1-202.8	9.7	8.76	90.3
24X	9	2220	202.8-212.4	9.6	6.54	68.1
25X	9	2255	212.4-222.0	9.6	7.45	77.6
26X	9	2330	222.0-231.5	9.5	6.33	66.6
27X	10	0005	231.5-241.2	9.7	8.88	91.5
28X	10	0040	241.2-250.8	9.6	8.72	90.8
29X	10	0110	250.8-260.4	9.6	7.97	83.0
30X	10	0145	260.4-270.1	9.7	7.17	73.9
31X	10	0215	270.1-279.7	9.6	3.83	39.9
32X	10	0245	279.7-289.3	9.6	9.67	100.7
33X	10	0310	289.3-299.0	9.7	8.82	90.9
34X	10	0415	299.0-308.6	9.6	3.20	33.3
35X	10	0505	308.6-318.2	9.6	3.45	35.9
36X	10	0600	318.2-327.8	9.6	8.99	93.6
37X	10	0710	327.8-337.5	9.7	8.30	85.6
38X	10	0815	337.5-347.1	9.6	4.36	45.4
39X	10	0915	347.1-356.8	9.7	9.63	99.3
40X	10	1040	356.8-366.4	9.6	1.20	12.5
41X	10	1145	366.4-376.0	9.6	8.88	92.5
42X	10	1315	376.0-385.6	9.6	9.82	102.3
43X	10	1440	385.6-395.3	9.7	9.36	96.5
44X	10	1600	395.3-404.9	9.6	2.54	26.5
45X	10	1715	404.9-414.6	9.7	9.84	101.4
46X	10	1825	414.6-424.2	9.6	9.76	101.7
47X	10	1950	424.2-433.8	9.6	9.55	99.5
48X	10	2115	433.8-443.5	9.7	9.74	100.4
49X	10	2315	443.5-452.7	9.2	4.93	53.6
Coring totals:				452.7	393.48	86.9
175-1081B-						
1H	16	120	0.0-3.7	3.7	3.70	100.0
2H	16	145	3.7-13.2	9.5	9.75	102.6
3H	16	205	13.2-22.7	9.5	9.99	105.2
4H	16	240	22.7-32.2	9.5	9.75	102.6
5H	16	310	32.2-41.7	9.5	10.10	106.3
6H	16	340	41.7-51.2	9.5	10.29	108.3
7H	16	410	51.2-60.7	9.5	9.64	101.5
8H	16	435	60.7-70.2	9.5	10.11	106.4
9H	16	505	70.2-79.7	9.5	10.17	107.1
10H	16	530	79.7-89.2	9.5	10.03	105.6
11H	16	605	89.2-98.7	9.5	10.05	105.8
12H	16	635	98.7-108.2	9.5	10.15	106.8
13H	16	705	108.2-117.7	9.5	10.08	106.1
14H	16	730	117.7-127.0	9.3	9.36	100.6
Coring totals:				127.0	133.17	104.9
175-1081C-						
1H	12	1000	0.0-7.3	7.3	7.50	102.7
2H	12	1025	7.3-16.8	9.5	10.07	106.0
3H	12	1050	16.8-26.3	9.5	10.05	105.8
4H	12	1110	26.3-35.8	9.5	10.07	106.0
5H	12	1125	35.8-45.3	9.5	9.77	102.8
6H	12	1155	45.3-54.8	9.5	9.83	103.5
7H	12	1220	54.8-64.3	9.5	9.73	102.4
8H	12	1245	64.3-73.8	9.5	9.86	103.8
9H	12	1315	73.8-83.3	9.5	9.85	103.7
10H	12	1340	83.3-92.8	9.5	9.81	103.3
11H	12	1405	92.8-102.3	9.5	9.75	102.6
12H	12	1430	102.3-111.8	9.5	9.98	105.1
13H	12	1455	111.8-121.3	9.5	9.95	104.7
14H	12	1520	121.3-130.8	9.5	9.98	105.1
15H	12	1550	130.8-138.4	7.6	7.70	101.3
16H	12	1620	138.4-147.9	9.5	9.68	101.9
17H	12	1655	147.9-155.2	7.3	7.36	100.8
Coring totals:				155.2	160.94	103.7

Notes: UTC = Universal Time Coordinated. An expanded version of this coring summary table that includes lengths and depths of sections and comments on sampling is included on CD-ROM (back pocket, this volume).

was rigged down by 1830 hr on 9 September. The hole was filled with heavy mud. The drill string was then pulled out of the hole with the bit clearing the seafloor at 2115 hr on 11 September, ending operations at Hole 1081A.

### Hole 1081B

The vessel was offset 30 m to the south, and Hole 1081B was spudded with the APC at 2220 hr on 11 September. The seafloor depth was established at 793.1 mbsl by DPM. APC coring advanced without incident to refusal at 187.6 mbsf, with 104.4% recovery (Table 1). Cores were oriented starting with Core 175-1081B-4H. The bit cleared the seafloor at 0925 hr on 12 September, thereby ending operations at Hole 1081B.

### Hole 1081C

The vessel was offset 30 m to the south, and Hole 1081C was spudded with the APC at 0955 hr. The seafloor depth was established at 793.8 mbsl by DPM. APC coring advanced routinely to refusal at 155.2 mbsf. The recovery was 103.7% (Table 1). Cores were oriented starting with Core 175-1081C-3H. The bit cleared the seafloor at 1815 hr, thereby ending operations at Site 1081.

## SITE GEOPHYSICS

### Introduction and Strategy

The Walvis Ridge at 20°S separates the Angola and Cape Basins in the eastern South Atlantic. Plate tectonic processes dominated the early evolution of the South Atlantic, which caused pronounced differences between the two basins since the Cretaceous because of the development of the Walvis Ridge and Rio Grande Rise as barriers for open-ocean circulation in the northern basins. The Walvis Ridge affects the oceanography of the region to this day and, in conjunction with the structure of the continental margin, is an important element of the Benguela upwelling and current systems.

The fourth working area of ODP Leg 175 covers the Walvis Ridge and the Walvis Basin as part of the Cape Basin. The general structure of the Cape Basin continental margin, which developed during the Cretaceous after the breakup of Gondwanaland, is summarized in several comprehensive papers (e.g., Emery and Uchupi, 1984; Dingle and Robson, 1992). In general, sedimentation at the continental margin was characterized by intense terrigenous deposition during the early opening of the South Atlantic in the Cretaceous. This high sedimentation rate subsequently declined during the Paleogene. Aridification of the continent in the Oligocene and Miocene led to a further decrease in sedimentation rate which, in conjunction with intensified bottom-water currents, resulted in starved conditions in the deeper region of the Cape Basin.

Isopach maps (Gerrard and Smith, 1984) based on borehole data, offshore geology, and seismics related to exploration activities along the coast indicate the presence of only a few elongated Cenozoic depocenters along the margin seaward of the Mesozoic depocenters. The northernmost depocenter, the Walvis Basin, was identified as a potential area to drill expanded sequences of Neogene upwelling sediments and was surveyed during *Meteor* Cruise M34/1 in January 1996 (Bleil et al., 1996).

The Walvis Ridge and Walvis Basin together represent a depositional realm, which is fed mainly by a combination of diatom-dominated coastal upwelling and oceanic production of biogenic carbonate. Deposition rates of the different components are supposed to be a function of distance to the coast, upwelling intensity, and the location of the different arms of the Benguela Current systems. The site on the Walvis Ridge was located closer to the coast and toward the coastal upwelling cell on the Walvis Ridge than DSDP Site 532 (Hay,

Sibuet, et al., 1984). Sites in the Walvis Basin, for which basically no seismic data were available before *Meteor* Cruise M34/1, were added to the original proposal to reconstruct fluctuations in upwelling activity and to monitor movements of the Benguela ocean current.

An extensive 7-day seismic survey was carried out between 19°30'S and 22°S in water depths from 200 to 2500 m (Fig. 3). The area is located off the most active coastal upwelling areas of the world, and it was assumed that it received significant sediment input during the late Neogene. Variations in thickness and regional distribution of seismic units should reflect the intensities and locations of the major sediment sources. Accordingly, a grid of seismic lines was chosen to allow future two-dimensional analyses. The seismic survey revealed a wide depositional basin characterized by significant subsidence on the upper continental slope, probably also as a result of the high sediment load. This led to a moderately inclined continental slope, which supported rapid hemipelagic deposition without the typical mass-movement events. No indication for slumping was found in Neogene sequences.

Because the seismic survey covered both the proposed sites on the Walvis Ridge and in the Walvis Basin and DSDP Sites 532 and 362, drilled in 1300 m water depth on the crest of the ridge, a seismostratigraphic framework could be developed for the uppermost seismic units based on previous drilling results. Accordingly, a few marker horizons were chosen and could be traced along the lines into the working area to estimate ages and sedimentation rates. Studies of seismic and digital echosounder data near DSDP Site 532 also revealed increasing current intensities, winnowing, and erosion.

### Seismostratigraphy

A net of 16 seismic lines with a total length of 1550 km was recorded in the working area during *Meteor* Cruise M34/1 (Fig. 3). About 395 km was located on the crest and southern flank of the Walvis Ridge; 1155 km covered the Walvis Basin. The lines were oriented so that both sediment input from and variations along the coast could be identified from two-dimensional analyses. Sites in the Walvis Basin were chosen on Lines GeoB/AWI 96-015 and 96-017, for which crossing lines were shot. The Walvis Ridge site was originally proposed based on data of Sibuet et al. (1984), which were collected during the presite survey for DSDP Leg 75. High-resolution multichannel seismic data were recorded during *Meteor* Cruise M34/1. Lines GeoB/AWI 96-020 to 96-022 connect the Walvis Basin with DSDP Sites 532 and 362, and Line GeoB/AWI 96-024 runs across DSDP Sites 532 and 362 along the crest of the Walvis Ridge upslope. Shore-based studies will allow detailed correlations of the seismic data, specifically the reconstruction of areal depositional patterns and accumulation rates.

The area of the seismic survey generally shows similar overall acoustic characteristics. Three sections of seismic lines will be shown across Sites 1081–1083 to illustrate these similarities.

Line GeoB/AWI 96-024 (Fig. 4) reveals a large number of strong reflectors in the upper seismic Unit 1. They cover a depth range of 250 ms two-way traveltime (TWT) at DSDP Site 532, but extend down to 750 ms TWT at Site 1081. Also, the zone of higher seismic amplitudes does not cover the same lithologies but ranges stratigraphically deeper at Site 1081. This may indicate different origins for high amplitudes at both sites, and further, more detailed analyses are required to understand these lateral variations. This seismic unit was not penetrated at Site 1081; therefore, deeper units will not be discussed here (see Sibuet et al., 1984). This unit, however, thins significantly between common depth points (CDPs) 1000 and 3000, and an erosional contact can be identified at ~100 ms TWT. The erosional contact is attributed to bottom currents that are forced to cross the Walvis Ridge and are accelerated, causing winnowing and erosion. Surface sediment cores taken at shallower water depth by the University of Bremen revealed numerous hiatuses. The sedimentary unit

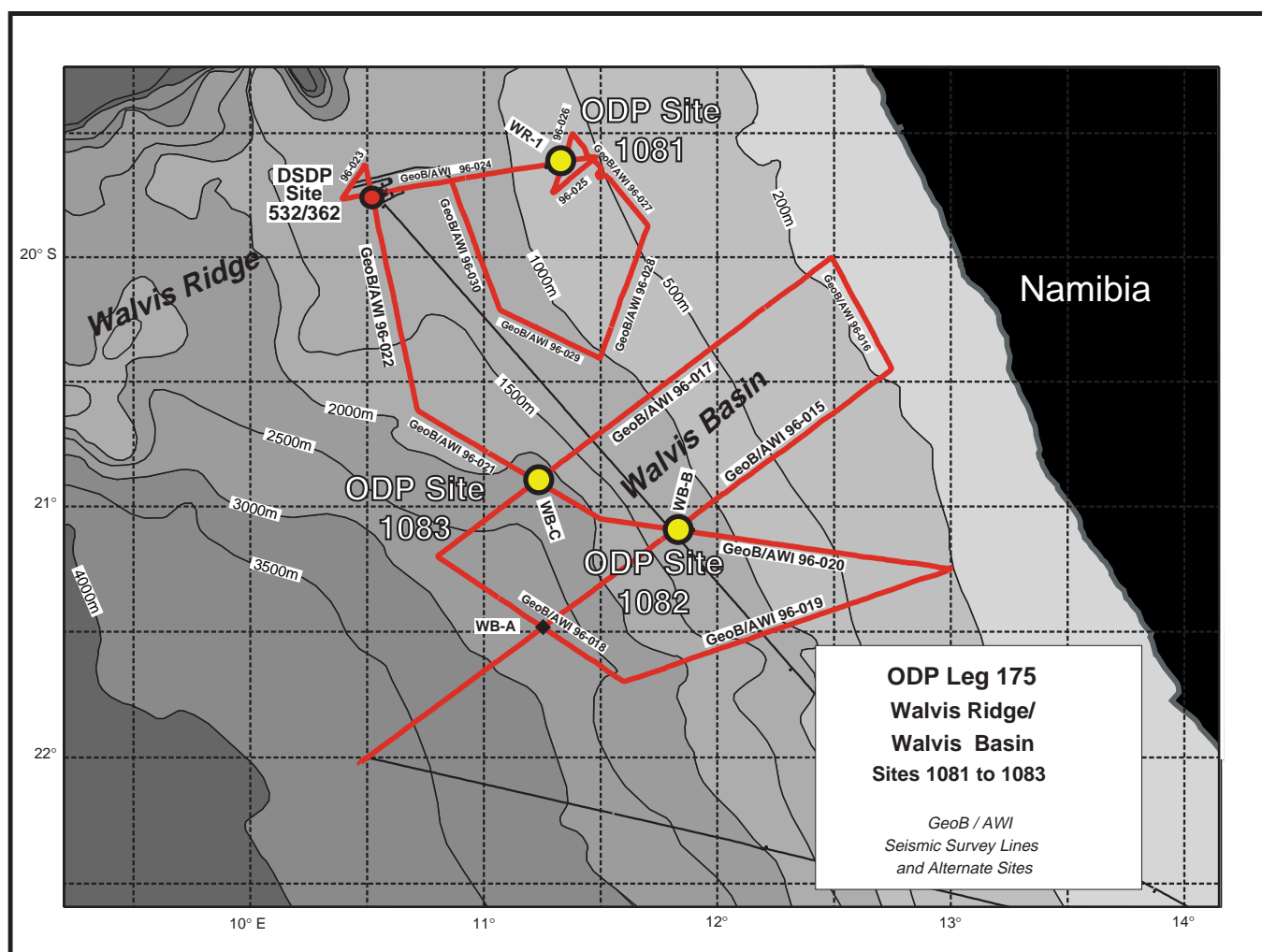


Figure 3. Map of seismic presite survey lines, proposed site locations, and ODP Leg 175 drill Sites 1081 to 1083 on the Walvis Ridge, in the Walvis Basin, and across DSDP Site 532. Bathymetry was derived from Gebco Digital Dataset on CD-ROM.

above the erosional surface thickens again toward Site 1081 from 100 ms TWT to a thickness  $>300$  ms TWT. There, the sequence appears to be continuous. The sedimentary packages beneath the drilled sequences are moderately affected by faulting. Also, a slump unit could be identified at  $\sim 700$  ms TWT upslope of Site 1081, but no indication for slumping was found at shallower depth.

Line GeoB/AWI 96-015 (Fig. 5) also shows an upper seismic unit of high-amplitude reflectors to a sub-bottom depth of 600 ms TWT, which was the target for drilling. This unit thins downslope, and again the interval of high seismic amplitude ranges stratigraphically deeper than at greater water depth. Around CDP 5500, a major slump scarp probably of Eocene age was observed, which could also be identified on other lines. Reflectors in the upper seismic unit can be traced to DSDP Site 532 along Lines GeoB/AWI 96-020, 96-021, and 96-022. In particular, according to this preliminary correlation, the Eocene/Oligocene boundary can be placed at about 750 ms TWT at Site 1082. A zone of even higher seismic amplitudes associated with significant scatter energy at shallower depth between CDPs 7200 and 8300 was avoided for drilling.

Line GeoB/AWI 96-017 (Fig. 6) basically reveals the same seismic characteristics as the other seismic lines but also shows a seaward thinning of the upper sedimentary sequence. The general morphology is still slightly affected by the surface created during the

Eocene slump event and/or by subsequent movements, but deposition of the upper unit of high seismic-reflection amplitudes is apparently unaffected. A major tectonic feature around CDP 4700, including local subsidence, was avoided for drilling.

### Site 1081

Site 1081 is located in 794 m water depth at the northern end of the survey area (Fig. 3) on Line GeoB/AWI 96-024 (CDP 3967). Figure 7 shows a 10-km-long seismic section of Line GeoB/AWI 96-024 across Site 1081. The seismic pattern reflects hemipelagic deposition without major disturbances or faulting. Some indication for slumping was found at 700 ms TWT sub-bottom depth upslope of CDP 4020, but not within the drilling range of 450 m. Seismic amplitudes vary significantly along Line GeoB/AWI 96-024 between DSDP Site 532 and ODP Site 1081 (Fig. 4) and increase near Site 1081. Seismic characteristics remain constant within the drilled depth range and give rise to the development of a detailed seismostratigraphy.

Figure 8 shows a close-up of the seismic section, plotted against sub-bottom depth for a sound velocity of 1500 m/s, for a 1-km-long interval near the drill site. Seismic reflectors are compared with the density log (see "Downhole Logging" section, this chapter). Sharp peaks in the density log indicate dolomitic or carbonate-rich clays,

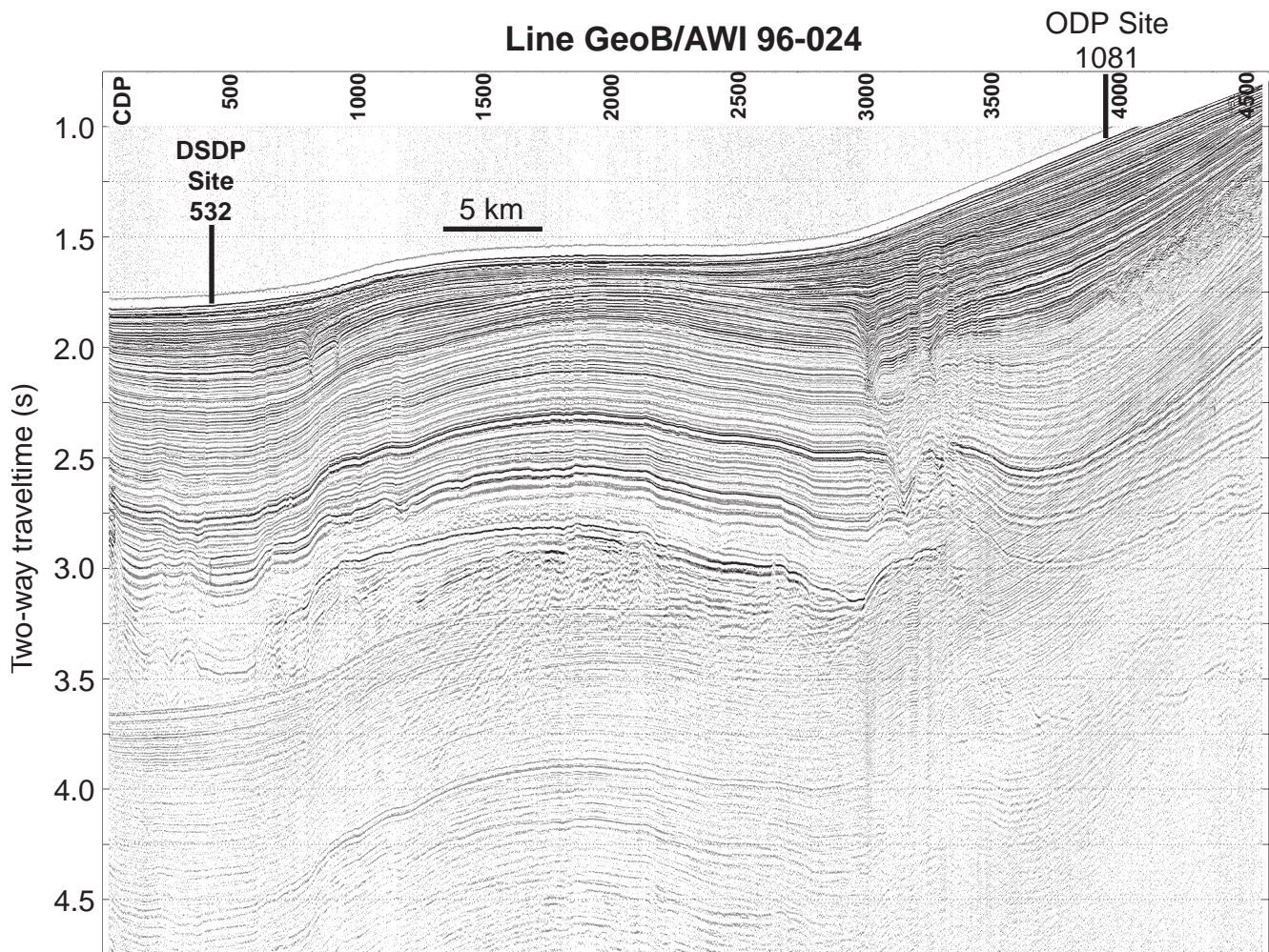


Figure 4. Seismic Line GeoB/AWI 96-024 with Site 1081. Vertical axis is given in TWT. CDP interval is 25 m for a shotpoint spacing of 25 m. Seismic data is 24-fold stacked and not migrated. Site 1081 is located at CDP 3967.

sometimes lithified to different degrees (see “Lithostratigraphy” section, this chapter). Most of these peaks could also be correlated to peaks in GRAPE density or findings of lithified sediment pieces in the core or core catchers, which are not measured with the MST.

Some seismic reflectors can be directly correlated to these layers, but in other cases no seismic energy is found at these depths. A dependency on layer thickness, as derived from logging data (see Fig. 47, “Downhole Logging” section, this chapter), was not observed. Surprisingly, the band of dolomitic layers from 300 to 320 mbsf is not seen in the seismic record. Also, some major lithologic changes seem to be associated with seismic reflectors, but seismic modeling is required to provide a precise reference for high-resolution seismic stratigraphy. Traditional seismic stratigraphy, conducted by identifying major reflectors with pronounced lithologic changes and geologic events, cannot be carried out where early diagenesis has locally overprinted the physical properties, as is observed at Site 1081. A more detailed approach has to be taken and further high-resolution seismic measurements, together with the analysis of frequency-dependent seismic properties (seismic attributes), are required to distinguish between dolomitic layers and other lithologic changes.

#### Site 1082

Site 1082 is located in 1280 m water depth in the middle of the survey area (Fig. 9) on Line GeoB/AWI 96-015 (CDP 6837). Figure 9 shows a 10-km-long seismic section of Line GeoB/AWI 96-015 across Site 1082. The seismic pattern reflects hemipelagic deposition

without major disturbances or faulting. Seismic amplitudes are high for the upper unit and gradually decrease beneath 600 ms TWT sub-bottom depth. Seismic characteristics remain constant within the drilled depth range and give rise to the development of a detailed seismic stratigraphy.

Figure 10 shows a close-up of the seismic section, plotted against TWT, for a 1-km-long interval near the drill site. Seismic reflectors are compared with the sound velocity log (see “Downhole Logging” section, this chapter), which was also used to recalculate logging depth to TWT. This modification was necessary because for the first time during the leg, velocities were so high that scale stretching could not be used because of a nonlinear relationship. Peaks in the velocity log are associated with dolomite layers or lithified intervals, and several could be correlated to seismic reflectors. Major lithologic changes have a more pronounced effect on density, which is not shown here but may have only a minor impact on velocity. Therefore, it cannot be expected that all reflectors find expressions in the velocity log. However, the boundary between lithologic Units IB and IC from diatom-rich clay to nannofossil clay, which is associated with a sharp increase in density with depth, is clearly identified at 485 ms in the seismic record.

#### Site 1083

Site 1083 is located in 2178 m water depth northwest of Site 1082 (Fig. 3) on Line GeoB/AWI 96-017 (CDP 6642). Figure 11 shows a 10-km-long seismic section of Line GeoB/AWI 96-017 across Site

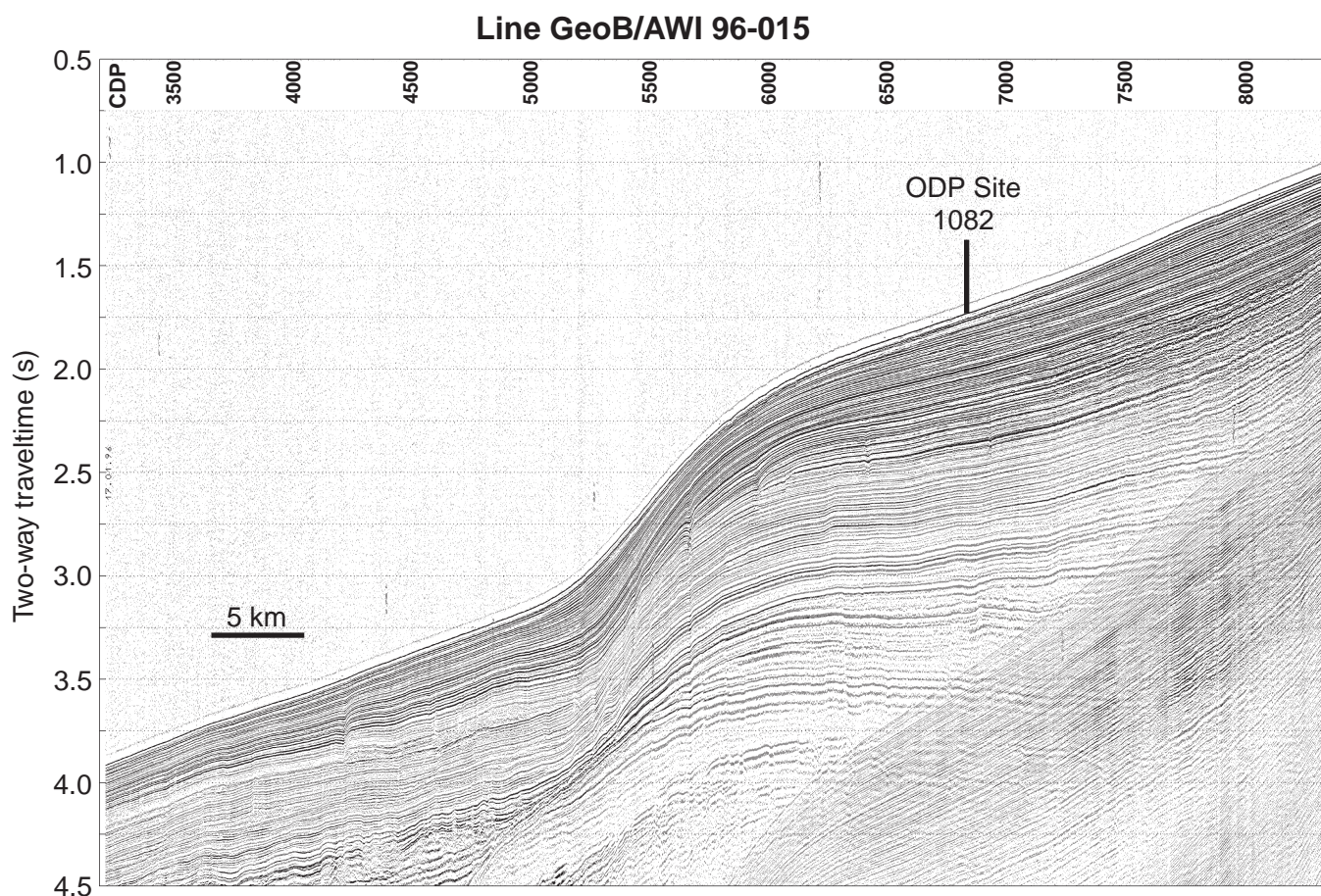


Figure 5. Seismic Line GeoB/AWI 96-015 with Site 1082. Vertical axis is given in TWT. CDP interval is 25 m for a shotpoint spacing of 25 m. Seismic data is 24-fold stacked and not migrated. Site 1082 is located at CDP 6837.

1083. The seismic pattern reflects hemipelagic deposition without major disturbances or faulting and is very similar to the pattern at Sites 1081 and 1082. An unconformity or an intercalated slumped block is observed deeper in the section at 650 ms and is more pronounced farther downslope, from CDP 6700 on. The unit of increased seismic amplitudes is thinner than at Site 1082 and can be correlated in detail between the sites along Lines GeoB/AWI 96-021 and 96-022.

Figure 12 shows a close-up of the seismic section, plotted against sub-bottom depth for a sound velocity of 1500 m/s, for a 1-km-long interval near the drill site. Seismic reflectors are compared with the GRAPE density log (see “Physical Properties” section, this chapter). Physical properties show pronounced and rapid fluctuations at rates that cannot be directly imaged because of the limited seismic frequency content of the data. Some major features of the density core log seem to be associated with reflectors, however, particularly in the interval of higher diatom abundance between 100 and 160 mbsf. No evidence for lithified intervals was found at this site, and amplitudes of reflection are generally lower. Some of the reflectors seem to be traceable to Site 1082, where they are associated with dolomitic layers.

## LITHOSTRATIGRAPHY

### Description of Lithostratigraphic Units

Three holes were drilled at Site 1081 with a maximum penetration of 452.7 mbsf (Fig. 13). The APC was used down to Cores 175-1081A-16H, 175-1081B-21H, and 175-1081C-17H. Because of gas expansion and the fact that several intervals, each as much as 60 cm

long, contained flow-in structures, the APC cores have an average recovery >100%. Hole 1081A was deepened to Core 175-1081A-49X (452.7 mbsf) using the XCB, with an average recovery of 78.9%. The XCB cores generally consist of 2- to 4-cm-thick sediment biscuits that are embedded in drill mud. The top 30–60 cm of both ACP and XCB cores are generally disturbed, and the core catcher contains a mixture of material from the whole core.

Sediments from Site 1081 form two lithostratigraphic units. Unit I is composed of olive (5Y 4/3), olive-gray (5Y 4/2), dark olive-gray (5Y 4/1), and black (5Y 2.5/1) clays, which contain varying amounts of diatoms, nannofossils, foraminifers, and radiolarians (Fig. 13). Unit I is moderately bioturbated, containing burrows of ~1 to 2 cm in diameter. Three subunits are defined based on variations in abundance and type of microfossils in the sediments. Unit II is composed of olive (5Y 4/3) and olive-gray (5Y 4/2) clayey nannofossil ooze.

#### Unit I

Interval: 175-1081A-1H-1, 0 cm, to 175-1081A-43X-3, 40 cm  
Age: Holocene to Miocene  
Depth: 0–390 mbsf

#### Subunit IA

Interval: 175-1081A-1H-1, 0 cm, through 175-1081A-9H  
Age: Holocene to Pleistocene  
Depth: 0–77 mbsf

The uppermost subunit is composed of bioturbated olive (5Y 4/3) and olive-gray (5Y 4/2), nannofossil- and foraminifer-rich clay. The contact between Subunits IA and IB is defined by an increase in the abundance of diatoms from bearing to rich and a corresponding de-

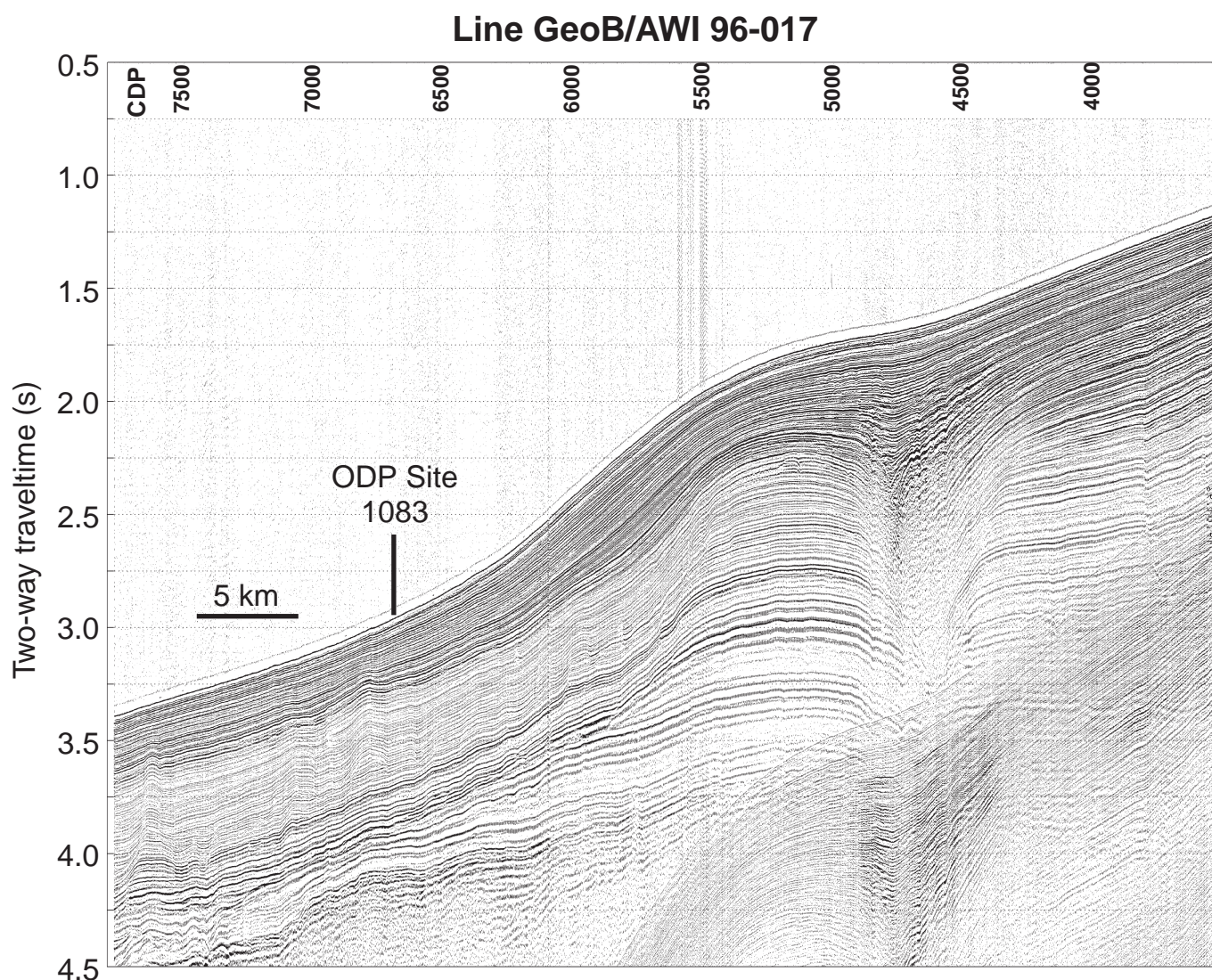


Figure 6. Seismic Line GeoB/AWI 96-017 with Site 1083. Vertical axis is given in TWT. CDP interval is 25 m for a shotpoint spacing of 25 m. Seismic data is 24-fold stacked and not migrated. Site 1083 is located at CDP 6642.

crease in nannofossil content. The contact is gradational over tens of meters, but the boundary is placed between Cores 175-1081A-9H and 10H (77 mbsf), Sections 175-1081B-9H-3 and 9H-4 (76 mbsf), and Sections 175-1081C-10H-4 and 10H-5 (90 mbsf). The subunit contains intervals with different-colored clays whose thicknesses range from 60 to 250 cm and that grade into one another over a distance of 20 to 40 cm. Subunit IA contains short intervals at Holes 1081A and 1081B in which the nannofossil and foraminiferal abundances are high enough for the sediments to be defined as nannofossil and foraminifer ooze (e.g., all of Core 175-1081A-2H and interval 175-1081B-6H-5, 50 cm, to 175-1081B-6H-7, 60 cm). Subunit IA has high carbonate (average of 30 wt%) and organic carbon (5 wt%) concentrations (see “Organic Geochemistry” section, this chapter).

#### *Subunit IB*

Interval: 175-1081A-10H through 175-1081A-26X  
 Age: Pleistocene to early Pliocene  
 Depth: 77–230 mbsf

Subunit IB is composed of intercalated intervals of black (5Y 2.5/1) and dark olive-gray (5Y 3/2) diatom-rich clay. Subunit IB is recognized in all three holes, but its contact with Subunit IC is observed only between Cores 175-1081A-26X and 27X (230 mbsf). The tran-

sition from Subunit IA to Subunit IB is gradational over several meters and is marked by an increase in the abundance of diatoms, a decrease of nannofossils, and a disappearance of planktonic foraminifers (see “Synthesis of Smear-Slide Analyses” and “Biostratigraphy and Sedimentation Rates” sections, this chapter). The same trend is reflected in the decrease of the carbonate concentration to an average of 6 wt%, with minimum values <1 wt%. Subunit IB contains intervals of different-colored clays ranging in thickness from 60 to 250 cm. Intervals grade into one another over a distance of 20 to 40 cm. Subunit IB is darker in color and has lower total reflectance than Subunit IA. Smear-slide examination indicates an increase in abundance of organic matter (see “Synthesis of Smear-Slide Analyses” section, this chapter), which is confirmed by an increase in the organic carbon concentration to a maximum of 8.2 wt% and an average of 6 wt%. Dolomitized clays are present in Subunit IB in intervals 175-1081A-17X-1, 0–24 cm (~137 mbsf), 175-1081A-19X-1, 0–25 cm (~154 mbsf), 175-1081A-20X-2, 60–110 cm (~166 mbsf), and 175-1081A-22X-3 (~183 mbsf; see Fig. 14).

#### *Subunit IC*

Interval: 175-1081A-27X to 175-1081A-143X-3, 41 cm  
 Age: early Pliocene to Miocene

## Line GeoB/AWI 96-024

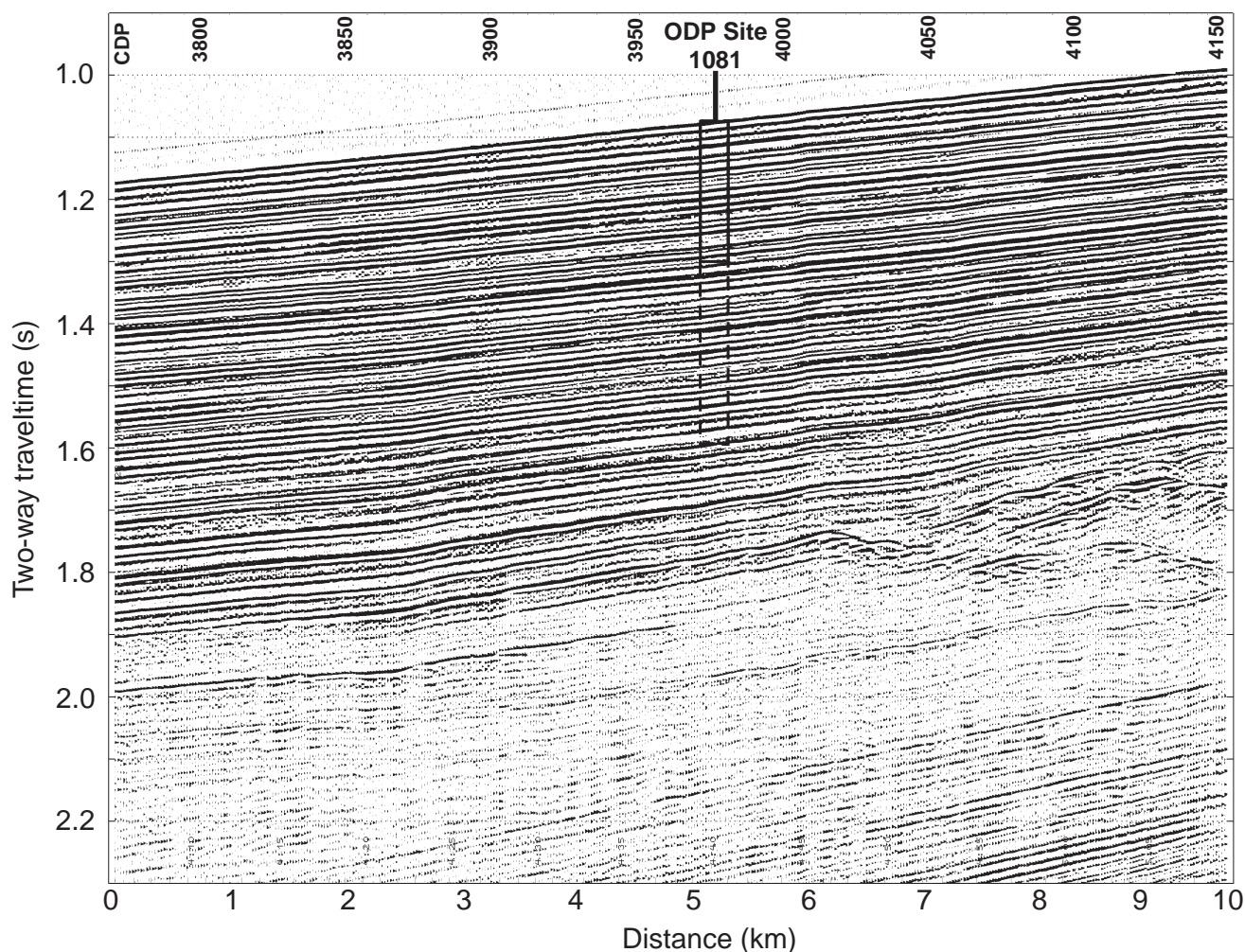


Figure 7. Seismic section of line GeoB/AWI 96-024 at Site 1081. Vertical axis is given in TWT. CDP interval is 25 m for a shotpoint spacing of 25 m. Site 1081 is located at CDP 3967. The box indicates the approximate penetration of the borehole of 200 m (APC) and 450 m (XCB), respectively.

Depth: 230–390 mbsf

Subunit IC is composed of olive (5Y 4/3) to olive-gray (5Y 4/2) nannofossil-rich clay. The transition between the diatom-rich, nannofossil-poor Subunit IB and the nannofossil-rich and diatom-poor Subunit IC is gradational and occurs between Cores 175-1081A-26X and 27X (230 mbsf). The transition from Subunit IC to Unit II is gradational and occurs within Section 175-1081A-43X-3 (390 mbsf). This boundary is marked by a significant decrease in the abundance of diatoms and an increase in the abundance of nannofossils. Subunit IC has high carbonate concentrations, which average 20 wt%, and low organic carbon concentrations, which average 2.5 wt%. No dolomitized clay intervals are found in Subunit IC; however, subhedral dolomite rhombs are observed in smear slides.

### Unit II

Interval: 175-1081A-43X-3, 41 cm, to 175-1081A-49X-5, 28 cm

Age: Miocene

Depth: 390–452.7 mbsf

Unit II is composed of olive (5Y 4/3) to olive-gray (5Y 4/2) clayey nannofossil ooze. Unit II has high calcium carbonate content, which averages 40 wt%, but low organic carbon content, which aver-

ages 2 wt%. Foraminifers and diatoms are present in Unit II but only in Cores 175-1081A-44X and 45X.

### Synthesis of Smear-Slide Analyses

Smear-slide analyses indicate that the detrital component of the sediment is a clay with rare silt-sized, angular and subangular, mono- and polycrystalline quartz grains, and feldspar. Muscovite and biotite are present in trace amounts. The biogenic component is represented by varying abundances of foraminifers (whole and fragments), nannofossils, and diatoms. Varying amounts of particulate organic matter and authigenic minerals, such as glauconite, framboidal pyrite, and dolomite, are observed in both trace and few abundances. Euhedral dolomite rhombs and fragments of sparry calcite cement are also common below Section 175-1081A-27X-2.

### X-ray Diffraction Analysis

X-ray diffraction (XRD) analysis of sediments from Hole 1081A reveals that the clastic fraction is dominated by the clay minerals smectite, kaolinite and illite, muscovite (mica), quartz, and the feldspars microcline and albite. Pyrite was the only sulfide mineral identified as an accessory phase. In the lithified clay horizons, dolomite

Line GeoB/AWI 96-024

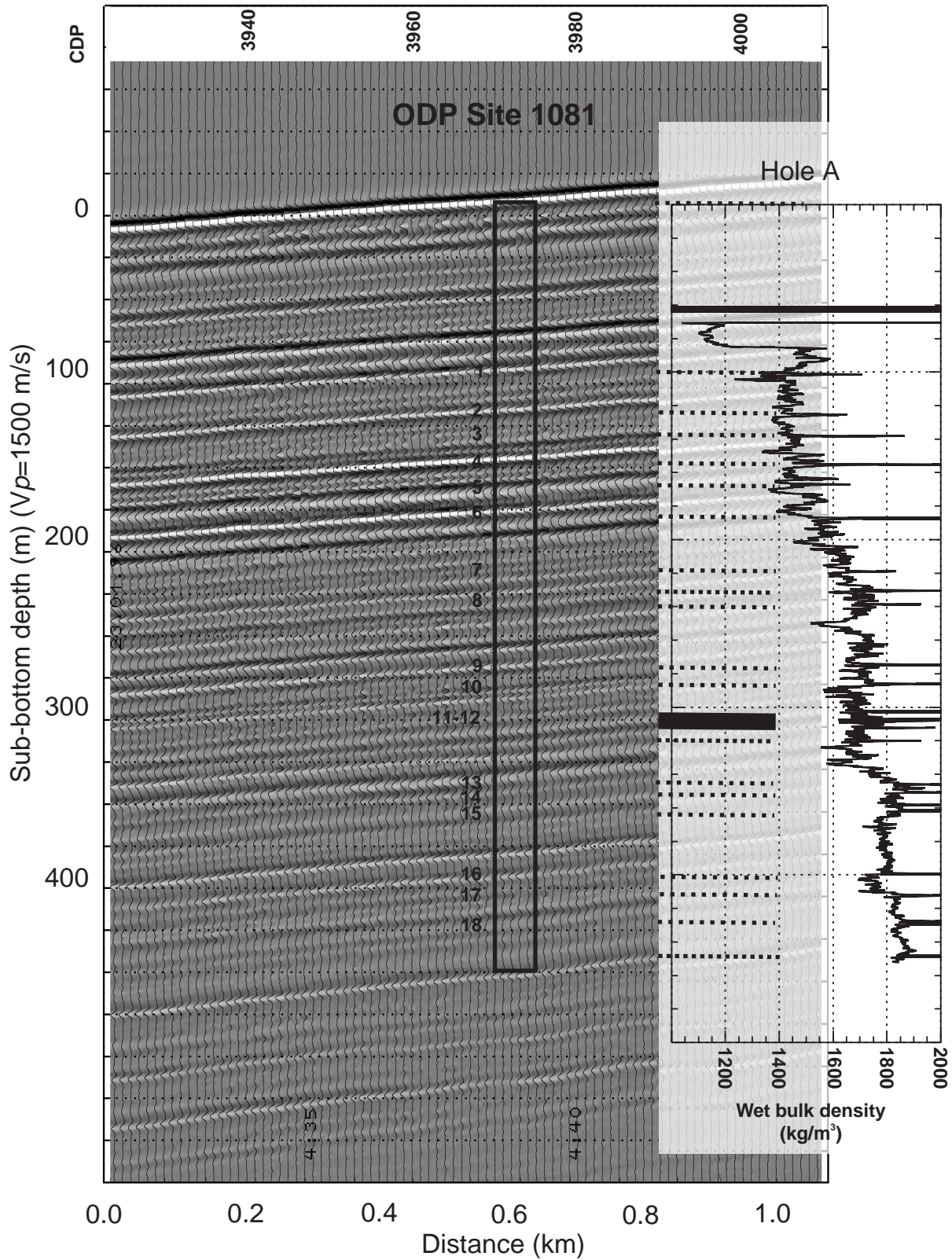


Figure 8. Close-up of Line GeoB/AWI 96-024 near Site 1081. Amplitudes are grayscale. For comparison, density data from downhole logging are shown. Consecutive numbers indicate occurrences of lithified intervals, dolomitic clays, or extreme GRAPE density values, all corresponding to peaks in density on the downhole log. Many peaks are associated with seismic reflectors (thick dashed lines). For depth determination, a sound velocity ( $V_p$ ) of 1500 m/s was used.

## Line GeoB/AWI 96-015

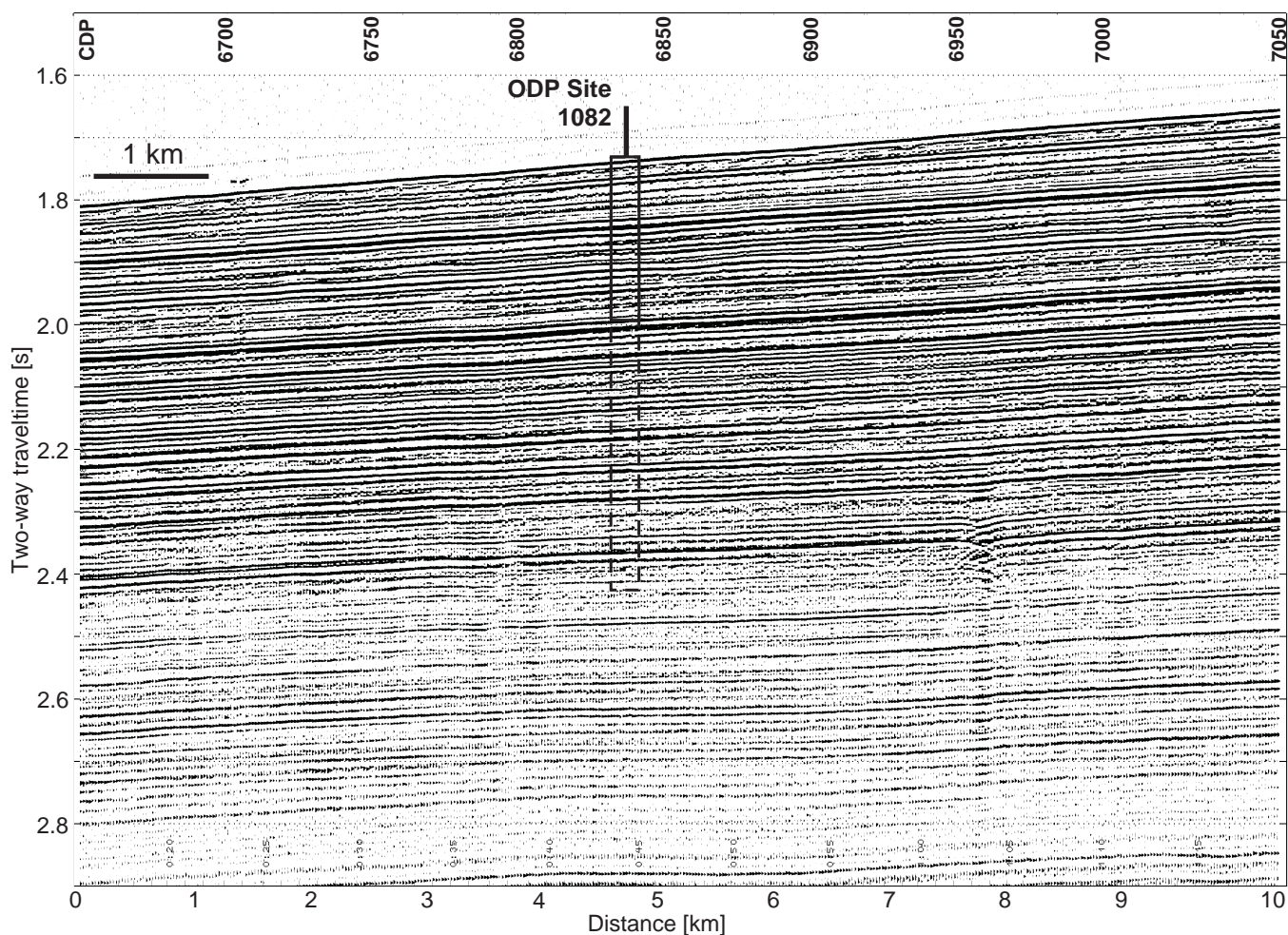


Figure 9. Seismic section of Line GeoB/AWI 96-015 at Site 1082. Vertical axis is given in TWT. CDP interval is 25 m for a shotpoint spacing of 25 m. Site 1082 is located at CDP 6837. The box indicates the approximate penetration of the borehole of 200 m (APC) and 600 m (XCB), respectively.

is identified, whereas external to these horizons, only minor amounts of dolomite are observed. The detected spacings of this mineral are slightly offset to larger lattices, which points to the formula  $\text{Ca}_{1.08}\text{Mg}_{0.92}(\text{CO}_3)_2$ . The detected biogenic components are calcite and opal. Calcite peak intensities are strongly correlated with measured calcium carbonate concentrations ( $r = 0.97$ ). Opal was measured from the height of the amorphous opal bulge according to the method of Eisma and van der Gaast (1971); the opal data are semiquantitative because no standard sample was available for calibration on board. The opal results are corroborated by the trends in the diatom abundance curves (Fig. 15).

Based on the downcore variations of quartz, albite, and microcline, the core can be subdivided into five parts (Fig. 16). A major transition coincides with the boundary between lithologic Subunits IC and IB at ~230 mbsf. Below this boundary, all three minerals covary, both in the long-term increase with time and in shorter term, low-amplitude variations. The variations are also visible in the opal record. Above this boundary, the three minerals decrease and the shorter term variations show higher amplitudes and are different for albite compared with quartz and microcline. This is the interval where the diatom abundances (see “Biostratigraphy and Sedimentation Rates” section, this chapter) and opal increase rapidly. In the upper part of Subunit IB, between ~175 and 100 mbsf, all three minerals

show different shorter term variations. For the long-term trend in this interval, quartz is high, as is opal. Between ~100 and 30 mbsf, the three minerals decrease in abundance, together with the opal counts and diatom abundance. In the shorter time scale, quartz and microcline show comparable variations, following the variations for opal. Above 30 mbsf, the three minerals show no correlation among one another or with opal.

The small grain size (silt sized) of quartz and feldspar, as observed from the smear slides, indicates an eolian origin. Their low-amplitude behavior and covariance with opal below ~235 mbsf suggest that the minerals reflect a relatively simple climatic system in which the force of the southeasterly trade winds controls the upwelling and the eolian input in late Miocene and early Pliocene times. The variations are too large to be explained solely by differences in dilution with calcium carbonate, although quartz and calcium carbonate are strongly negatively correlated (Fig. 17). Around the lower to upper Pliocene boundary (235 mbsf), the contribution of the eolian components starts to become decoupled, which implies that the character of the transport mechanisms or the source areas must have changed. A similar feature occurred around 2.2 Ma (175 mbsf), when the sources of quartz and microcline also became decoupled and the variations started to show higher amplitudes. The appearance and disappearance of the eolian transport mechanism may occur through the displacement

Line GeoB/AWI 96-015

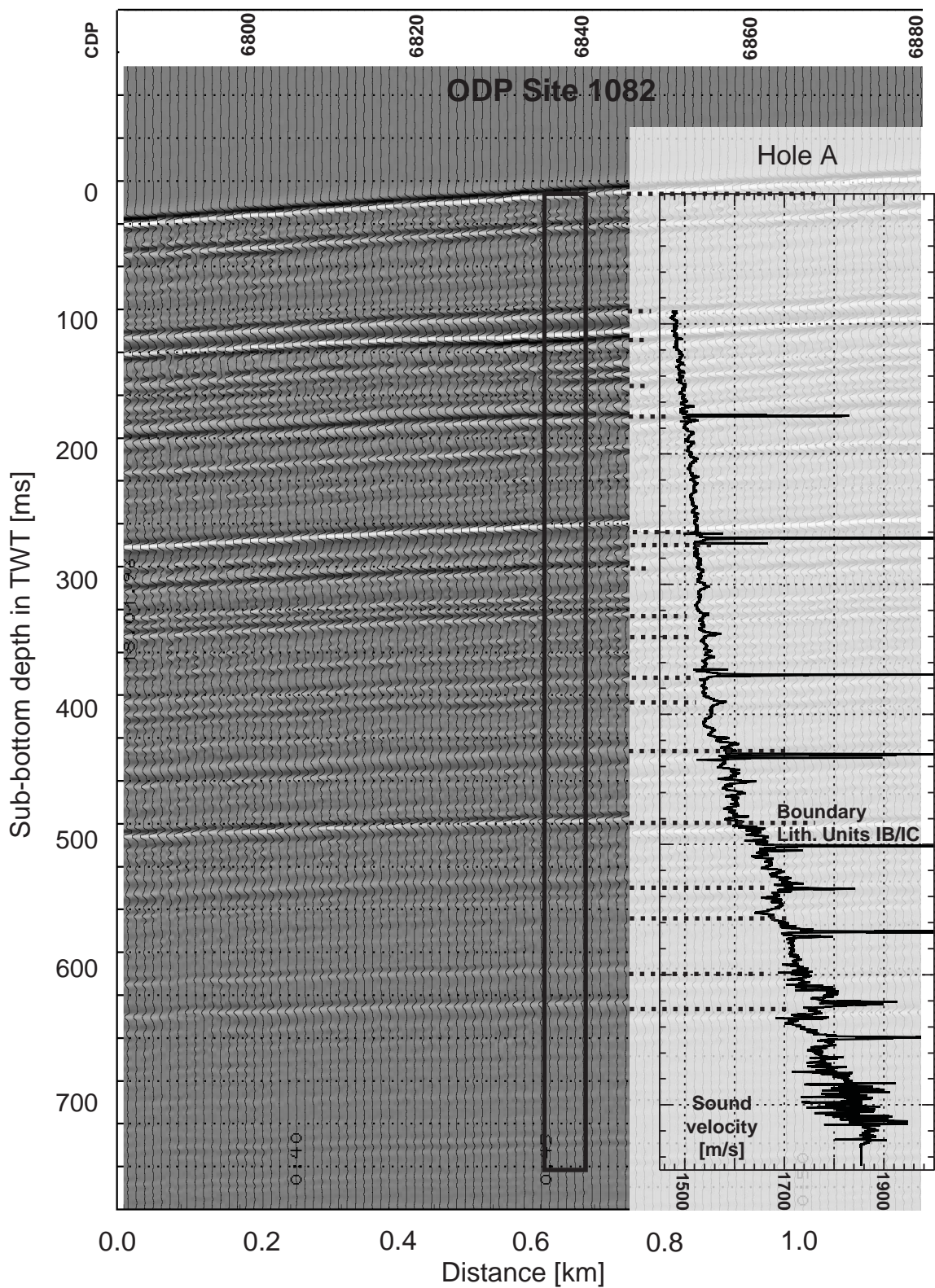


Figure 10. Close-up of Line GeoB/AWI 96-015 near Site 1082. Vertical axis is given in TWT. Amplitudes are grayscale. For comparison, the sound velocity profile from downhole logging is shown. Logging depth is transferred to TWT using the logging results. Selected reflectors can be correlated with local extremes in the velocity log (thick dashed lines), but density-controlled lithologic changes are not reflected in the logging data.

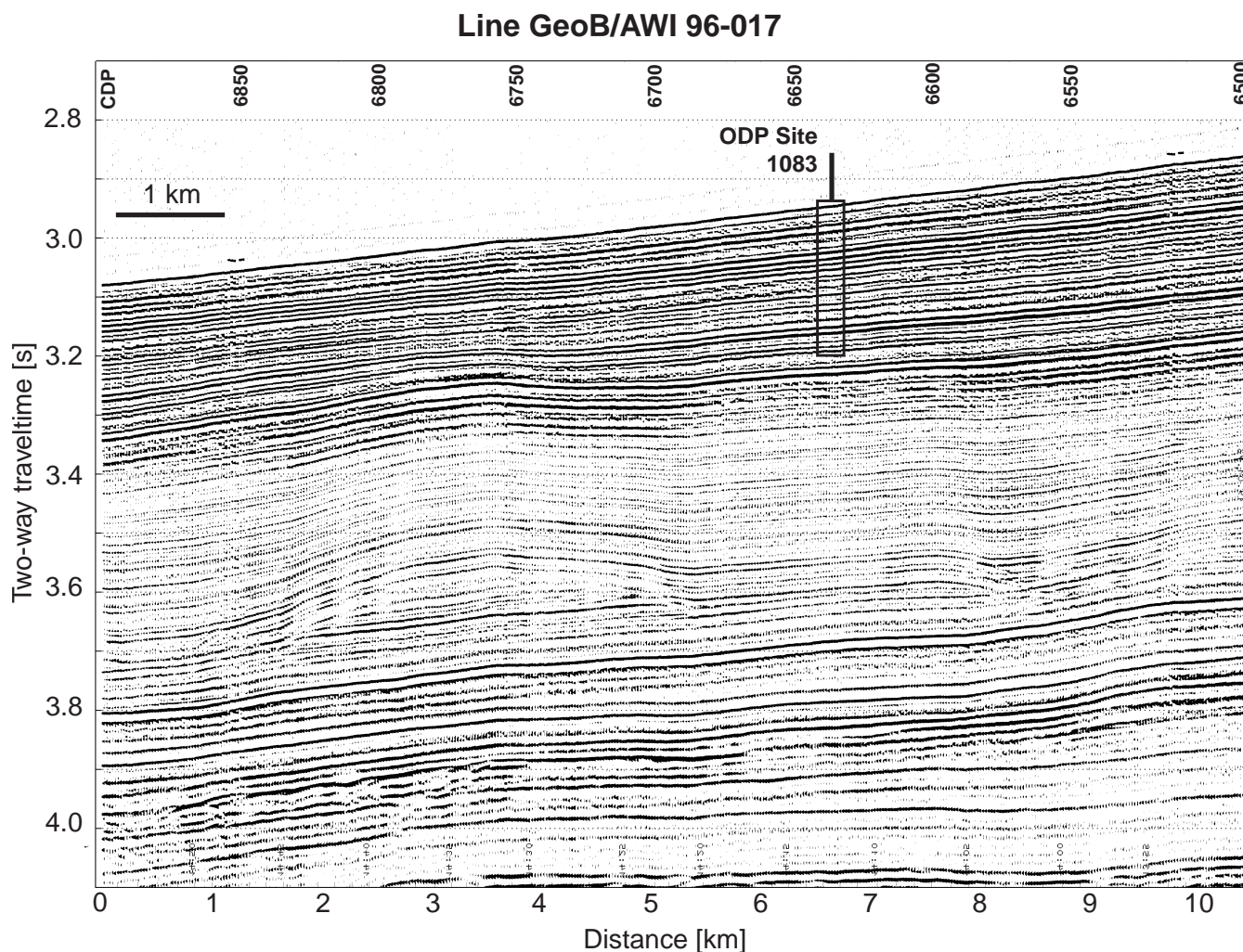


Figure 11. Seismic section of Line GeoB/AWI 96-017 at Site 1083. Vertical axis is given in TWT. CDP interval is 25 m for a shotpoint spacing of 25 m. Site 1083 is located at CDP 6642. The box indicates the approximate penetration of the borehole of 200 m (APC).

of the climatic system or by a change in the terrigenous source. Besides the southeasterly trade winds, the Namibian bergwinds (land winds that blow into the ocean particularly in the austral winter) are an important carrier of eolian sediments to the South Atlantic. These bergwinds may have become important during the early to late Pliocene transition either by their onset or because the southern African deserts originated during this period. The later, less well-defined transitions might then be caused by changes in the position and direction of the trade winds.

### Spectrophotometry

Color data were measured every 2 cm for Cores 175-1081A-1H through 9H. Cores 175-1081A-10H through 49X and all of Holes 1081B and 1081C were measured at 4-cm intervals. At Site 1081, total reflectance values range between 24% and 44%, and the red/blue (650 nm/450 nm) ratio varies between 1.1 and 1.6 (Fig. 18). This range is greater than that observed at Sites 1075–1080 (e.g., see “Litho-stratigraphy” section, “Site 1075” chapter, this volume).

The general trends in red/blue ratio, total reflectance, magnetic susceptibility, and GRAPE density can be correlated to the lithostratigraphic units and subunits defined for Hole 1081A (Fig. 18).

The magnetic susceptibility record seems to follow clay abundance in these sediments. Changing concentrations of organic carbon and calcium carbonate influence total reflectance and red/blue ratio in sediments from Site 1081, as well as bulk density.

In lithostratigraphic Subunit IA of Holes 1081A, 1081B, and 1081C, red/blue ratios and total reflectance values are high compared with the other subunits of Unit I (Fig. 18). Subunit IA is characterized by high calcium carbonate and organic carbon contents. The red/blue ratio is positively correlated with calcium carbonate, whereas total reflectance shows a weak negative correlation with organic carbon content (Fig. 19A, B). There is no relationship between calcium carbonate and total reflectance (Fig. 19C). This suggests that in Subunit IA, carbonate dominates the red/blue ratio, whereas the concentration of organic matter may influence the total reflectance.

In lithostratigraphic Subunit IB, total reflectance, and red/blue ratio values are lower than in Subunit IA; GRAPE density and magnetic susceptibility also have low values (Fig. 18). Compared with Subunit IA, Subunit IB has higher abundances of diatoms (see “Description of Lithostratigraphic Units” section, this chapter) but similar organic carbon content (see “Organic Geochemistry” section, this chapter; also see Fig. 18). No specific relationship is evident between total reflectance and organic carbon. We suggest that the high

Line GeoB/AWI 96-017

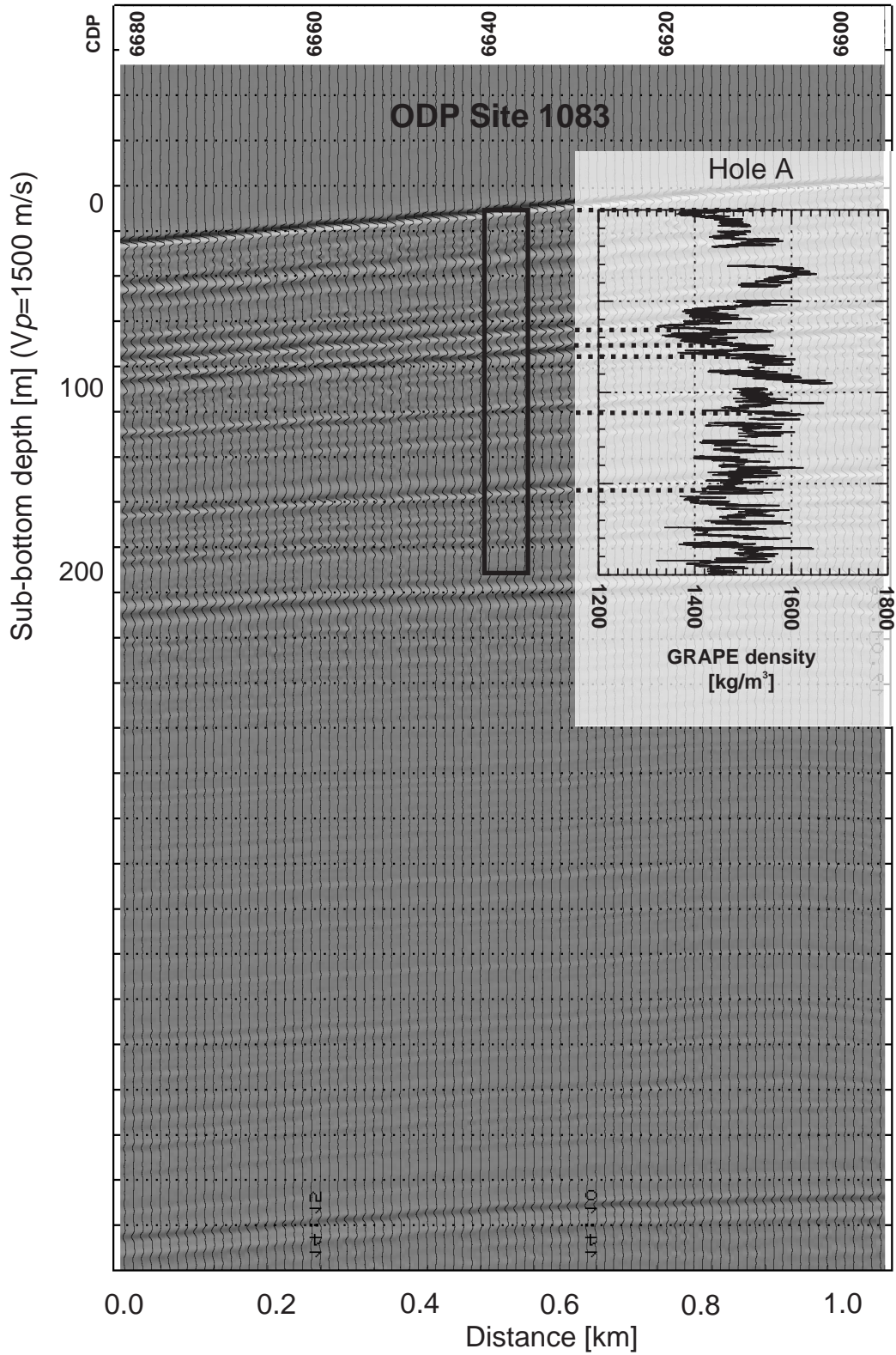


Figure 12. Close-up of Line GeoB/AWI 96-017 near Site 1083. Amplitudes are grayscale. For comparison, GRAPE density data from MST measurements are shown, and main reflectors are correlated with local extremes in the density log (thick dashed lines). For depth determination, a sound velocity  $V_p$  of 1500 m/s was used.

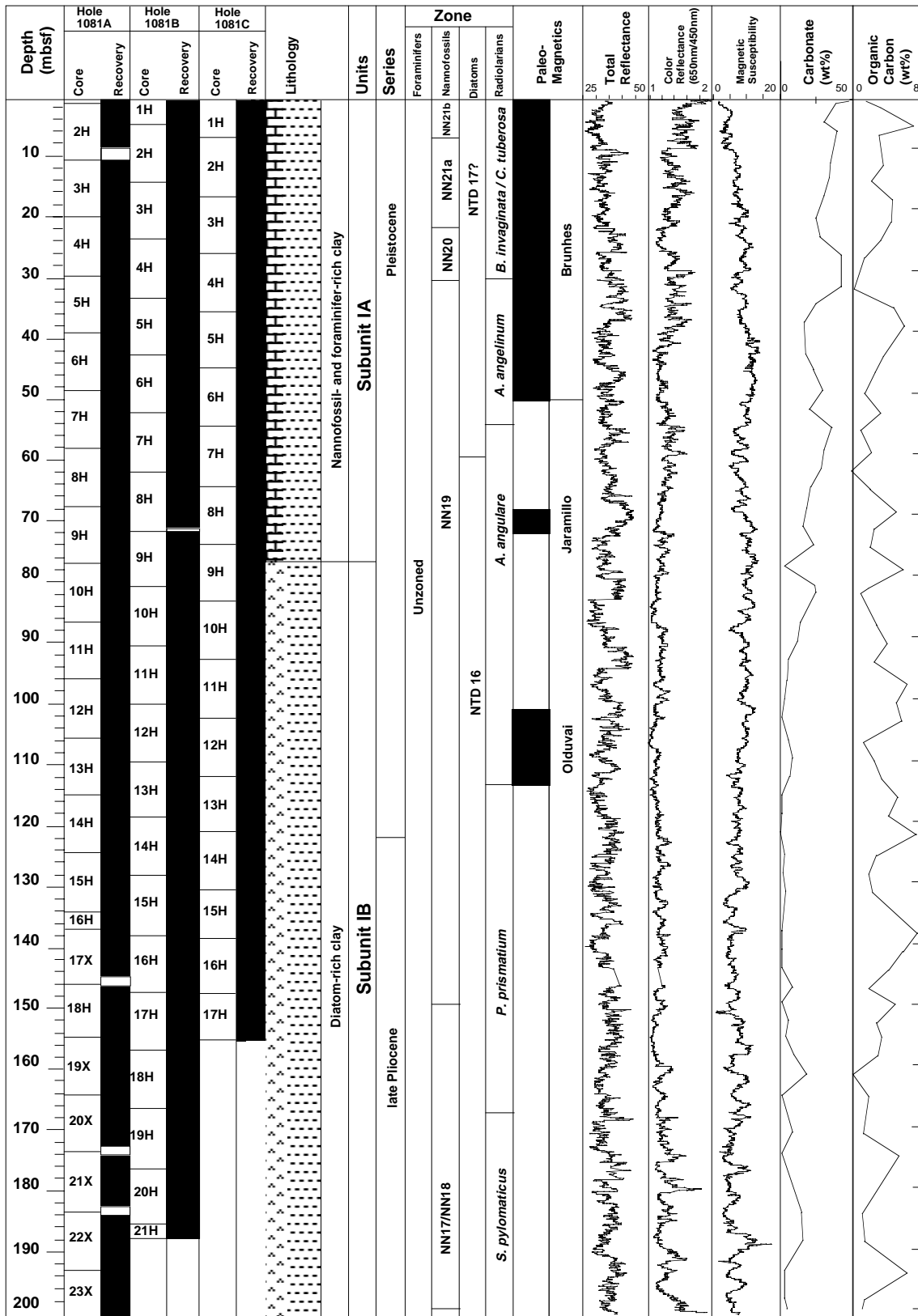


Figure 13. Composite stratigraphic section for Site 1081 showing core recovery in all holes, a simplified summary of lithology, age, total reflectance (400–700 nm), color reflectance (650 nm/450 nm), magnetic susceptibility, calcium carbonate, and organic carbon content. (Continued next page.)



Figure 13 (continued).

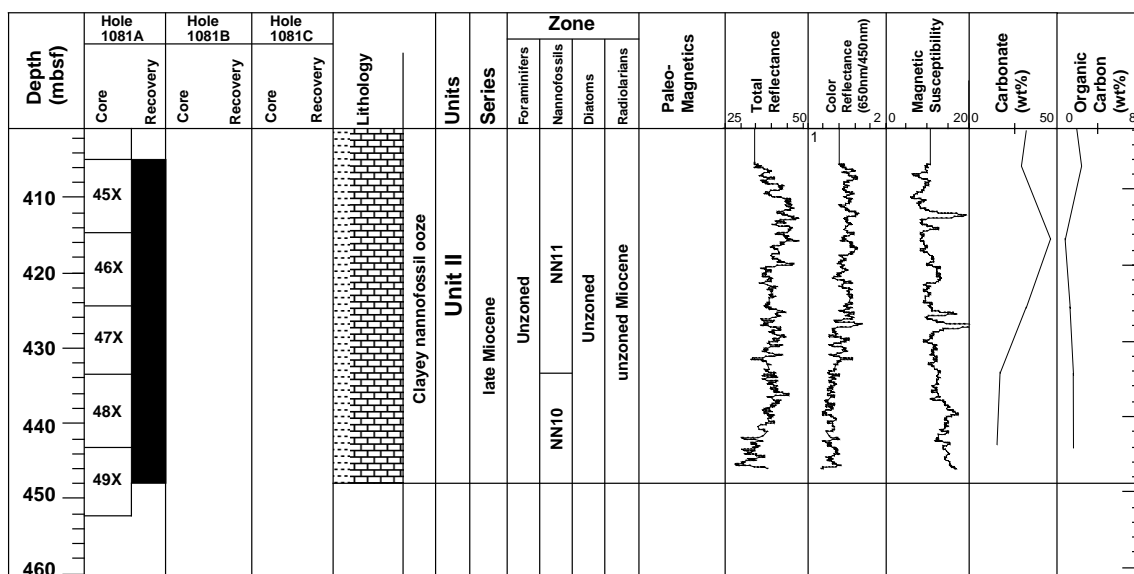


Figure 13 (continued).

abundances of diatoms in this subunit may attenuate the effect of organic carbon on total reflectance. Within Subunit IB, the highest red/blue ratios correspond to intervals containing dolomitized clays (see above), which is consistent with the high GRAPE density values.

Subunit IC has slightly higher red/blue ratios and total reflectance values than Subunit IB, as well as higher magnetic susceptibility and GRAPE density values (Fig. 18). Subunit IC contains more nannofossils and very few diatoms compared with Subunit IB. Over this interval, the organic carbon content decreases downcore, whereas the calcium carbonate content increases (see “Organic Geochemistry” section, this chapter). In this subunit, calcium carbonate content controls both total reflectance and red/blue ratios because the organic carbon content is so low (Fig. 19D, E). Similarly, in Unit II calcium carbonate content exerts the main control on color reflectance data (Fig. 19D, E).

## BIOSTRATIGRAPHY AND SEDIMENTATION RATES

Sediments recovered from Site 1081 represent a relatively continuous hemipelagic section spanning the last ~9 m.y. The micropaleontological studies were carried out on core-catcher samples from Hole 1081A. Additional samples from within the cores were examined for calcareous nannofossil- and diatom-based biostratigraphy. Because both siliceous and calcareous microfossil index species are present throughout this site, an integrated biostratigraphic framework can be established (Fig. 20; Table 2). Sedimentation rates are fairly constant within the late Miocene and early Pliocene (average of 4 cm/k.y.). Sedimentation rates within the late Pliocene are the highest recorded for Site 1081A (9–15 cm/k.y.), but they are reduced at the Pliocene/Pleistocene boundary (~7 cm/k.y.). With the exception of planktonic foraminifers, all microfossil groups (calcareous nannofossils, benthic foraminifers, diatoms, and radiolarians) show marked fluctuations in abundance (Fig. 21), which are reflected in the lithology (see “Lithostratigraphy” section, this chapter). Planktonic foraminifers are absent, rare, or replaced by pyrite from Sample 175-1081A-12H-CC to the bottom of the hole.

## Calcareous Nannofossils

Calcareous nannofossils were studied in core-catcher samples from Hole 1081A. Additional samples from within the cores were examined close to datum events to improve the stratigraphic resolution. Overall abundance ranges from abundant to very abundant within the upper (Cores 175-1081A-1H through 9H) and lower parts of the section (Cores 175-1081A-39X through base). Samples from Cores 175-1081A-10H through 25X are commonly barren or poor in calcareous nannofossils (Fig. 21), although some nannofossil-rich sediment occasionally is found within narrow intervals (lower part of Core 14H; upper part of Core 18H; upper part of Core 21H). A third unit spanning Cores 175-1081A-26X through 38X contains common to abundant nannofossils. Preservation is good to very good except within the barren and nannofossil-poor interval, which commonly contains heavily etched and dissolved specimens.

Within the sampling resolution, the sedimentation appears continuous throughout the entire section (Fig. 20). Site 1081 terminated in the late Miocene within Zone NN10. Based on the oldest identified calcareous nannofossil datum, the bottom age is estimated at  $9 \pm 0.2$  Ma.

The nannofossil-based biostratigraphy of the Neogene part of Site 1081 is imperfectly constrained because of the scarcity of index species. Most of the biohorizons used to define the Miocene and Pliocene are based on the first occurrence (FO) or last occurrence (LO) of *Discoaster* species. These datum events are difficult to find in high latitudes, marginal seas, and eastern boundary current areas. Also, the other marker species belong to genera (i.e., *Amaurolithus*, *Ceratoolithus*, and *Triquetrorhabdulus*) that are more common in low latitudes. Consequently, the Zone NN18/NN17, NN15/NN14, and NN14/NN13 boundaries could not be identified within this section.

### Zone NN21

This zone covers the last 21.9 mbsf of Hole 1081A. The FO of the *Emiliana huxleyi* acme, which defines the Zone NN21b/NN21a boundary, is between Samples 175-1081A-2H-1, 100 cm, and 2H-4, 90 cm.

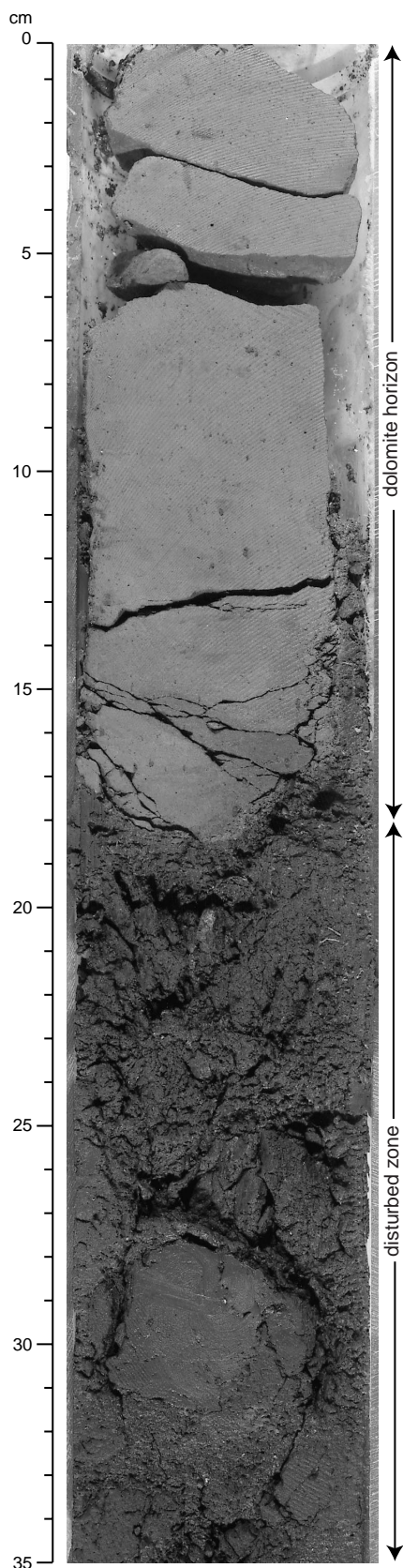


Figure 14. Photograph of a dolomite horizon in interval 175-1081A-17X-1, 0–18 cm.

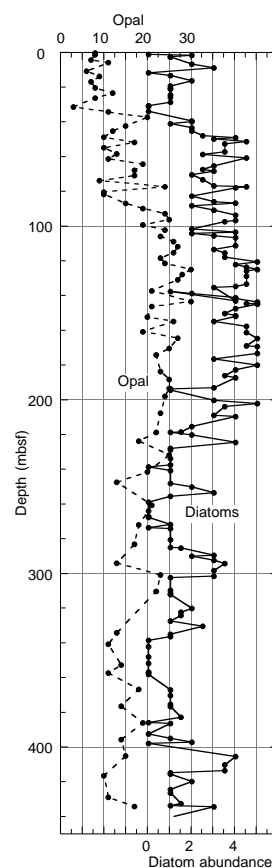


Figure 15. Downcore variation in opal (XRD counts) and diatom abundance (see “Biostratigraphy and Sedimentation Rates” section, this chapter).

**Zone NN20**

This interval spans 0.2 m.y. from the middle of oxygen-isotope Stage 8 to the middle of isotope Stage 12. The LO of *Pseudoemiliana lacunosa*, the datum event for the Zone NN20/NN19 boundary, was identified between Samples 175-1081A-4H-CC and 5H-2, 120 cm.

**Zone NN19**

In addition to the zonal boundary events, five biohorizons are identified within this interval. These are the LO of the Small *Gephyrocapsa acme* (0.6 Ma; Weaver, 1993) at 40.81 mbsf; the LO of *Reticulofenestra asanoi* (0.83 Ma) at 54 mbsf; the LO of Small *Gephyrocapsa acme* (0.96; Gartner, 1977) at 63.69 mbsf; the LO of *Helicosphaera sellii* (1.25 Ma) at 83.46 mbsf; and the LO of *Calcidiscus macintyreii* (1.67 Ma) at 107.88 mbsf.

**Zones NN18–NN17**

The top of Zone NN18 is defined by the disappearance of the last *Discoaster* species, *D. brouweri* (between Samples 175-1081A-18H-1, 93 cm, and 18H-4, 80 cm). This species is one of the few star-shaped calcareous nannofossils to be found consistently within the Neogene interval of Hole 1081A. *D. pentaradiatus*, whose LO event is used to define the Zone NN18/NN17 boundary, is too sparse within the late Pliocene part of the section to allow for a clear definition of this zonal boundary.

**Zone NN16**

The datum event for the Zone NN17/NN16 boundary (LO of *D. surculus*) was identified between Samples 175-1081A-23X-5, 80 cm,

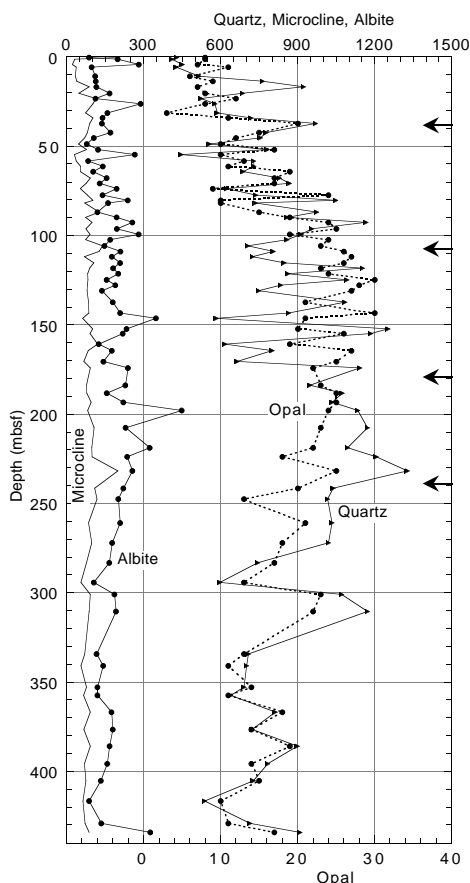


Figure 16. Downcore variation in quartz, albite, microcline, and opal. Horizontal axes are XRD counts. Arrows subdivide figure into the five parts discussed in the text.

and 23X-CC. The base of this zone is defined by the LO event of one of the few non-*Discoaster* marker species of the Neogene, *Reticulofenestra pseudoumbilica*. This datum (3.82 Ma) occurs slightly before the late/early Pliocene boundary and can therefore be used to approximate this epoch boundary.

#### Zones NN15, NN14, NN13, and NN12

This interval spans 1.72 m.y. between 5.54 and 3.82 Ma. The horseshoe-shaped calcareous nannofossils of the genera *Amaurolithus*, *Ceratolithus*, and *Triquetrorhabdulus*, which define the various zonal boundaries within this interval, are virtually absent from the analyzed samples. The Zone NN12/NN11 boundary was identified between Samples 175-1081A-34X-CC and 35X-2, 120 cm.

#### Zone NN11

This interval is defined by the range of *D. quinquaramus* and its synonym species *D. berggrenii*. The FO of *D. quinquaramus* (Zone NN11/NN10 boundary) was identified within Core 175-1081A-47X at the mean depth of 430.50 mbsf.

#### Zone NN10

The presence of *D. loeblichii* and *D. neorectus*, two species restricted to Zone NN10 within Samples 175-1081A-47X-CC and 48X-CC, confirms that Site 1081 terminated within this interval.

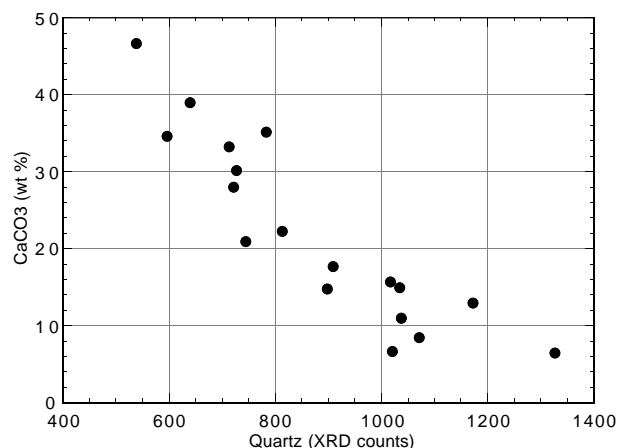


Figure 17. Crossplot of quartz (XRD counts) and calcium carbonate concentrations (see "Organic Geochemistry" section, this chapter) for the depth interval 230–440 mbsf.

### Planktonic Foraminifers

The uppermost assemblage is dominated by *Globigerinoides sacculifer* and *Globigerina bulloides*, and *Hastigerina siphonifera* is abundant. *Neogloboquadrina pachyderma* (dextral), *Orbulina universa*, *Globorotalia truncatulinoides*, *Globigerinella calida*, *Globigerinoides ruber*, *Globigerina falconensis*, *Globigerinoides sacculifer*, *Globigerina quinqueloba*, and *Globorotalia crassaformis* also are present (Table 3). This assemblage is a mixture of warm-water fauna associated with the Angola Current and cool-water fauna. *N. pachyderma* (dextral) and *G. bulloides* are common in the fringes of upwelling cells and are associated with the Benguela Coastal Current (Little et al., 1997). There is little downcore variation (Table 3). Tropical species, *Globorotalia menardii* and *Globorotalia tumida*, are present in Samples 175-1081A-6H-CC and 7H-CC and may indicate intervals of strong Angola Current flow. Sample 175-1081A-9H-CC is barren, and Samples 175-1081A-10H-CC and 11H-CC contain rare planktonic foraminifers (Table 3).

The majority of the core is affected by dissolution and pyritization. Samples 175-1081A-12H-CC through 24X-CC, 26X-CC, 28X-CC, 29X-CC, and 31X-CC through 35X-CC are barren. Planktonic foraminifers in Samples 175-1081A-37X-CC through 49X-CC are replaced by pyrite, although Samples 37X-CC, 41X-CC, and 43X-CC contain a trace of unreplaced foraminifers. Foraminifers in Sample 49X-CC are completely replaced. Samples 175-1081A-25X-CC and 30X-CC contain only trace numbers of planktonic foraminifers. Assigning the planktonic foraminifers to zones is difficult because of the generally very low abundance and lack of index fossils. Samples 25X-CC through 49X-CC probably are Pliocene to late Miocene in age.

In Sample 175-1081A-25X-CC, planktonic foraminifers are rare. *Globorotalia puncticulata* is present, but *G. inflata* is absent. This absence may be caused by dissolution, but it may also be an evolutionary event. The first-appearance datum for *G. inflata* occurs in the late Pliocene. Sample 175-1081A-30X-CC contains only trace amounts of foraminifers. The age is constrained to the late Miocene to Pliocene based on the presence of *Globigerinoides woodi*, which ranges from the late Oligocene to late Pliocene, and on *N. pachyderma*, which ranges from the late Miocene to the Holocene (Kennett and Srinivasan, 1983).

Samples 175-1081A-37X-CC to the base of the section are of Miocene age. The boundary may be higher in the section (e.g., 175-1081A-34X-CC), as suggested by the other microfossil groups, but

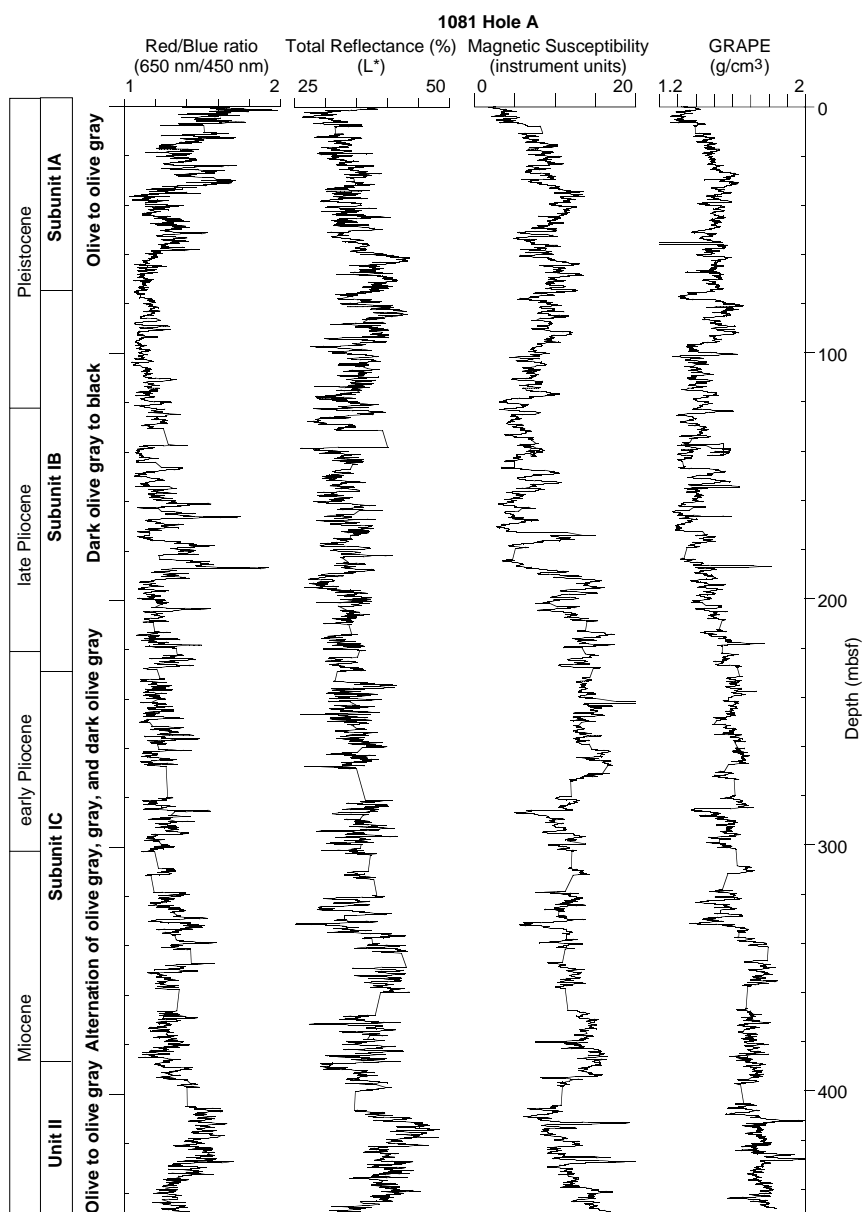


Figure 18. Stratigraphic variation in the red/blue ratio (650 nm/450 nm), total reflectance, magnetic susceptibility, and GRAPE density at Hole 1081A. Ages (see “Biostratigraphy and Sedimentation Rates” section, this chapter), lithostratigraphic subunits, and the main color changes based on the Munsell Color Chart are indicated.

the interval is barren of planktonic foraminifers. Furthermore, most of the samples below 37X-CC are pyritized. Replacement by pyrite destroys some diagnostic information, such as wall structure and tooth preservation, and renders the zonation tentative.

The few existing foraminifers in Sample 175-1081A-37X-CC were tentatively identified as *Globorotalia conoidea* (middle to late Miocene) and *D. altispira* (early Miocene to late Pliocene). Sample 175-1081A-39X-CC provides some stratigraphic control for the base of the core: the presence of *G. conoidea* indicates an age of middle to latest Miocene. *Sphaeroidinellopsis seminulina* is also present. Sample 175-1081A-41X-CC contains *N. pachyderma* and *G. conoidea* and is of late Miocene age. Sample 175-1081A-43X-CC has very few specimens, which only constrains the age to the Miocene: *Sphaeroidinellopsis seminulina seminulina*, *Orbulina universa*, and *Globigerinella obesa*; however, the assemblage in Sample 175-1081A-46X-CC is constrained to the late Miocene by the presence of *N. acostaensis*, *G. conoidea*, *G. sacculifer*, *O. universa*, and *S. seminulina seminulina*. Samples 175-1081A-47X-CC through 49X-CC contain *Globorotalia conoidea* (middle to latest Miocene).

### Benthic Foraminifers

The absolute abundance of benthic foraminifers is high in Samples 175-1081A-1H-CC through 8H-CC (Fig. 21). This interval is followed by an interval comprising Samples 175-1081A-9H-CC through 17X-CC that are barren or have very low abundance (Table 4). Before this, there is a succession of barren samples or samples with low abundances alternating with samples showing high abundance of benthic foraminifers. In general, preservation follows the absolute abundance pattern, suggesting that the absolute abundance reflects the degree of dissolution.

Only a few benthic foraminifer species are present throughout the entire Hole 1081A. *Uvigerina auferiana* is present in high relative abundance (between 4% and 89%, average 41%) in the pre-Pleistocene interval (Samples 175-1081A-14H-CC through 49X-CC) disregarding barren samples, samples with lithified sediment, and samples with too few specimens on which to base reliable percentage estimates. This species is also present in the Pleistocene part of Hole 1081A (Samples 175-1081A-1H-CC through 10H-CC), but in lower

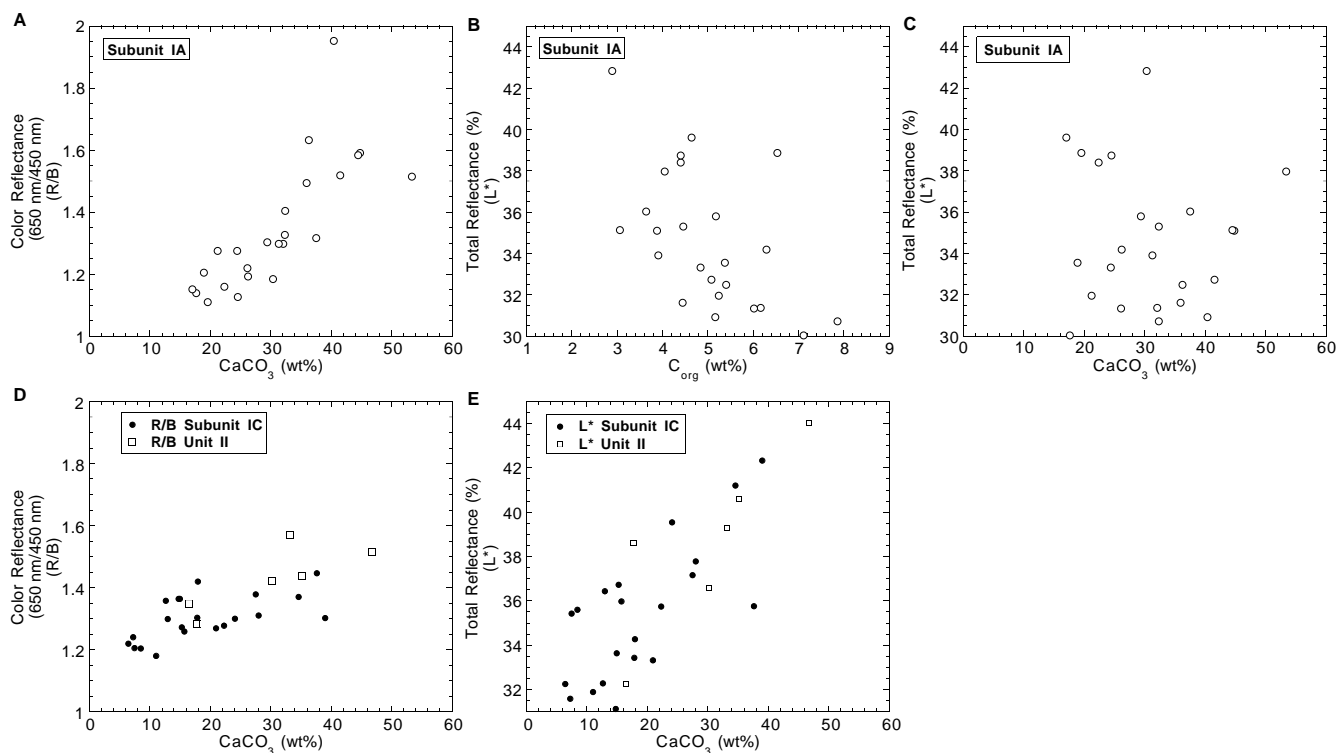


Figure 19. Comparison between calcium carbonate and organic carbon contents (in weight percent) with the red/blue wavelength spectral ratio and total reflectance for lithostratigraphic units at Hole 1081A. A–C. Subunit IA. D–E. Subunit IC and Unit II.

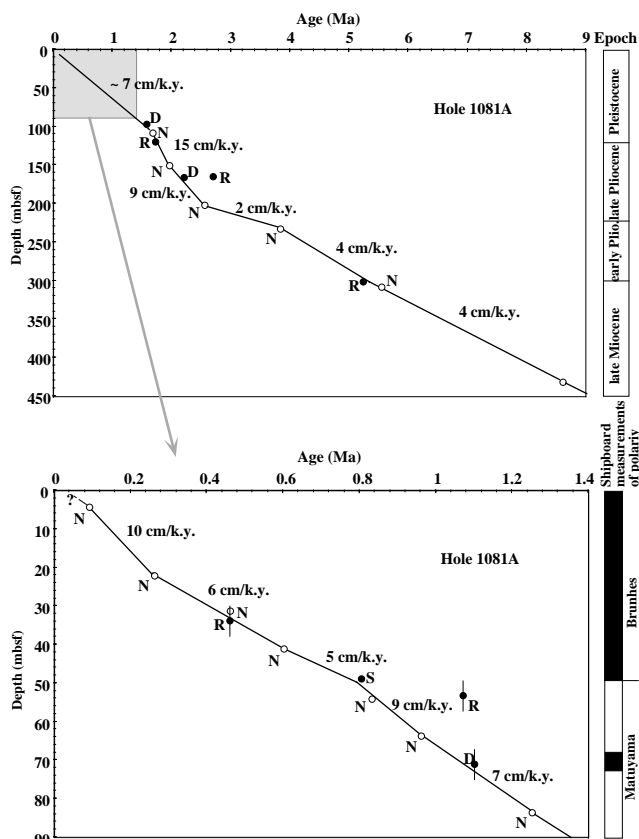


Figure 20. Age-depth plot and sedimentation rates estimated from calcareous nannofossil (open circles) and siliceous microfossil (solid circles; D = diatoms, R = radiolarians, and S = silicoflagellates) datums at Hole 1081A.

relative abundance (between 1% and 21%, average 5%). Other species present throughout Hole 1081A are *Globocassidulina subglobosa* and *Oridorsalis umbonatus*, although they are present in much lower relative abundance compared to *Uvigerina auberiana* (generally <5% each).

Species restricted to, or with their highest abundance in, the Pleistocene are *Bolivina* sp. 1, *Bolivina* sp. 2, *Bulimina aculeata*, *Bulimina marginata*, and *Cassidulina laevigata*, (Table 4; Fig. 22). The late Pliocene is dominated by *Bulimina exilis* and *Uvigerina auberiana* (between 25% and 90%, average 67%; Fig. 22). The early Pliocene is characterized by high abundance of *Cibicidoides pachyderma*, stiliostomellas (often broken), and *Uvigerina auberiana*. The upper part has high abundance of the arenaceous species *Siphotextularia concava*, whereas the lower part has high abundance of *Trifarina* sp. 1. *Siphotextularia concava* seems to be restricted to an interval covering the early/late Pliocene boundary. The Miocene section of Hole 1081A is dominated by *Cibicidoides pachyderma* and *Uvigerina auberiana*, with contributions from several species (e.g., *Cibicidoides bradyi*, *Globocassidulina subglobosa*, *Oridorsalis umbonatus*, and stiliostomellas). The species *Cibicidoides bradyi* is not found in post-Miocene sediments at Hole 1081A, whereas *Cibicidoides pachyderma* and *Sigmolinopsis schlumbergeri* seem to be restricted to the Miocene and early Pliocene.

## Radiolarians

Radiolarians are present in most of the core-catcher samples of Hole 1081A (Table 5). In the upper sequence, radiolarians are generally abundant and well preserved. In the lower sequence, radiolarians are rare and show signs of dissolution, although concentrations by the sample preparation often produce high abundances of radiolarians in the assemblage slides. Radiolarian fauna indicates a Quaternary to late Miocene age for Hole 1081A. No apparent reworking has been identified.

**Table 2. Microfossil datums at Hole 1081A.**

Fossil group	Event	Age (Ma)	Zone (base)		Core, section, interval (cm)		Depth (mbsf)		
			A	B	Top	Bottom	Top	Bottom	Mean
N	FO <i>Emiliana huxleyi</i> acme	0.09	NN21b		175-1081A-2H-1, 100	175-1081A-2H-4, 90	2.00	6.40	4.20
N	FO <i>Emiliana huxleyi</i>	0.26	NN21a	CN15	3H-CC	4H-3, 80	20.05	23.80	21.93
N	LO <i>Gephyrocapsa caribbeanica</i> acme	0.26	NN21a	CN15	3H-CC	4H-3, 80	20.05	23.80	21.93
N	LO <i>Pseudoemiliana lacunosa</i>	0.46	NN20	CN14b	4H-CC	5H-2, 120	29.93	32.20	31.07
R	LO <i>Axoprunum angelinum</i>	0.46			2H-CC	5H-CC	8.22	39.12	23.67
N	LO Small <i>Gephyrocapsa</i> acme (Weaver, 1993)	0.60			5H-CC	6H-3, 50	39.12	42.50	40.81
S	LO <i>Bachmannocena quadrangula</i>	0.80			5H-CC	6H-CC	39.12	48.52	43.82
N	LO <i>Reticulofenestra asanoi</i>	0.83			7H-3, 30	7H-6, 30	51.80	56.20	54.00
N	LO Small <i>Gephyrocapsa</i> acme (Gartner, 1977)	0.96			8H-3, 98	8H-5, 130	61.98	65.20	63.59
R	LO <i>Lamprocyrtis neoheteroporos</i>	1.07			6H-CC	7H-CC	48.52	58.03	53.28
D	LO <i>Rhizosolenia matuyama</i>	1.10			9H-2, 80	9H-4, 80	69.80	72.70	71.25
N	LO <i>Helicosphaera sellii</i>	1.25			10H-3, 60	10H-CC	80.60	86.31	83.46
D	LO <i>Rhizosolenia praebergonii</i> var. <i>robusta</i>	1.65			11H-CC	12H-1, 90	96.12	96.90	96.51
N	LO <i>Calcidiscus macintyreii</i>	1.67			12H-CC	13H-4, 70	105.05	110.70	107.88
D	LO <i>Proboscia barboi</i>	1.68			12H-CC	13H-1, 70	105.05	106.20	105.63
R	LO <i>Cycladophora pliconica</i>	1.83			13H-CC	14H-CC	114.87	124.50	119.69
N	LO <i>Discoaster browleri</i>	1.95	NN19	CN13a	18H-1, 93	18H-4, 80	146.93	151.25	149.09
D	LO <i>Thalassiosira convexa</i>	2.19			19H-CC	20X-3, 125	164.17	168.35	166.26
N	LO <i>Discoaster surculus</i>	2.55	NN17	CN12c	23X-5, 80	23X-CC	199.90	201.81	200.86
R	FO <i>Cycladophora davisiana</i>	2.70			19X-CC	20X-CC	164.17	172.90	168.54
N	LO <i>Reticulofenestra pseudoumbilicus</i>	3.82	NN16	CN12a	26X-CC	27X-2, 140	228.28	234.40	231.34
R	FO <i>Spongurus pylomaticus</i>	5.20			33X-CC	34X-CC	298.07	302.14	300.11
N	LO <i>Discoaster quinqueramus</i>	5.54	NN12	CN10a	34X-CC	35X-2, 120	302.14	311.30	306.72
N	FO <i>Discoaster quinqueramus</i>	8.60	NN11	CN9a	47X-4, 30	47X-6, 30	429.00	432.00	430.50

Notes: Fossil group: N = calcareous nannofossils, R = radiolarians, S = silicoflagellates, D = diatoms. FO = first occurrence and LO = last occurrence. Zonal codes refer to the standard calcareous nannofossil zonations of (A) Martini (1971) and (B) Okada and Bukry (1980).

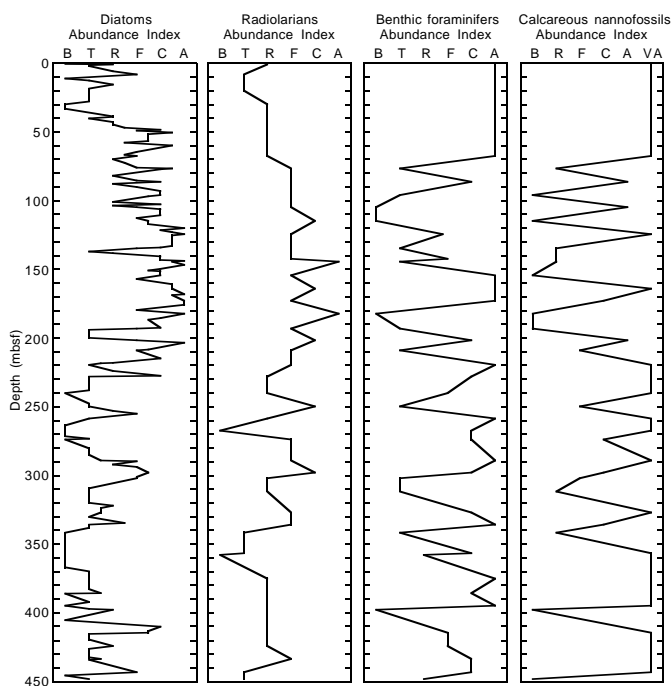


Figure 21. Downhole abundance fluctuations of opaline (diatoms and radiolarians) and calcareous (benthic foraminifers and nannofossils) microfossils at Hole 1081A. The abundance definitions for diatoms, radiolarians, and calcareous nannofossils are given in the “Biostratigraphy” section, “Explanatory Notes” chapter (this volume). The abundance definition of benthic foraminifers is given in the caption of Figure 22.

**Table 3. Relative abundance, presence or absence, and overall abundance of Pleistocene planktonic foraminifers at Hole 1081A.**

Core, section, interval	Depth (mbsf)	Overall abundance	<i>Orbulina universa</i>	<i>Globigerina bulloides</i>	<i>Hastigerina siphonifera</i>	<i>Globorotalia inflata</i>	<i>Globorotalia menardii</i> / <i>Globorotalia tumida</i>	<i>Globorotalia conoidea</i>
175-1081A-1H-CC	0.89	5		D	A	D		
2H-CC	8.22	5		D		D		
4H-CC	29.93	5	A	A		D		
5H-CC	39.12	5		A		D		
6H-CC	48.52	5	A	A		D	P	
7H-CC	58.03	5		A		D	P	
8H-CC	67.71	4		A		D		
9H-CC	76.72	0						
11H-CC	96.12	1		D				
37X-CC	336.05	1						P
38X-CC	341.81	1						
39X-CC	356.68	1						P
40X-CC	357.95	1						
41X-CC	375.23	1						P
42X-CC	385.77	1						
43X-CC	394.91	1						
44X-CC	397.79	1						
45X-CC	414.69	1						
46X-CC	424.31	1						P

Notes: Relative abundance is reported for Samples 175-1081A-1H-CC through 11H-CC, where D = dominant (>30%) and A = abundant (10%–30%). Sample 9H-CC is barren. The presence (P) of *G. menardii* is noted and indicates warm water (possibly the Angola Current). The presence of *G. conoidea* indicates an age of middle to latest Miocene, assuming no reworking. Overall abundance: 0 = absent; 1 = trace; 4 = common; and 5 = abundant.



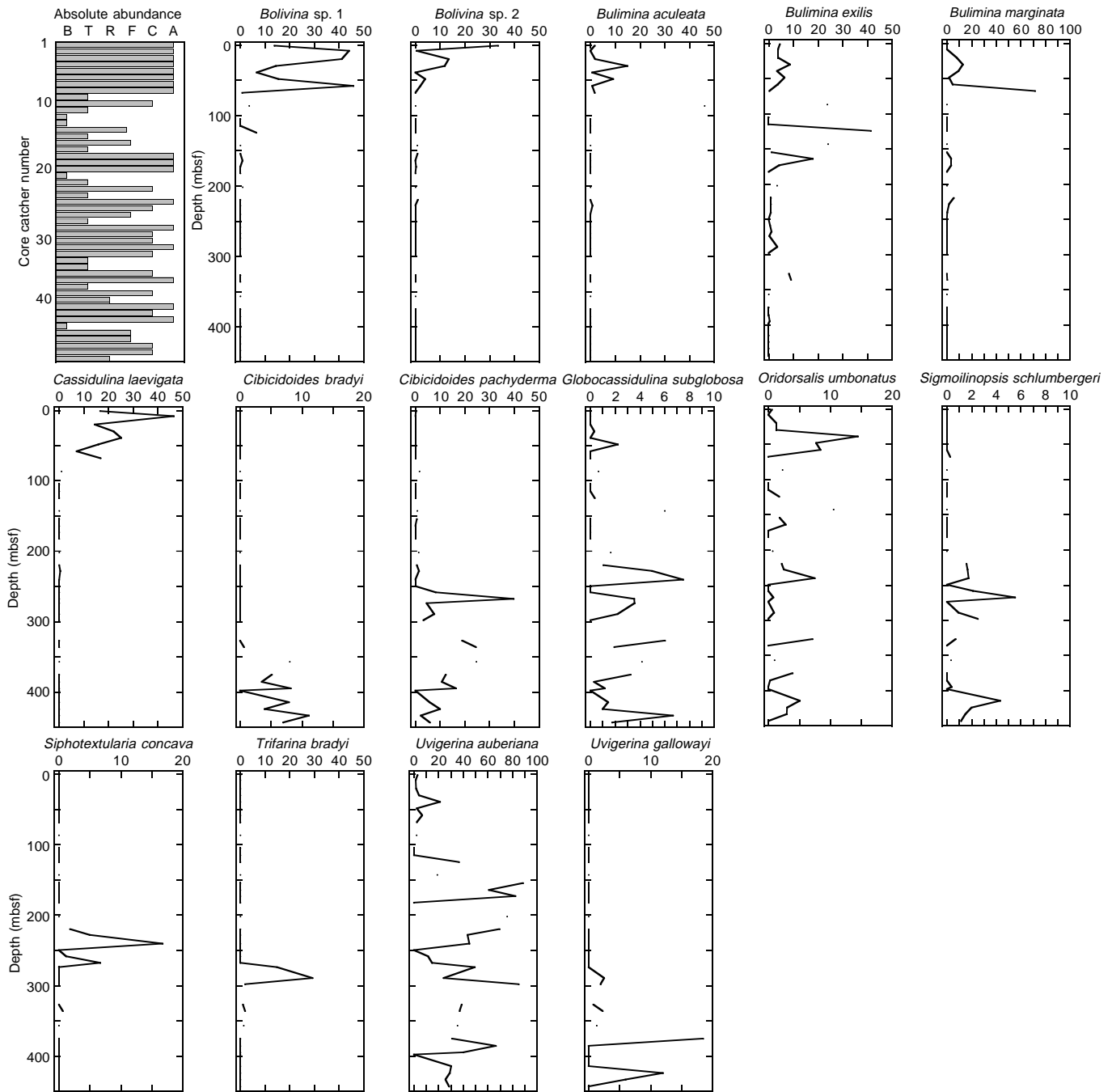


Figure 22. Relative abundances (in percentages) for selected benthic foraminifer species. Absolute abundance (per ~20 cm<sup>3</sup> of sediment) of benthic foraminifers are given as follows: A = abundant (>500 specimens); C = common (250–500 specimens); F = few (100–249 specimens); R = rare (50–99 specimens); T = trace (1–49 specimens); and B = barren (no specimens). Note that some samples are barren or contain very few specimens (Samples 175-1081A-9H-CC, 11H-CC through 13H-CC, 15H-CC, 17X-CC, 21X-CC, 22X-CC, 24X-CC, 28X-CC, 34X-CC, 35X-CC, 38X-CC, 40X-CC, 44X-CC, and 49X-CC), and that no reliable percentage estimates could be obtained.

The radiolarian zones used for this hole are those of Moore (1995) and Motoyama (1996). There are some difficulties in applying the established tropical and Antarctic zonations (Sanfilippo et al., 1985; Lazarus, 1992) because of the absence of index species such as *Pterocanium prismatium*, *Spongaster pentas*, *Diartus hughesi*, *Helotholus vema*, *Prunopyle titan*, and *Amphymenium challengerae*, and because of the extended occurrences up to the uppermost Pleistocene of *Eucyrtidium calvertense* and *Pterocanium trilobum*, which became extinct in the Pliocene or earlier Pleistocene in the Antarctic Ocean.

The absence of *Axoprunum angelinum* indicates that the uppermost cores (175-1081A-1H-CC and 2H-CC) are within either the Pleistocene *Collosphaera tuberosa* Zone or the Pleistocene to Holocene *Buccinosphaera invaginata* Zone of Moore (1995). A finer zonal resolution could not be achieved because of the absence of *B. invaginata*.

Although the diagnostic species *Anthocyrtidium angulare* is absent throughout the core, Samples 175-1081A-5H-CC and 6H-CC are approximately assigned to the Pleistocene *A. angelinum* Zone or



part of the *Cycladophora sakaii* Zone to the *S. pylomaticus* Zone in the North Pacific (Motoyama, 1996).

In the lower sequence below Sample 175-1081A-33X-CC, the fauna consists mainly of *Spumellaria*, and age-diagnostic forms are sparse. Therefore, no zones are defined for Samples 175-1081A-34X-CC through 49X-CC. The rare occurrences of tropical zonal marker species *Didymocyrtis antepenultima* within Samples 42X-CC, 46X-CC, 47X-CC, and 48X-CC possibly indicate that these samples belong to the middle part of the late Miocene *D. antepenultima* Zone. The presence of *Stichocorys peregrina* probably indicates that the deepest sample (49X-CC) is no older than ~ 9 Ma, because its FO approximates that age in the high-latitude Southern Ocean (Lazarus, 1992), although the FO of this species is at ~7 Ma in the tropical region.

*S. peregrina* seems to prefer tropical to temperate oceanographic conditions (Motoyama, 1996). Its last (common) occurrence is highly variable in age in different places; it disappeared in the late Miocene (~6.8 Ma) in the high-latitude North Pacific, whereas it became extinct at 2.6 Ma in the tropical region. At Hole 1081A, *S. peregrina* disappeared in Sample 175-1081A-24X-CC, far below the FO of *C. davisiana* (2.7 Ma). The presence of *S. peregrina* through the lower sequence indicates temperate oceanographic conditions, and its terminal event indicates a retirement of temperate conditions from the Walvis Basin region. Simultaneously, an Antarctic species, *C. pliocenica*, first appeared in Sample 24X-CC; it ranges up to Sample 14H-CC, indicating invasion of cooler waters into the study region from a southern higher latitude, which agrees with diatom observations (see below).

### Diatoms

Diatom counts and identification were carried out on smear slides and on acid-treated, sieved (63 µm) material from core-catcher samples from Hole 1081A. Additional samples from within the cores were examined close to datum events to improve the stratigraphic resolution and to refine floral changes (Table 6). Diatom preservation is moderate throughout Hole 1081A. The record of diatom abundance points to a substantial increase in deposition during the late Pliocene and early Pleistocene (from ~227 to 50 mbsf), reaching a maximum in the late Pliocene, followed by a decrease within the Pleistocene at about 1 Ma (~77 mbsf; see Table 6; Fig. 21). Overall abundance levels remain low (trace–frequent) in the late Miocene and early Pliocene. This pattern resembles that of DSDP Site 532 (see summary in Hay and Brock, 1992; Berger and Wefer, 1996). We may assume that the diatom content at Hole 1081A reflects a varying nutrient supply that could be related to the upwelling of nutrient-rich deeper waters and high biological productivity over the Walvis Ridge, especially in the late Pliocene.

The diatom biostratigraphic zones used for this hole are those summarized in Barron (1985). Zones could not be applied to Samples 175-1081A-26X-CC through the end of the hole because of the scarcity of diatom valves and concomitant lack of biostratigraphic markers (Table 6). The LO (1.55 Ma) of *Rhizosolenia praebergonii* var. *robusta* was recognized between Samples 175-1081A-11H-CC and 12H-1, 90 cm; the LO (0.8 Ma) of the silicoflagellate *Bachmannocena quadrangula* was recognized between Samples 175-1081A-5H-CC and 6H-CC (Fig. 20).

The diatom assemblage consists of a mixture of upwelling-indicator (*Chaetoceros* resting spores and *Thalassionema nitzschioides* var. *nitzschioides*) and oceanic species (e.g., *Azpeitia* spp., *Hemidiscus cuneiformis*, and *Thalassiothrix* spp.). Within Subunit IB, upwelling-related species dominate the diatom assemblage during highest abundance times in the late Pliocene (see “Lithostratigraphy” section, this chapter). They are not common in early Pliocene nor Miocene sediments when oceanic species tend to dominate (Table 6). In addition, the record of two middle- to high-latitude species, *Proboscia* (=Simon-

**Table 6. Overall diatom abundance estimated from smear slides and strewn slides of the >63-µm fraction from Hole 1081A.**

Core, section, interval (cm)	Depth (mbsf)	Overall abundance (smear slide)	Overall abundance (sieved 63 µm)	Dominant assemblage	Diatom stratigraphic zones
175-1081A-1H-1, 50	0.50	0.0	1.0		NTD17?
1H-CC	0.89	2.0			
2H-1, 62	1.62	1.0	1.0	Upwelling	
2H-1, 100	2.00	1.0			
2H-4, 37	5.87	2.0			
2H-CC	8.22	3.0			
3H-1, 62	11.12	0.0	0.0		
3H-2, 64	12.64	1.0			
3H-4, 80	15.70	2.0	0.0		
3H-6, 70	18.60	1.0			
3H-CC	20.05	1.0	0.0		
4H-1, 63	20.63	1.0			
4H-3, 80	23.80	1.0	0.0		
4H-4, 70	25.10	1.0			
4H-6, 70	28.10	1.0	0.0		
4H-CC	29.93	0.0			
5H-1-74	30.24	0.0	1.0		
5H-3, 84	33.34	0.0			
5H-7, 30	38.70	2.0	1.0		
5H-CC	39.12	2.0			
6H-1, 130	40.30	1.0	4.0	Upwelling	[ <i>S. curvirostris</i> ]
6H-3, 80	42.80	2.0			
6H-4, 120	44.60	2.0	2.0	Upw. + oceanic	NTD 16
6H-6, 80	47.20	2.5			
6H-CC	48.52	4.0	2.0	Upwelling	
7H-1, 70	49.20	3.0			
7H-2, 65	50.65	4.5	3.5	Upw. + oceanic	
7H-3, 40	51.90	3.5			
7H-6, 80	56.70	3.5	2.5	Upwelling	
7H-CC	58.03	2.5			
8H-2, 60	60.10	4.5	2.0	Upwelling	
8H-5, 80	64.70	3.0			
8H-6, 134	66.74	2.5	3.0	Upw. + oceanic	
8H-CC	67.71	3.0			
9H-2, 80	69.80	2.0	2.5	Upwelling	
9H-4, 80	72.70	2.5			
9H-6, 134	76.24	3.0	2.5	Upwelling	
9H-CC	76.72	4.5			
10H-1, 30	77.30	4.0	2.0	Upw. + oceanic	
10H-4, 70	82.10	2.0			
10H-6, 100	85.40	3.0	2.5	Upwelling	
10H-CC	86.31	4.0			
11H-1, 133	87.83	2.0	2.5	Upwelling	
11H-4, 70	90.20	3.0			
11H-5, 70	93.10	4.0	3.5	Upw. + oceanic	
11H-CC	96.12	4.0			
12H-1, 90	96.90	3.5	2.0	Upw. + oceanic	
12H-4, 64	101.04	2.0			
12H-5, 100	102.90	4.0	3.0	Upwelling	
12H-6, 30	103.70	2.0			
12H-CC	105.05	3.0	5.0	Upw. + oceanic	
13H-1, 70	106.20	4.0			
13H-4, 70	110.70	4.0	3.0	Upw. + oceanic	
13H-5, 140	112.90	3.0			
13H-CC	114.87	3.5	3.0	Upw. + oceanic	
14H-2, 80	117.30	3.5			
14H-4, 62	120.12	5.0	3.0	Upw. + neritic + oceanic	
14H-5, 62	121.62	4.0			
14H-6, 62	123.12	4.5	3.0	Upw. + oceanic	
14H-CC	124.50	5.0			
15H-1, 90	125.40	4.5	3.0	Upw. + oceanic	
15H-3, 80	128.30	4.5			
15H-6, 90	132.96	4.5	5.0	Upw. + oceanic	
15H-7, 80	134.36	4.0			
15H-CC	134.77	3.0	5.0	Upw. + oceanic	
16H-CC	142.51	4.0			
17X-1, 11	137.11	1.0	5.0	Upw. + oceanic	
17X-1, 130	138.30	2.0			
17X-3, 79	140.75	4.0	5.0	Upw. + oceanic	
17X-3, 117	141.13	4.0			
17X-5, 30	143.26	5.0	5.0	Upw. + oceanic	
17X-5, 104	144.00	5.0			
17X-5, 112	144.08	4.5	5.0	Upw. + oceanic	
17X-CC	144.45	5.0			

Table 6 (continued).

Core, section, interval (cm)	Depth (mbsf)	Overall abundance (smear slide)	Overall abundance (sieved 63 µm)	Dominant assemblage	Diatom stratigraphic zones	Core, section, interval (cm)	Depth (mbsf)	Overall abundance (smear slide)	Overall abundance (sieved 63 µm)	Dominant assemblage	Diatom stratigraphic zones
18H-1, 93	146.93	4.0				33X-4, 24	294.04	3.5			
18H-3, 84	149.84	3.5				33X-CC	298.07	3.0	4.0	Upw. + oceanic	
18H-4, 50	150.95	4.0				34X-2, 82	301.32	3.0			
18H-4, 100	151.45	4.0				34X-CC	302.14	1.0	1.0		
18H-CC	154.49	3.0	3.0	Upw. + oceanic		35X-1, 80	309.40	1.0			
19X-2, 120	157.20	4.5				35X-2, 120	311.30	1.0			
19X-5, 35	160.85	4.5				35X-CC	312.00	1.0	1.0		
19X-CC	164.17	5.0	5.0	Upw. + oceanic		36X-2, 135	320.00	2.0			
20X-3, 125	168.35	4.5				36X-4, 45	322.10	1.5			
20X-4, 25	168.85	5.0				36X-5, 80	323.95	1.5			
20X-CC	172.90	5.0	5.0	Upw. + neritic + oceanic	NTD 15	36X-CC	327.14	1.0	1.0		
21X-2, 70	176.00	3.0				37X-2, 100	330.30	2.5			
21X-5, 40	179.63	5.0				37X-5, 100	334.80	1.0			
21X-CC	182.38	4.0	2.0	Upw. + oceanic		37X-CC	336.05	1.0	1.0		
22X-2, 70	185.70	3.5				38X-1, 80	338.30	0.0			
22X-3, 40	186.90	4.0				38X-CC	341.81	0.0	1.0		
22X-7, 20	192.70	3.0				39X-1, 68	347.78	0.0			
22X-CC	193.36	1.0	1.0			39X-4, 60	351.52	0.0			
23X-1, 90	194.00	1.0				39X-CC	356.68	0.0	1.0		
23X-5, 85	199.95	3.0				40X-1, 29	357.09	0.0			
23X-CC	201.81	5.0	5.0	Upw. + oceanic	[ <i>S. barboi</i> ]	40X-CC	357.95	0.0	0.0		
24X-1, 70	203.50	3.5				41X-1, 56	366.96	1.0			
24X-4, 127	208.57	3.0				41X-3, 73	370.13	1.0			
24X-CC	209.29	4.0	3.0	Upw. + oceanic		41X-CC	375.23	1.0	2.0		
25X-2, 119	215.03	2.0				42X-1, 63	376.63	1.0			
25X-4, 127	218.17	1.5				42X-5, 76	382.76	1.5			
25X-4, 143	218.33	1.0				42X-CC	385.77	0.0	1.0		
25X-CC	219.80	2.0	5.0	Oceanic Upw. + oceanic	↓	43X-1, 69	386.29	1.0			
26X-2, 70	224.20	4.0				43X-5, 76	392.36	0.0			
26X-4, 112	227.62	1.0				43X-CC	394.91	1.0	1.0		
26X-CC	228.28	1.0	1.0			44X-2, 35	397.15	2.0			
27X-2, 47	233.47	1.0				44X-CC	397.79	0.0	1.0		
27X-4, 112	237.12	1.0				45X-1, 45	405.35	4.0		Oceanic	
27X-5, 76	238.26	0.0				45X-4, 78	410.18	3.5		Oceanic	
27X-CC	240.33	1.0				45X-6, 106	413.46	3.5			
28X-5, 61	247.83	1.0				45X-CC	414.69	1.0	1.0		
28X-CC	249.87	2.0	4.0	Oceanic	No zones assigned	46X-1, 93	415.53	1.0			
29X-2, 95	253.25	3.0				46X-4, 60	419.70	2.0			
29X-3, 141	255.21	1.0				46X-CC	424.31	1.0	1.0		
29X-CC	258.72	0.0	1.0			47X-2, 75	426.45	1.0			
30X-3, 38	263.78	0.0				47X-6, 77	432.54	1.5			
30X-5, 55	266.95	0.0				47X-CC	433.70	1.0	3.0	Oceanic	
30X-CC	267.52	0.0	0.0			48X-1, 52	434.32	3.0			
31X-1, 138	271.48	1.0				48X-CC	443.49	0.0	0.0		
31X-3, 30	273.40	0.0				49X-2, 70	445.70	1.0	1.0		
31X-CC	273.88	1.0	1.0			49X-CC	448.38	0.0	0.0		
32X-1, 69	280.39	1.0									
32X-4, 48	284.68	1.0									
32X-4, 86	285.06	1.5									
32X-CC	289.32	3.0	4.0	Upw. + oceanic							
33X-1, 60	289.90	2.0									
33X-2, 135	292.15	3.0									

Notes: Overall abundance is given as 0 = barren; 1 = trace; 2 = rare; 3 = few; 4 = common; and 5 = abundant. The dominant assemblage in each core catcher and the characteristic diatom stratigraphic zone are given. Note the occurrence of *Simonse-niella curvirostris* in Sample 175-1081A-7H-1, 70 cm, and of *S. barboi* in Samples 13H-1, 70 cm, to 23X-5, 85 cm (see text).

*seniella curvirostris* in Sample 175-1081A-7H-1, 70 cm (at approximately the Brunhes/Matuyama boundary), and *P. barboi* in Samples 175-1081A-13H-1, 70 cm, to 23X-5, 85 cm (~1.8–2.8 Ma), is interesting to note. *P. barboi* is a known ancestor of the Pleistocene cold-water diatom *P. curvirostris*, and it appears to have had similar ecological preference (Fenner, 1991; Barron, 1995). The occurrence of these species may indicate periods of intensified Benguela Current transport, an assumption that is also supported by the co-occurrence of the Antarctic radiolarian *C. pliocenica* (see above).

## PALEOMAGNETISM

The investigation of magnetic properties at Site 1081 included the measurement of bulk susceptibility of whole-core sections and the

natural remanent magnetization (NRM) of archive-half sections. The Tensor tool was used to orient Cores 175-1081A-4H through 16H and 18H, Cores 175-1081B-4H through 21H, and Cores 175-1081C-3H through 17H (Table 7).

## Natural Remanent Magnetization and Magnetic Susceptibility

Measurements of NRM were made on all archive-half core sections from Holes 1081A, 1081B, and 1081C. Sections from Hole 1081A were demagnetized by AF at 10 and 20 mT, and sections from Holes 1081B and 1081C were demagnetized by AF at 20 mT only. Magnetic susceptibility measurements were made on whole cores from both holes as part of the MST analysis (see “Physical Properties” section, this chapter).

**Table 7. Tensor tool-orientation data for cores from Holes 1081A, 1081B, and 1081C.**

Core	MTF (°)	Inclination angle
175-1081A-		
4H	354	0.63
5H	313	0.61
6H	77	0.53
7H	64	1.78
8H	147	0.68
9H	133	0.74
10H	70	0.67
11H	337	0.58
12H	241	0.93
13H	237	0.73
14H	188	0.90
15H	127	0.75
16H	256	0.64
18H	76	0.89
175-1081B-		
4H	64	0.21
5H	101	0.21
6H	76	0.25
7H	185	0.43
8H	175	0.42
9H	327	0.52
10H	279	0.47
11H	204	0.42
12H	147	0.38
13H	49	0.19
14H	123	0.23
15H	36	0.15
16H	310	0.29
17H	67	0.23
18H	248	0.63
19H	150	0.18
20H	166	0.22
21H	85	0.25
175-1081C-		
3H	95	0.37
4H	21	0.40
5H	210	0.28
6H	31	0.12
7H	267	0.08
8H	351	0.39
9H	159	0.30
10H	73	0.45
11H	1.18	0.72
12H	92	0.81
13H	328	0.90
14H	138	0.87
15H	70	0.89
16H	265	0.76
17H	43	1.08

Notes: The orientation parameter (MTF) is the angle in degrees between magnetic north and the double line marked on the center of the working half of the core. The local declination anomaly is 14°W.

The intensity of NRM after 20-mT demagnetization decays gradually with depth from  $\sim 10^{-2}$  to  $\sim 10^{-5}$  A/m in the upper 150 mbsf (Figs. 23, 24). It rapidly increases with depth to  $10^{-2}$  A/m between 160 and 190 mbsf at Hole 1081A, then decreases gradually with depth again. The trend in magnetic susceptibility is similar to the remanent intensity, except for the uppermost 30 mbsf and between 210 and 260 mbsf, but the amplitude of the variations is much smaller, ranging between 3 and  $15 \times 10^{-5}$  (SI volume units).

A primary NRM record was recovered after 20-mT demagnetization from sediments in the upper 120 mbsf (Figs. 23, 24). APC cores, however, below 120 mbsf from all three holes and all XCB cores from Hole 1081A (between 137 and 144 mbsf and below 154 mbsf) were pervasively overprinted during coring. Declinations of APC cores below  $\sim 120$  mbsf show a weak grouping at  $0^\circ$  before orientation (Fig. 23), indicating significant coring-induced magnetization of a radially-inward direction (see “Paleomagnetism” section, “Site 1077” chapter, this volume). All XCB cores show declinations of about  $-30^\circ$  and inclinations of  $\sim 45^\circ$ , even where sediments are extensively biscuitied (Fig. 23). The pervasiveness of the declination, which is independent of the orientation of sediments, indicates that the magnetization was acquired during coring, but it is difficult to explain the nonaxisymmetric geometry. A magnetic overprint similar to that found at this site was observed in XCB cores during previous ODP legs (declination of  $+20^\circ$ , Shipboard Scientific Party, 1996; declination of  $-40^\circ$ , Shipboard Scientific Party, in press).

### Magnetostratigraphy

We identified the polarity of the NRM from the magnetic declinations and inclinations. The Brunhes/Matuyama boundary (0.78 Ma; Berggren et al., 1995) occurs between 48 and 52 mbsf at Hole 1081A, between 51 and 53 mbsf at Hole 1081B, and between 53 and 57 mbsf at Hole 1081C (Fig. 24, middle and right panels). The termination and beginning of the Jaramillo Subchron (C1r.1n), 0.99 and 1.07 Ma (Berggren et al., 1995), respectively, occur at  $\sim 68$  and 72 mbsf at Hole 1081A, 68 and 75 mbsf at Hole 1081B, and 69 and 78 mbsf at Hole 1081C. The termination and beginning of the Olduvai Chron (C2n), 1.77 and 1.95 Ma (Berggren et al., 1995), respectively, occur at about 102 and 116 mbsf at Hole 1081A, 102 and 114 mbsf at Hole 1081B, and 97 and 112 mbsf at Hole 1081C.

No short reversal events and/or excursions were identified within the Brunhes and Matuyama Chrons. All anomalous directions in the Brunhes Chron were likely caused by disturbance of the sediments because they occur at core boundaries. The scatter of directions be-

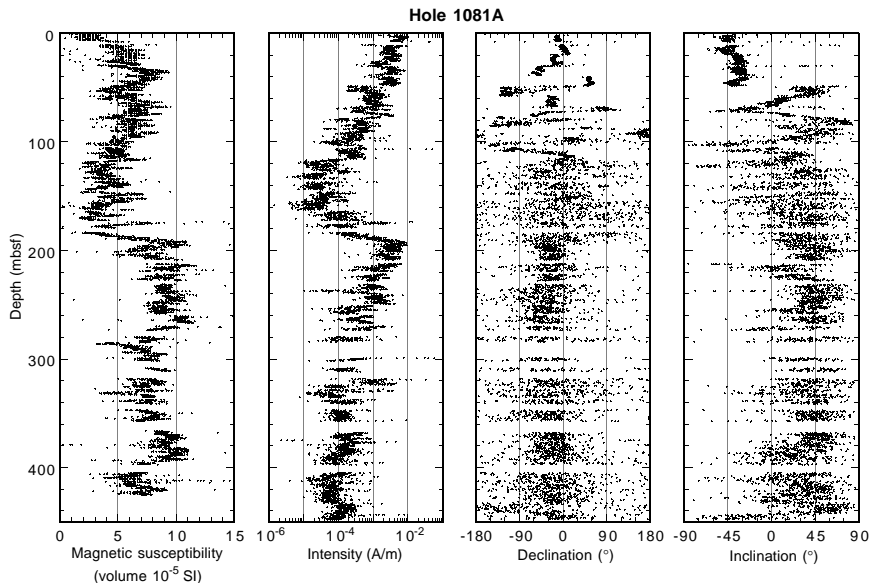


Figure 23. Magnetic susceptibility and NRM intensity, declination (unoriented), and inclination for Hole 1081A. See Figure 24 for oriented declination of APC cores (upper 150 mbsf).

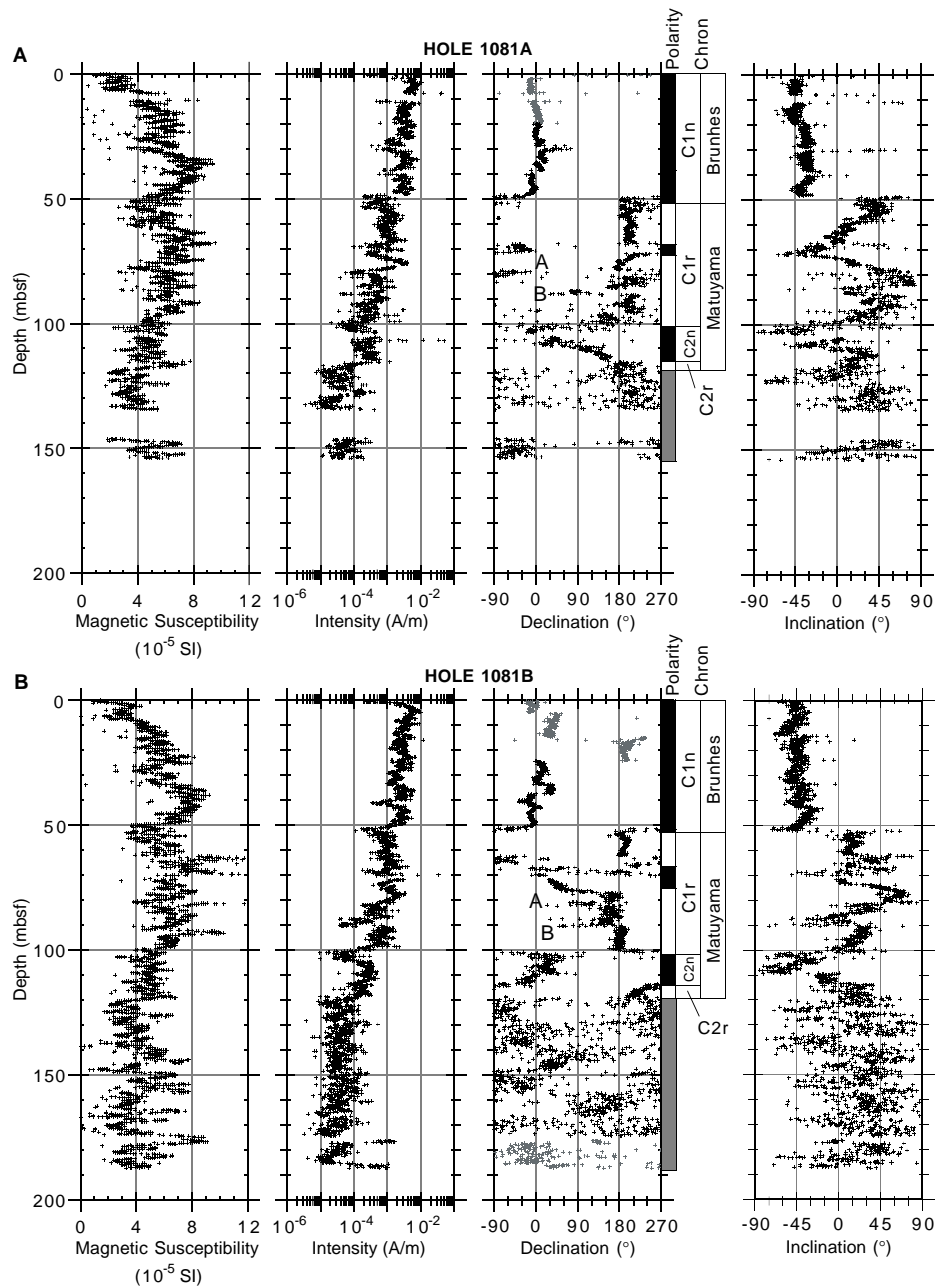


Figure 24. Magnetic susceptibility (SI), intensity, declination, magnetostratigraphic interpretation, and inclination after 20-mT demagnetization. Black symbols = Tensor corrected; gray symbols = uncorrected. Polarity shading: black = normal, white = reversed, and gray = ambiguous. **A.** Hole 1081A. **B.** Hole 1081B. (Continued next page.)

tween 62 and 70 mbsf at Hole 1081B (Core 175-1081B-8H) is also attributed to sediment disturbance. There are several apparent shifts in direction between the Jaramillo and Olduvai Subchrons (including those labeled “A” and “B” in Figure 24). They can be correlated among the three holes from the magnetic susceptibility. Most of them showed declinations close to zero before Tensor orientation, however, suggesting that these directions represent the radial-inward coring-induced magnetization. This was confirmed for Hole 1081C by measuring the NRM of both archive and working halves for the suspicious sections (175-1081C-9H-5, 10H-3, and 11H-3). The declinations at the pseudo-events were almost 180° opposite between the archive and working halves, indicating a radial-inward magnetization (Fig. 25). It is unclear why the overprint dominates at these particular horizons. The remanent intensity decreases at many of these pseudo-

events, suggesting that the primary component is much weaker and thus strongly overprinted.

### The Brunhes/Matuyama Polarity Transition

Sediments from the three holes recorded the Brunhes/Matuyama polarity transition with little magnetic overprint. These records show the characteristic behavior of the Brunhes/Matuyama transition, displayed in Figure 26. Before the main transition between 52.5 and 52.0 mbsf, a decrease in intensity, accompanied by a fluctuation of directions, occurs at 54.2 mbsf. This may represent the “precursor” of the reversal (at ~15 k.y.) before the main transition documented by Hartl and Tauxe (1996). Shortly after the main transition, a large change in declination with a shallow inclination (“rebound”) occurs at 51.4

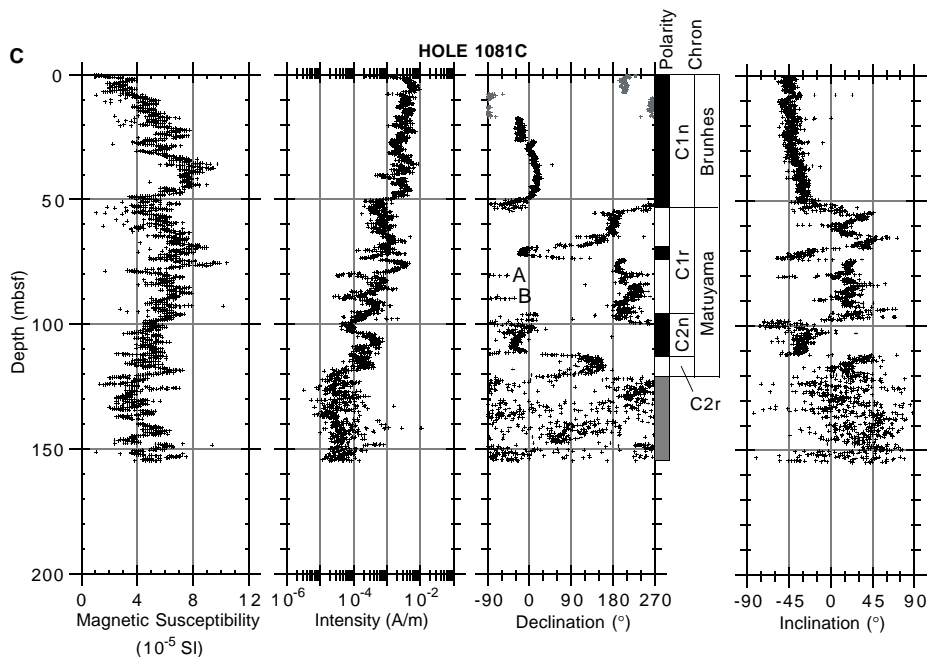


Figure 24 (continued). C. Hole 1081C.

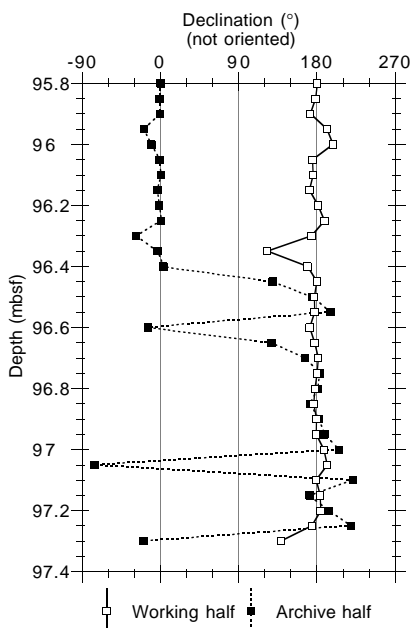


Figure 25. Unoriented declination of Section 175-1081C-11H-3. Declinations of 0° and 180° in the archive and working halves above 96.5 mbsf indicate a radial-inward magnetic overprint.

mbsf, which may correspond to the shift reported previously by Clement and Kent (1986) and Quidelleur and Valet (1996). Agreement with this previously reported feature of the Brunhes/Matuyama transition suggests that sediments at this site faithfully recorded the geomagnetic changes. These sediments will thus be useful for studying the detailed behavior of the geomagnetic field during the polarity reversal.

### COMPOSITE SECTION

At Site 1081, three holes were cored with a maximum penetration of 448.2 mbsf. The maximum depth reached with the APC was 187.4

mbsf (Hole 1081B). Physical properties and color reflectance data were measured at 2-cm (Hole 1081A) and 4-cm (Holes 1081B and 1081C) intervals. The correlation of features present in the physical and visual properties measurements of adjacent holes was used to demonstrate the completeness of the local stratigraphic sequence drilled and to establish a depth scale in terms of meters composite depth (mcd) for Site 1081 (Table 8). The continuity of the stratigraphic sequence was shown to a depth of 215 mcd (Fig. 27).

At Site 1081, magnetic susceptibility and wet bulk density (GRAPE) were used to establish the mcd scale. The data sets were extensively processed before being used for correlation. Suspect measurements were eliminated by thresholding the data. The resulting data were smoothed using a Gaussian filter with a length of 12 cm. All data shown in Figures 27 and 28 were processed as described above.

The resulting growth of the mcd scale compared with the standard ODP mbsf scale is ~7% (Section 175-1081A-23X-CC at 215 mcd and 201.5 mbsf). Figure 29 shows a linear growth of offsets applied to cores down to 130 mbsf. The growth of the mcd scale compared with the mbsf scale averages 10% in this depth interval. Below 130 mbsf, offsets are constant.

The gaps between successive cores of the same hole average ~2 m. Large intervals seem to be missing at Hole 1081A at 9.5 mcd (between Cores 175-1081A-2H and 3H, 4 m), 85.5 mcd (between Cores 175-1081A-14H and 15H, 2.5 m), 156.5 mcd (between Cores 175-1081A-16H and 18H, 2.5 m), and 192.5 mcd (between Cores 175-1081A-21X and 22X, 4.5 m).

Of special interest is the transition of APC cores to XCB cores from Hole 1081A and the correlation of XCB cores from Hole 1081A to adjacent APC cores from Hole 1081B. The quality of XCB cores from Hole 1081A compared with APC cores from Hole 1081B is good. Interhole correlation was possible for the entire APC-covered length at Hole 1081B, down to 215 mcd.

The spliced record presented in Figure 28 (also see Table 9) is continuous to 215 mcd for magnetic susceptibility and GRAPE wet bulk densities. The selection of cores to be included in the spliced record and the placement of tie points was carried out mainly using the composite section of magnetic susceptibility from Site 1081. The strategy for splicing was to construct a continuous spliced record with smooth transitions between individual cores for most of the triple APC-covered depth interval. Because of the disturbed Core 175-1081B-8H and a missing interval between Cores 175-1081B-9H and

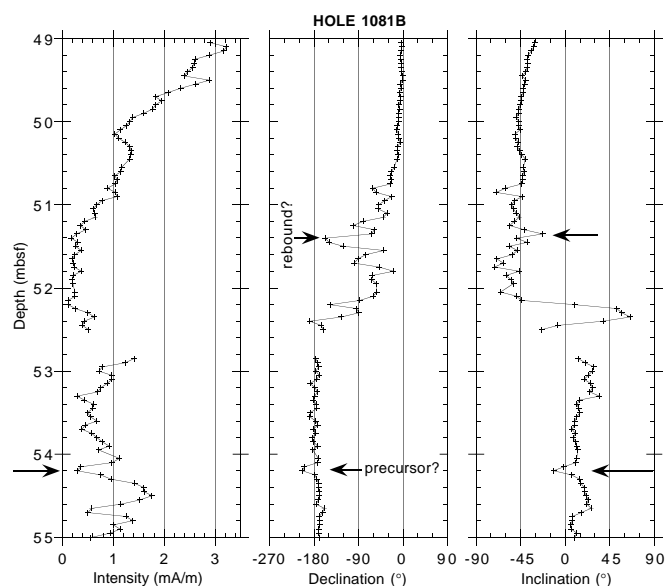


Figure 26. The Brunhes/Matuyama transition recorded at Hole 1081B. NRM intensity, declination (oriented), and inclination.

10H, critical depth intervals were Cores 175-1081A-8H through 10H and Cores 175-1081B-8H through 10H. Also, the APC-to-XCB transition from Core 175-1081A-16H through 19X was problematic. Both depth intervals could be covered by the corresponding cores from Hole 1081C, thus emphasizing the importance of triple coverage to achieve a complete sedimentary sequence at a site.

## INORGANIC GEOCHEMISTRY

Twenty-four interstitial water samples were gathered from Hole 1081A over a depth range from 2.4 to 441.2 mbsf, at a sampling frequency of one sample per core for the upper 100 mbsf and every third core to total depth (Table 10). Unlike the previous Leg 175 sites, the drilling at this hole targeted the deeper portions of the sequences, thereby enabling the interstitial water program to document an additional suite of chemical behaviors that was not evident at sites with less penetration. Throughout the sequence, interstitial water variations are observed that can be tied directly to the local stratigraphic lithologic unit, as well as the variations caused by the changes in organic matter concentration, as have been observed previously. In particular, the depositional and paleoceanographic conditions that result in the diatom-rich clays of lithostratigraphic Subunit IB appear to have a strong influence on chemical processes occurring at Site 1081.

### Alkalinity, Sulfate, and Ammonium

Downcore profiles of alkalinity, sulfate, and ammonium (Fig. 30) through the upper ~100 mbsf record the degradation of organic matter found in these shallowly buried sediments. Sulfate is completely consumed within the upper 60 mbsf. Through this uppermost depth interval, alkalinity values increase sharply, and the concentration of ammonium also shows the greatest relative increase. These alkalinity values are lower than those measured at previous Leg 175 sites.

Additional chemical sources and sinks are active in the deeper portions of the hole. Below a minimum in alkalinity at 100 mbsf (see discussion of carbonate reactions below), values gently increase to a maximum of 30 mM at ~200 mbsf. Alkalinity then decreases steadily to a deep minimum value of 14.8 mM at the bottom of the hole. We interpret the maximum at 200 mbsf as reflecting a higher organic supply during the times in which lithostratigraphic Subunits IB and IC were deposited.

Table 8. Offsets applied to cores from Holes 1081A, 1081B, and 1081C.

Core	Depth (mbsf)	Offset (m)	Composite depth (mcd)
175-1081A-			
1H	0.0	0.00	0.00
2H	1.0	1.41	2.41
3H	10.5	2.80	13.30
4H	20.0	4.57	24.57
5H	29.5	5.27	34.77
6H	39.0	5.57	44.57
7H	48.5	6.95	55.45
8H	58.0	6.87	64.87
9H	67.5	7.99	75.49
10H	77.0	9.97	86.97
11H	86.5	8.86	95.36
12H	96.0	9.48	105.48
13H	105.5	11.64	117.14
14H	115.0	12.50	127.50
15H	124.5	12.54	137.04
16H	134.0	12.54	146.54
17X	137.0	12.54	149.54
18H	146.0	13.04	159.04
19X	154.5	13.08	167.58
20X	164.1	13.08	177.18
21X	173.8	13.08	186.88
22X	183.5	13.08	196.58
23X	193.1	13.08	206.18
24X	202.8	12.54	215.34
25X	212.4	12.54	224.94
26X	222.0	12.54	234.54
27X	231.5	12.54	244.04
28X	241.2	12.54	253.74
29X	250.8	12.54	263.34
30X	260.4	12.54	272.94
31X	270.1	12.54	282.64
32X	279.7	12.54	292.24
33X	289.3	12.54	301.84
34X	299.0	12.54	311.54
35X	308.6	12.54	321.14
36X	318.2	12.54	330.74
37X	327.8	12.54	340.34
38X	337.5	12.54	350.04
39X	347.1	12.54	359.64
40X	356.8	12.54	369.34
41X	366.4	12.54	378.94
42X	376.0	12.54	388.54
43X	385.6	12.54	398.14
44X	395.3	12.54	407.84
45X	404.9	12.54	417.44
46X	414.6	12.54	427.14
47X	424.2	12.54	436.74
48X	433.8	12.54	446.34
49X	443.5	12.54	456.04
175-1081B-			
1H	0.0	0.00	0.00
2H	5.0	0.36	5.36
3H	14.5	1.38	15.88
4H	24.0	2.73	26.73
5H	33.5	3.63	37.13
6H	43.0	4.33	47.33
7H	52.5	5.07	57.57
8H	62.0	5.07	67.07
9H	71.5	6.43	77.93
10H	81.0	6.71	87.71
11H	90.5	7.51	98.01
12H	100.0	8.43	108.43
13H	109.5	9.72	119.22
14H	119.0	10.48	129.48

Through this same deeper interval, ammonium concentrations also reach maximum values before decreasing toward the bottom of the hole. Again, we interpret the maximum as reflecting a greater availability of organic matter through that portion of the sequence. The decrease toward the bottom of the hole may reflect cation exchange reactions during clay diagenesis.

### Calcium, Magnesium, and Strontium

Concentration profiles of  $\text{Ca}^{2+}$ ,  $\text{Mg}^{2+}$ , and  $\text{Sr}^{2+}$  reflect processes of carbonate dissolution and precipitation through the various shallow and deep portions of the sedimentary sequence at Site 1081 (Fig. 31). First, from the seafloor to ~50 mbsf, the interstitial water chemical distribution of these elements records carbonate precipitation, including dolomitization, accompanied by calcite dissolution. The evidence for calcite dissolution is not as unambiguous as at the previous Leg 175 sites; however, the net increase from dissolved  $\text{Sr}^{2+}$  values near that of modern seawater at the shallowest sample to values approach-

Table 8 (continued).

Core	Depth (mbsf)	Offset (m)	Composite depth (mcd)
15H	128.5	11.60	140.10
16H	138.0	11.60	149.60
17H	147.5	11.60	159.10
18H	157.0	11.60	168.60
19H	166.5	12.52	179.02
20H	176.0	12.52	188.52
21H	185.5	12.52	198.02
175-1081C-			
1H	0.0	0.12	0.12
2H	7.3	0.58	7.88
3H	16.8	2.62	19.42
4H	26.3	3.79	30.09
5H	35.8	4.29	40.09
6H	45.3	5.27	50.57
7H	54.8	6.17	60.97
8H	64.3	6.73	71.03
9H	73.8	7.87	81.67
10H	83.3	7.45	90.75
11H	92.8	8.29	101.09
12H	102.3	9.21	111.51
13H	111.8	10.38	122.18
14H	121.3	11.06	132.36
15H	130.8	11.82	142.62
16H	138.4	12.62	151.02
17H	147.9	12.50	160.40

Note: The offsets transform ODP standard depth values in meters below seafloor (mbsf) to meters composite depth (mcd).

ing 150  $\mu\text{M}$  at ~130 mbsf reflects the diagenetic release of  $\text{Sr}^{2+}$  by the dissolution of biogenic calcite. Superimposed on this increase is a localized minimum at ~50 mbsf, which indicates the local presence of a strong  $\text{Sr}^{2+}$  sink that is most likely diagenetic apatite.

Stoichiometrically, the decrease in  $\text{Mg}^{2+}$  concentrations through this portion of the stratigraphy (an 8-mM decrease from 2.4 to 43.3 mbsf) essentially exactly mimics the decrease in  $\text{Ca}^{2+}$  concentration, suggesting that the paired decrease in these elements represents their simultaneous incorporation into diagenetic dolomite. From 43 mbsf to the bottom of the hole,  $\text{Ca}^{2+}$  and  $\text{Sr}^{2+}$  concentrations increase, whereas those of  $\text{Mg}^{2+}$  decrease. We interpret these chemical gradients as recording the dissolution of biogenic calcite and the incorporation of  $\text{Mg}^{2+}$  into clay phases. The several local minima superimposed on the general increase with depth of dissolved calcite broadly correspond to the lithologic unit boundaries and reflect the contrasts between these units (see "Lithostratigraphy" section, this chapter). Additionally, although there are portions of the stratigraphic section in Subunits IB and IC that contain dolomite layers in them, the interstitial water chemistry clearly indicates that these are trapped layers not actively growing; the zone of currently active dolomitization appears to be confined to the upper ~100 mbsf. As sedimentation occurs, this zone of precipitation moves upward, leaving behind the relict layers.

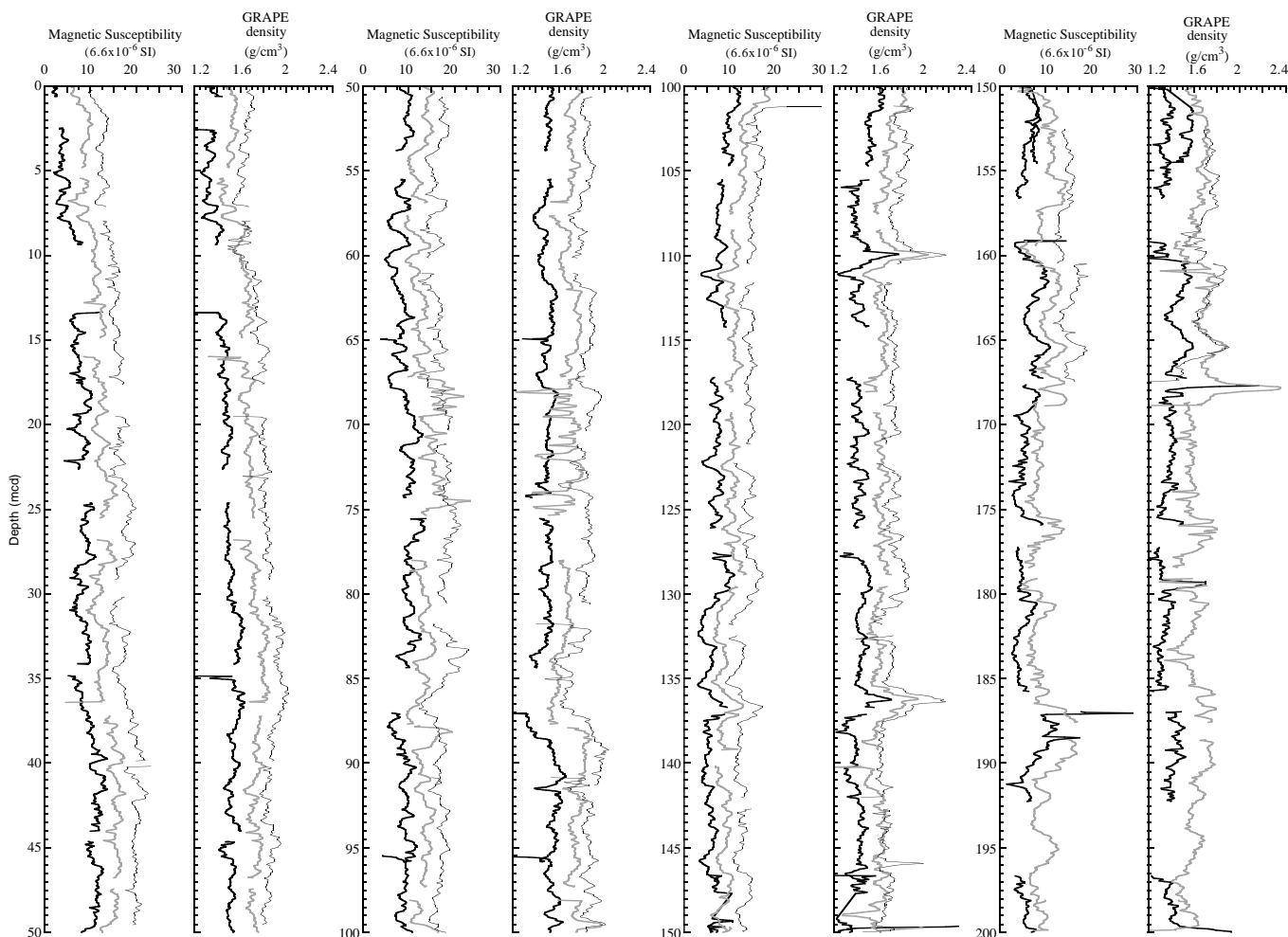


Figure 27. Composite section for Site 1081. Magnetic susceptibility and color reflectance (red/blue ratio [650 nm/450 nm]) are plotted for Holes 1081A (thick black line), 1081B (gray line), and 1081C (thin black line). The downhole logs are shown in meters composite depth (mcd). Offsets have been applied for clarity.

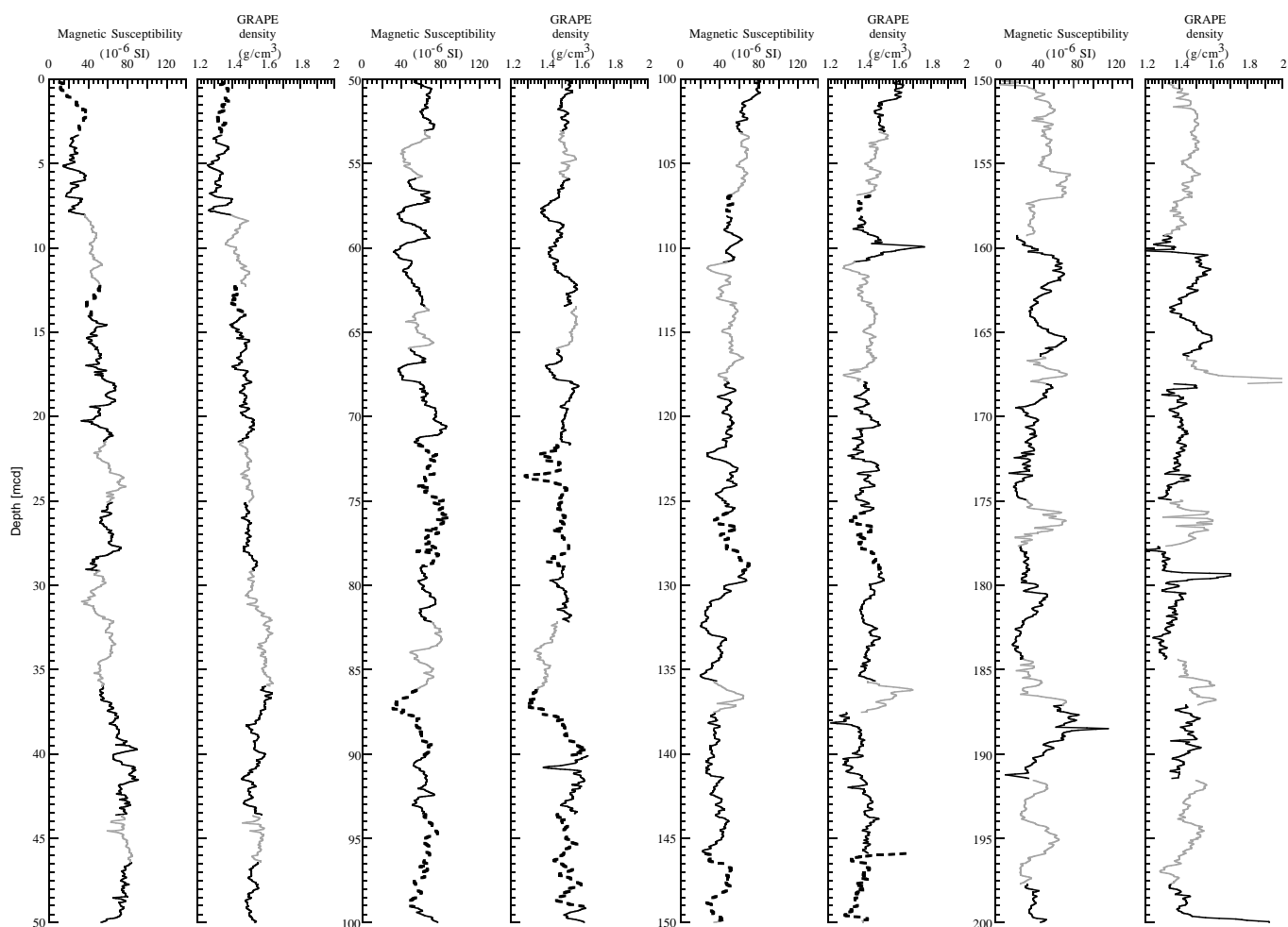


Figure 28. Spliced records for magnetic susceptibility and color reflectance (red/blue ratio [650/450 nm]) plotted in meters composite depth (mcd). Cores from Holes 1081A, 1081B, and 1081C have been used for the spliced record: black line = Hole 1081A, gray line = Hole 1081B, and dashed line = Hole 1081C.

### Silica and Phosphate

Dissolved silica increases in concentration very rapidly from representative bottom-water values to a maximum of 1074 mM at 100 mbsf (Fig. 32), recording the dissolution of biogenic opal. This maximum occurs within the diatom-rich clays of lithostratigraphic Subunit IB (see “Lithostratigraphy” section, this chapter), but its stratigraphic position does not appear to correspond to the first-order abundance index of diatom distributions (see “Biostratigraphy and Sedimentation Rates” section, this chapter). Because the maximum in dissolved silica occurs near the top of the diatomaceous unit, we interpret this chemical profile as recording first the diagenetic dissolution of biogenic opal in the youngest sediments of the subunit, followed by the formation of authigenic clays in the older sediments, which subsequently removes dissolved silica from the interstitial waters. In lithostratigraphic Subunit IC and Unit II, the local maxima in dissolved silica correspond well with local maxima in the diatom abundance index centered on ~300 and 410 mbsf (see “Biostratigraphy and Sedimentation Rates” section, this chapter).

Dissolved phosphate concentrations increase with depth within lithostratigraphic Subunit IA, recording the remineralization of organic matter. There is a pronounced local maximum centered at 150 mbsf in the middle of Subunit IB. The diatoms in this subunit are characteristic of upwelling species (see “Biostratigraphy and Sedi-

mentation Rates” section, this chapter). This is consistent with the high dissolved phosphate concentrations recording a greater supply of organic matter during the time in which the unit was deposited. Also, the highest TOC concentrations found at Site 1081 are distributed through this portion of the sequence. Dissolved phosphate concentrations decrease through Subunits IC and ID, recording the removal of phosphate most likely into either precipitating authigenic phases or onto iron oxides.

### Sodium and Potassium

The concentration of dissolved  $\text{Na}^+$  increases from seawater values to maximum values at depth (Fig. 33). This increase may be recording the release of  $\text{Na}^+$  from clay minerals. The concentration of  $\text{K}^+$  (Fig. 33) initially increases from seawater values in the uppermost 10 mbsf and remains essentially constant to a depth of ~300 mbsf. From 300 mbsf to the bottom of the hole, the concentration of dissolved  $\text{K}^+$  decreases by almost one-half. This decrease does not correspond with any lithologic boundary. Broadly, it is through a similar depth range that ammonium concentrations also decrease. Collectively, we interpret these concentration profiles as reflecting deep clay exchange reactions, but we cannot distinguish between purely diagenetic causes and those causes that may reflect a mineralogical or source variation.

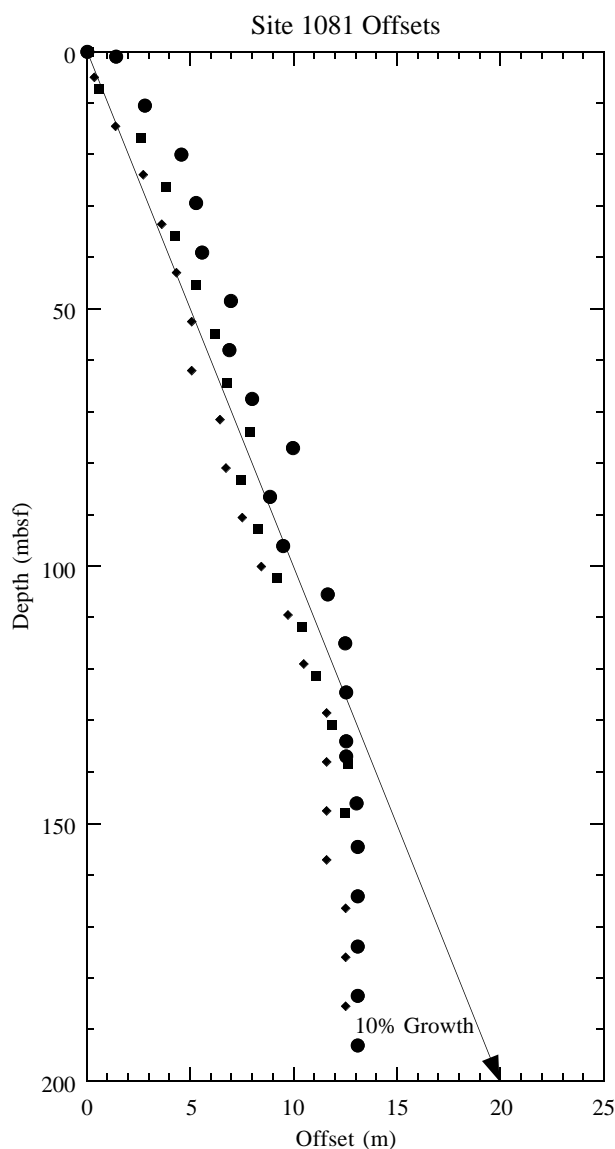


Figure 29. Core offsets applied to Site 1081 plotted against standard ODP meters below seafloor (mbsf). A linear 10% growth of meters composite depth (mcd) compared with mbsf is indicated by an arrow. Offsets are plotted for Hole 1081A (circles), Hole 1081B (diamonds), and Hole 1081C (squares).

### Salinity and Chloride

Salinity decreases smoothly downcore to a broad minimum from 90 to 178 mbsf before increasing with depth to the bottom of the hole (Fig. 34). The initial decrease most likely is recording the combined decreases of dissolved sulfate,  $\text{Ca}^{2+}$ , and  $\text{Mg}^{2+}$ , whereas the deep increase is responding to increases in  $\text{Na}^+$ ,  $\text{Cl}^-$ , and  $\text{Ca}^{2+}$ . Concentrations of dissolved  $\text{Cl}^-$  record a relative maximum at 72 mbsf and a continual increase to the bottom of the hole.

## ORGANIC GEOCHEMISTRY

Calcium carbonate and organic carbon concentrations were measured on sediment samples from Hole 1081A (Table 11). Organic matter atomic carbon/nitrogen (C/N) ratios and Rock-Eval pyrolysis

analyses were employed to determine the type of organic matter contained within the sediments. High gas contents were encountered, and routine monitoring of the sedimentary gases was done for drilling safety.

### Inorganic and Organic Carbon Concentrations

Concentrations of carbonate carbon in Site 1081 sediments range between 6.4 and 0.1 wt%, corresponding to 53.4 and 1.0 wt%  $\text{CaCO}_3$  (Table 11). The carbonate concentrations vary in two ways: (1) closely spaced changes related to light–dark color fluctuations and (2) a general downhole decrease followed by an increase in concentrations (Fig. 35). Sediments from this site are divided into an upper lithostratigraphic unit, which has three subunits, and a lower unit (see “Lithostratigraphy” section, this chapter). Subunit IA, a Pleistocene nannofossil- and foraminifer-rich clay, averages 31 wt%  $\text{CaCO}_3$ . Subunit IB is a Pliocene–Pleistocene diatom-rich clay that averages 8 wt%  $\text{CaCO}_3$ . Subunit IC is a Miocene–Pliocene nannofossil-rich clay that contains an average of 18 wt%  $\text{CaCO}_3$ . Unit II, a Miocene clayey nanofossil ooze, averages 30 wt%  $\text{CaCO}_3$ . The variations in concentrations reflect varying combinations of changes in delivery of calcareous material, dilution by noncalcareous components, and carbonate dissolution fueled by oxidation of organic matter.

TOC determinations were done regularly throughout Hole 1081A sediments to estimate the amounts of organic matter in the different lithostratigraphic units (Table 11). Like  $\text{CaCO}_3$  concentrations, TOC concentrations change in both short-term and longer term patterns (Fig. 36). Dark-colored sediments have higher TOC values than light-colored layers. TOC concentrations also differ in Hole 1081A lithostratigraphic units, averaging 5.00 wt% in Subunit IA, 5.21 wt% in Subunit IB, 3.34 wt% in Subunit IC, and 2.18 wt% in Unit II. The high TOC concentrations in all units are a consequence of the elevated paleoproductivity of the Benguela Current upwelling system, which has delivered abundant organic matter to the sediments, and the high accumulation rate of sediments (see “Biostratigraphy and Sedimentation Rates” section, this chapter), which enhances preservation of the organic matter.

### Organic Matter Source Characterization

Organic C/N ratios were calculated for sediment samples from the different Site 1081 lithostratigraphic units using TOC and total nitrogen concentrations (Table 11). The C/N ratios vary from 16.9 to 7.8 (Fig. 37). These C/N ratios are intermediate between unaltered algal organic matter (5–8) and fresh land-plant material (25–35; e.g., Emerson and Hedges, 1988; Meyers, 1994). The means of the C/N ratios are Subunit IA, 13.4; Subunit IB, 14.1; Subunit IC, 11.9; and Unit II, 10.3. Because of their setting under a major upwelling system and offshore from a coastal desert, it is likely that these organic carbon-rich sediments contain mostly marine-derived organic matter with only a minor contribution of detrital continental organic matter. The C/N ratios that are higher than fresh algal organic matter indicate that preferential loss of nitrogen-rich, proteinaceous matter and consequent elevation of C/N ratios occurred during settling of organic matter to the seafloor. Such early diagenetic alteration of C/N ratios is often seen under areas of elevated marine productivity such as upwelling systems (Meyers, 1997).

A Van Krevelen-type plot of the hydrogen index (HI) and oxygen index (OI) values indicates that the sediments contain type II (algal) organic matter (Fig. 38) that has been altered by microbial processing during early diagenesis. Well-preserved type II organic matter has high HI values (Peters, 1986); these values can be lowered by microbial oxidation (Meyers, 1997). In general, Hole 1081A sediments having lower Rock-Eval TOC values also have lower HI values (Fig. 39). This relationship confirms that the marine organic matter has been subject to partial oxidation, which simultaneously lowers TOC

**Table 9. List of splice tie points used to create the continuous “spliced” stratigraphic sequence for Site 1081.**

Hole, core, section, interval (cm)	Depth (mbsf)	Composite depth (mcd)	Whether tied	Hole, core, section, interval (cm)	Depth (mbsf)	Composite depth (mcd)	Offset (m)
1081C-1H-3, 20	3.20	3.32	Tie to	1081A-2H-1, 90.5	1.91	3.32	1.41
1081A-2H-4, 114	6.64	8.05	Tie to	1081B-2H-2, 118.5	7.69	8.05	0.36
1081B-2H-5, 88	11.88	12.24	Tie to	1081C-2H-3, 136	11.66	12.24	0.58
1081C-2H-5, 12	13.42	14.00	Tie to	1081A-3H-1, 70	11.20	14.00	2.80
1081A-3H-6, 78	18.68	21.48	Tie to	1081B-3H-4, 109	20.10	21.48	1.38
1081B-3H-7, 20	23.70	25.08	Tie to	1081A-4H-1, 50.5	20.51	25.08	4.57
1081A-4H-4, 16	24.56	29.13	Tie to	1081B-4H-2, 89	26.40	29.13	2.73
1081B-4H-7, 24	33.24	35.97	Tie to	1081A-5H-1, 120	30.70	35.97	5.27
1081A-5H-6, 144	38.34	43.61	Tie to	1081B-5H-5, 48	39.98	43.61	3.63
1081B-5H-7, 28	42.78	46.41	Tie to	1081A-6H-2, 34	40.84	46.41	5.57
1081A-6H-6, 108	47.48	53.05	Tie to	1081B-6H-4, 121	48.72	53.05	4.33
1081B-6H-6, 104	51.54	55.87	Tie to	1081A-7H-1, 42	48.92	55.87	6.95
1081A-7H-6, 62	56.52	63.47	Tie to	1081B-7H-4, 140	58.40	63.47	5.07
1081B-7H-6, 92	60.92	65.99	Tie to	1081A-8H-1, 112	59.12	65.99	6.87
1081A-8H-5, 92	64.82	71.69	Tie to	1081C-8H-1, 65	64.96	71.69	6.73
1081C-8H-6, 32	72.12	78.85	Tie to	1081A-9H-3, 36	70.86	78.85	7.99
1081A-9H-5, 78	74.18	82.17	Tie to	1081B-9H-3, 132	75.82	82.17	6.35
1081B-9H-6, 84	79.84	86.19	Tie to	1081C-9H-3, 100	77.80	86.19	8.39
1081C-9H-6, 40	81.70	90.09	Tie to	1081A-10H-3, 82	80.82	90.09	9.27
1081A-10H-5, 136	84.26	93.53	Tie to	1081C-10H-3, 16	86.46	93.53	7.07
1081C-10H-6, 120	92.00	99.07	Tie to	1081A-11H-3, 96	90.46	99.07	8.61
1081A-11H-6, 64	94.54	103.15	Tie to	1081B-11H-4, 72	95.72	103.15	7.43
1081B-11H-6, 144	99.44	106.87	Tie to	1081C-11H-4, 128	98.58	106.87	8.29
1081C-11H-5, 100	99.80	108.09	Tie to	1081A-12H-2, 110.5	98.61	108.09	9.48
1081A-12H-4, 96	101.36	110.84	Tie to	1081B-12H-2, 90.5	102.41	110.84	8.43
1081B-12H-7, 48	109.48	117.91	Tie to	1081A-13H-1, 75.5	106.27	117.91	11.64
1081A-13H-6, 100	114.05	125.69	Tie to	1081C-13H-3, 50.5	115.31	125.69	10.38
1081C-13H-5, 100	118.80	129.18	Tie to	1081A-14H-2, 17	116.68	129.18	12.50
1081A-14H-6, 68	123.18	135.68	Tie to	1081B-14H-5, 20	125.20	135.68	10.48
1081B-14H-6, 56	127.06	137.54	Tie to	1081A-15H-1, 49	125.00	137.54	12.54
1081A-15H-6, 128	133.34	145.88	Tie to	1081C-15H-3, 25	134.06	145.88	11.82
1081C-15H-5, 124	138.04	149.86	Tie to	1081B-16H-1, 25	138.26	149.86	11.60
1081B-16H-7, 60	147.67	159.27	Tie to	1081A-18H-1, 22.5	146.23	159.27	13.04
1081A-18H-5, 144	153.39	166.43	Tie to	1081B-17H-5, 131.5	154.83	166.43	11.60
1081B-17H-6, 144	156.44	168.04	Tie to	1081A-19X-1, 45	154.96	168.04	13.08
1081A-19X-5, 136	161.86	174.94	Tie to	1081B-18H-5, 33	163.34	174.94	11.60
1081B-18H-7, 8	166.08	177.68	Tie to	1081A-20X-1, 49	164.60	177.68	13.08
1081A-20X-5, 120	171.30	184.38	Tie to	1081B-19H-4, 85	171.86	184.38	12.52
1081B-19H-6, 56	174.56	187.08	Tie to	1081A-21X-1, 20	174.00	187.08	13.08
1081A-21X-4, 8	178.38	191.46	Tie to	1081B-20H-2, 144	178.94	191.46	12.52
1081B-20H-7, 20	185.2	197.72	Tie to	1081A-22X-1, 113	184.64	197.72	13.08
1081A-22X-7, 44	192.94	206.02	Tie to	1081A-23X-1, 0	193.1	206.18	13.08
1081A-23X-6, 92	201.52	214.60					

Note: The tie points are listed in standard ODP meters below seafloor (mbsf) and meters composite depth (mcd).

**Table 10. Interstitial water composition for Hole 1081A.**

Core, section, interval (cm)	Depth (mbsf)	pH	Alkalinity (mM)	Salinity	Cl <sup>-</sup> (titr) (mM)	Cl <sup>-</sup> (IC) (mM)	SO <sub>4</sub> <sup>2-</sup> (mM)	Na <sup>+</sup> (mM)	Mg <sup>2+</sup> (mM)	Ca <sup>2+</sup> (mM)	K <sup>+</sup> (mM)	H <sub>2</sub> SiO <sub>4</sub> (μM)	NH <sub>4</sub> <sup>+</sup> (μM)	PO <sub>4</sub> <sup>3-</sup> (μM)	Sr <sup>2+</sup> (μM)
175-1081A-															
2H-1, 140-150	2.40	7.56	4.190	35.0	551	550	26.54	471	52.33	10.47	11.15	514	442	15.7	91
2H-3, 140-150	5.40	7.15	5.180	35.0	552	551	26.04	475	51.91	10.07	11.06	594	713	13.4	90
3H-2, 130-140	13.30	7.77	7.830	34.5	552	550	24.05	478	50.64	8.52	11.78	550	1,266	29.4	91
4H-3, 130-140	24.30	7.16	10.670	34.5	555	554	18.84	479	49.75	6.55	11.75	624	1,960	24.8	88
5H-3, 130-140	33.80	7.25	17.690	34.0	559	557	8.53	481	46.24	3.94	11.90	666	2,912	33.9	72
6H-3, 130-140	43.30	7.96	22.890	33.5	564	565	2.65	487	43.54	3.42	11.40	832	3,189	30.5	68
7H-3, 130-140	52.80	8.01	22.630	33.5	566	565	1.51	488	42.46	3.61	11.49	899	3,421	25.9	76
8H-2, 130-140	62.30	8.04	25.380	33.5	566	565	0.17	490	41.36	3.69	11.66	956	3,509	28.2	99
9H-2, 130-140	71.80	7.99	25.430	33.5	568	568	0.00	495	39.53	3.74	11.44	967	3,945	23.7	120
10H-4, 130-140	81.30	7.91	23.530	33.0	562	561	0.45	495	35.47	4.06	11.74	948	4,309	20.2	124
11H-3, 130-140	90.80	7.79	21.040	32.5	558	561	0.14	496	31.89	4.00	11.55	1038	5,095	13.4	130
12H-3, 130-140	100.30	6.56	18.200	32.5	557	555	0.00	496	30.32	3.25	11.99	1074	6,070	7.0	133
15H-3, 144-154	128.90	7.24	22.520	32.5	556	556	0.04	501	28.67	4.64	11.67	1033	8,049	20.2	153
18H-3, 135-145	150.40	7.19	27.140	32.5	559	558	0.00	509	27.84	4.99	11.75	984	9,126	25.9	164
21X-3, 140-150	178.20	7.12	27.730	32.5	557	556	0.46	508	27.89	5.27	11.40	944	10,042	23.0	177
24X-3, 140-150	207.20	7.25	30.380	33.0	558	556	0.11	513	26.62	5.23	12.00	898	11,323	9.0	192
27X-3, 130-140	235.80	7.21	28.770	33.0	558	561	0.00	515	25.39	4.88	11.42	815	11,279	7.0	210
30X-3, 135-150	264.80	7.39	27.070	33.0	561	562	0.10	516	25.09	5.57	11.14	586	11,556	3.0	222
33X-3, 135-150	293.70	6.91	25.140	33.5	568	569	0.06	524	23.31	5.51	11.40	920	10,784	3.0	234
36X-4, 135-150	323.00	7.16	25.940	33.5	573	573	0.00	529	23.50	6.80	10.21	1069	11,381	3.0	251
39X-4, 135-150	352.30	7.17	20.340	33.5	569	584	0.00	518	23.28	7.49	9.50	715	10,668	3.0	254
42X-3, 138-150	380.40	7.19	18.360	34.0	581	601	0.18	528	24.00	7.64	8.72	865	9,620	3.0	257
45X-3, 138-150	409.30	7.15	16.420	34.5	588	587	0.83	536	23.36	7.73	8.09	1032	9,882	3.0	268
48X-5, 135-150	441.20	7.17	14.830	34.5	593	596	0.54	536	24.27	8.84	6.77	984	8,835	2.0	277

Notes: Cl<sup>-</sup> (titr) = analyzed by titration and Cl<sup>-</sup> (IC) = analyzed by ion chromatography. Empty cell = not analyzed.

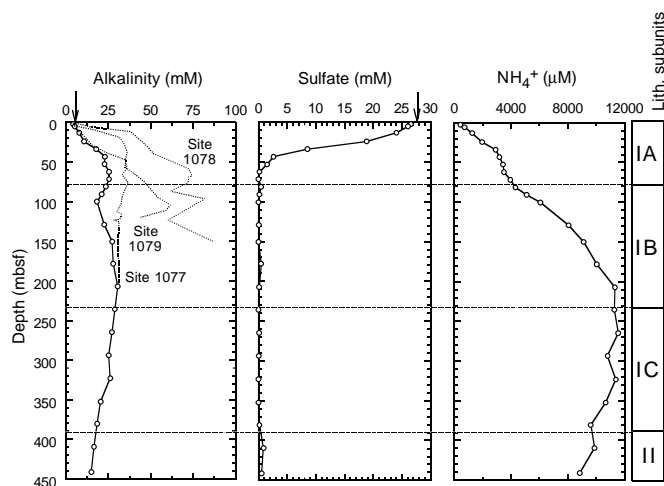


Figure 30. Downcore profiles of dissolved alkalinity, sulfate, and ammonium at Site 1081 (solid lines with open circles). Lithostratigraphic subunits shown on right-hand bar. Profiles of alkalinity at previous Leg 175 sites (dotted lines) are shown for comparison. Arrows = mean ocean-bottom-water values taken from Millero and Sohn (1992).

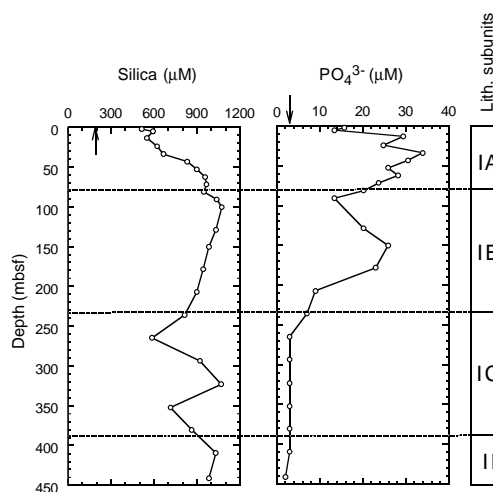


Figure 32. Downcore profiles of dissolved silica and phosphate at Site 1081. Lithostratigraphic subunits shown on right-hand bar. Arrows = mean ocean-bottom-water values taken from Millero and Sohn (1992).

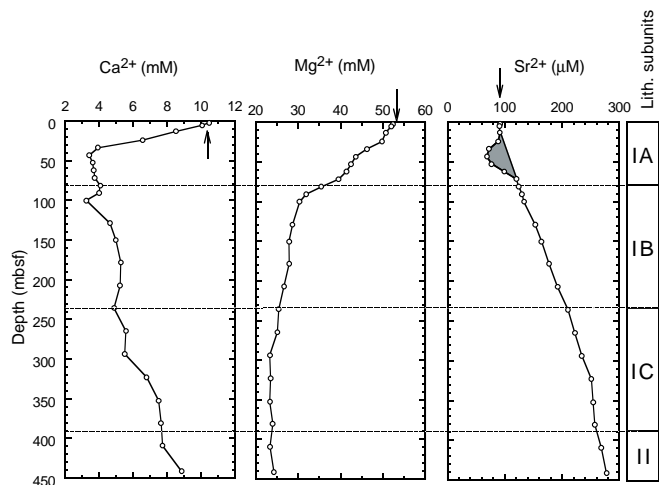


Figure 31. Downcore profiles of  $\text{Ca}^{2+}$ ,  $\text{Mg}^{2+}$ , and  $\text{Sr}^{2+}$  at Site 1081. Lithostratigraphic subunits shown on right-hand bar. Arrows = mean ocean-bottom-water values taken from Millero and Sohn (1992). Shaded region = position of local  $\text{Sr}^{2+}$  sink, superimposed over the general increase recording dissolution of biogenic calcite.

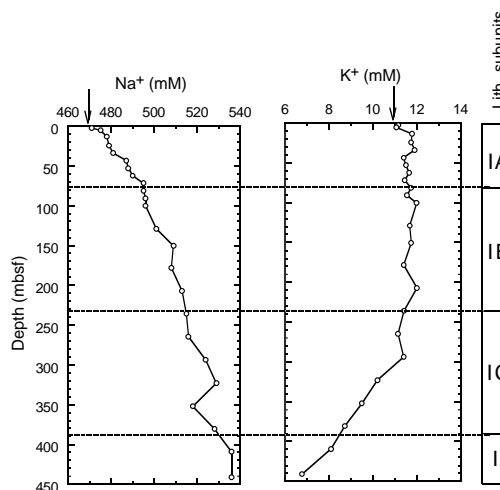


Figure 33. Downcore profiles of dissolved  $\text{Na}^{+}$  and  $\text{K}^{+}$  at Site 1081. Lithostratigraphic subunits shown on right-hand bar. Arrows = mean ocean-bottom-water values taken from Millero and Sohn (1992).

and HI values (Meyers, 1997). Further evidence of substantial amounts of in situ organic matter degradation exists in the large decreases in sulfate and increases in alkalinity and ammonia in the interstitial waters of Site 1081 sediments (see “Inorganic Geochemistry” section, this chapter).

The sediment samples have relatively low Rock-Eval  $T_{\text{max}}$  values (Table 12), showing that their organic matter is thermally immature with respect to petroleum generation (Peters, 1986) and therefore contains little detrital organic matter derived from the erosion of ancient sediments from Africa.

### Headspace Gases

Sediments from Site 1081 had high gas content, including  $\text{CO}_2$ , methane, and hydrogen sulfide. Total gas pressures became great enough in sediments below Core 175-1081A-3H (20 mbsf) to require perforating the core liner to relieve the pressure and prevent exces-

sive core expansion. The odor of hydrogen sulfide was noted in Cores 175-1081A-2H through 5H (1.5–37.9 mbsf), although this gas remained below the detection limits of shipboard instruments (~1 ppm).

Methane ( $\text{C}_1$ ) first appears in headspace gas samples from Hole 1081A sediments at 43.4 mbsf. Concentrations become significant in sediments below 60 mbsf (Fig. 40). High methane/ethane ( $\text{C}_1/\text{C}_2$ ) ratios and the absence of major contributions of higher molecular weight hydrocarbon gases (Table 13) indicate that the gas is biogenic, as opposed to thermogenic, in origin. The origin of the methane is probably from in situ microbial fermentation of the marine organic matter present in the sediments. Similar microbial production of methane from marine organic matter has been inferred from high biogenic gas concentrations in Pliocene–Pleistocene sediments from DSDP Site 532 nearby on the Walvis Ridge (Meyers and Brassell, 1985), Sites 897 and 898 on the Iberian Abyssal Plain (Meyers and Shaw, 1996), and also in middle Miocene sediments from Site 767 in the Celebes Sea (Shipboard Scientific Party, 1990). A biogenic origin of the methane is supported by the disappearance of interstitial sulfate at approximately the same sub-bottom depth where methane concen-

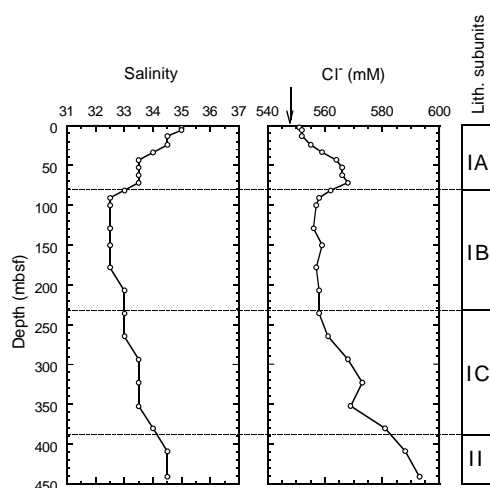


Figure 34. Downcore profiles of salinity and dissolved  $\text{Cl}^-$  at Site 1081. Lithostratigraphic subunits shown on right-hand bar. Arrow = mean ocean-bottom-water value taken from Millero and Sohn (1992).

trations begin to rise (see “Inorganic Geochemistry” section, this chapter), inasmuch as Claypool and Kvenvolden (1983) observe that the presence of interstitial sulfate inhibits microbial methanogenesis in marine sediments.

Natural gas analyses determined that the most abundant gas was usually  $\text{CO}_2$ , and headspace concentrations of this gas remain high to the bottom of Hole 1081A (446.5 mbsf; Fig. 41). Cragg et al. (1992) report the existence of viable microbes to depths of ~500 mbsf in the sediments of the Japan Sea. The abundance of biogenic gases in sediments from Site 1081 suggests the presence of viable microbial communities to similar sub-bottom depths on the Walvis Ridge.

## PHYSICAL PROPERTIES

Shipboard physical properties measurements included determination of compressional ( $P$ -wave) ultrasonic velocity, wet bulk density, magnetic susceptibility, and natural gamma radiation with the MST system on whole-round sections of cores from each hole (see “Explanatory Notes” chapter, this volume).

Index properties (gravimetric wet bulk density, porosity, and moisture content) were measured on one or two samples (volume = ~10  $\text{cm}^3$ ) per working-half section on all cores from Hole 1081A. Method C was used at this site (see “Explanatory Notes” chapter, this volume).

Discrete ultrasonic compressional ( $P$ -wave) velocity and undrained vane shear strength measurements were made at a resolution of about one or two sample points per section. For the discrete  $P$ -wave measurements, the modified Hamilton Frame was used to make ultrasonic measurements through the core liner.

Thermal conductivity was measured in every second section of each core at Hole 1081A.

### Multisensor Track

GRAPE density (Fig. 42),  $P$ -wave velocities (Fig. 43), and magnetic susceptibility (Fig. 44A) were determined every 4 cm, and natural gamma radiation was measured with a sampling period of 30 s at 32-cm resolution (Fig. 44B). MST data are included on CD-ROM (back pocket, this volume). Compressional velocities were recorded at a threshold of 100 incremental units to automatically exclude weaker signals from the profile. Deepest measurements with the MST  $P$ -wave logger were recorded at 80 mbsf, even before the discrete velocity measurements were terminated (Fig. 43). MST veloc-

ity and discrete velocities are not well correlated. An explanation cannot be given at this stage. At 70 mbsf, the MST profile merges with the discrete velocity profile.

Profiles of magnetic susceptibility and natural gamma radiation show a positive correlation throughout the entire depth range (Fig. 44A and B, respectively). GRAPE density values generally agree with the discrete wet bulk density data (Fig. 42), though GRAPE values are higher between 0 and 80 mbsf and lower or equal below 80 mbsf. Density core logs show a significant variability and a pronounced cyclicity in some intervals. Density anomalies (e.g., at 78 and 100 mbsf) coincide in many intervals with features observed in the logging and lithostratigraphic analysis (see “Downhole Logging” and “Lithostratigraphy” sections, this chapter). Natural gamma radiation shows a pronounced maximum at 240 mbsf. These features seem to correspond to dolomite horizons.

## Velocities

Discrete velocities range between 1535 and 1590 m/s, whereas  $P$ -wave logging with the MST shows lower values (Fig. 43). At 80 mbsf, a gradual increase of 50 m/s is observed over a depth range of 10 m. Below 25 mbsf, discrete velocity and the GRAPE density profiles correlate well.

## Index Properties

Results of discrete measurements of wet bulk density, porosity, and moisture content are presented in Figures 45A, 45B, and 45C, respectively (also see Table 14 on CD-ROM, back pocket, this volume). The density values vary between 1250 and 2200  $\text{kg}/\text{m}^3$ . Very sharp peaks are noticed at 122 and 220 mbsf.

Porosities decrease from 82% in the top section to 55% at 300 mbsf (Fig. 45B), and moisture content varies between 68% at the top of Hole 1081A and 30% at 300 mbsf (Fig. 45C).

## Thermal Conductivity and Geothermal Gradient

The thermal conductivity profile at Hole 1081A was measured in every second core section (see “Explanatory Notes” chapter, this volume). The profile shows a high degree of similarity with the magnetic susceptibility and natural gamma radiation profile (Fig. 44C), indicating major compositional changes.

In Hole 1081A, the Adara tool was deployed to measure formation temperature. A preliminary analysis provided four data points, which were used to estimate a geothermal gradient of 51°C/km, but further analyses will be required to confirm this result.

## Vane Shear Strength

An undrained vane-shear measurement was performed in the bottom part of each core section. The profile shows a gradual increase in vane shear from the top of Hole 1081A to 120 mbsf (Fig. 44D). As at previous sites, higher values of shear strength were found primarily in the middle sections of each core, as can be seen from the position of the indicated core breaks. Scatter increases below 70 mbsf. The change from APC to XCB drilling is apparent below 160 mbsf by a decrease of vane shear strength. Data quality below 155 mbsf is significantly affected by drilling disturbances and coring.

## DOWNHOLE LOGGING

Hole 1081A was logged with a full suite of sensors to continuously characterize the sedimentary changes, to correlate the lithostratigraphy with that at other sites, and to provide data for core-log integration (coring disturbance) and correlation with seismic profiles using synthetic seismograms.

**Table 11. Percentages of inorganic and total carbon, total nitrogen, and total sulfur in sediment samples from Hole 1081A.**

Core, section, interval (cm)	Depth (mbsf)	IC (wt%)	CaCO <sub>3</sub> (wt%)	TC (wt%)	TOC (wt%)	TN (wt%)	TS (wt%)	C/N (atomic)
175-1081A-								
Subunit IA - Pleistocene nannofossil- and foraminifer-rich clay								
1H-1, 47-48	0.47	6.41	53.4	10.46	4.05	0.46	0.45	10.2
2H-1, 46-47	1.46	4.85	40.4	10.02	5.17	0.54	1.17	11.1
2H-3, 46-47	4.46	3.88	32.3	11.74	7.86	0.71	1.99	12.9
2H-4, 46-47	5.96	4.98	41.5	10.06	5.08	0.48	1.44	12.4
3H-1, 46-47	10.96	4.36	36.3	9.77	5.41	0.49	1.64	13.0
3H-3, 46-47	13.86	4.31	35.9	8.75	4.44	0.40	1.55	13.0
3H-5, 46-47	16.86	3.85	32.0	10.02	6.17	0.49	1.53	14.6
4H-1, 46-47	20.46	3.13	26.1	9.15	6.02	0.51	1.98	13.8
4H-3, 46-47	23.46	3.53	29.4	8.71	5.18	0.43	1.47	13.9
4H-5, 46-47	26.36	5.38	44.8	9.25	3.88	0.35	1.18	12.8
5H-2, 46-47	31.46	5.34	44.5	8.40	3.06	0.30	1.29	12.1
5H-4, 46-47	34.36	3.14	26.2	9.44	6.29	0.55	2.16	13.5
5H-6, 46-47	37.36	2.11	17.6	9.22	7.10	0.55	2.15	15.0
6H-3, 46-47	42.46	2.27	18.9	7.64	5.38	0.44	2.09	14.2
6H-5, 46-47	45.36	2.93	24.4	7.77	4.84	0.40	1.98	14.0
7H-1, 46-47	48.96	3.75	31.3	7.67	3.91	0.33	1.84	13.8
7H-3, 46-47	51.96	2.54	21.2	7.78	5.24	0.41	1.68	15.0
7H-5, 46-47	54.86	4.50	37.5	8.14	3.64	0.33	1.58	13.0
8H-1, 46-47	58.46	3.88	32.3	8.34	4.46	0.35	1.59	14.9
8H-3, 46-47	61.46	3.64	30.3	6.53	2.89	0.28	1.80	12.3
8H-5, 46-47	64.36	2.68	22.3	7.08	4.40	0.38	1.95	13.6
9H-1, 46-47	67.96	2.34	19.5	8.88	6.53	0.50	2.42	15.2
9H-3, 46-47	70.96	2.04	17.0	6.68	4.64	0.39	2.04	13.7
9H-5, 46-47	73.86	2.94	24.5	7.35	4.40	0.36	1.95	14.2
Subunit IB - Pliocene-Pleistocene diatom-rich clay								
10H-1, 46-47	77.46	0.36	3.0	7.41	7.06	0.51	2.36	16.1
10H-3, 46-47	80.46	3.07	25.5	7.28	4.21	0.35	1.82	14.0
10H-4, 46-47	81.86	3.20	26.7	6.78	3.58	0.33	1.81	12.8
11H-1, 46-47	86.96	1.82	15.1	6.67	4.86	0.39	2.22	14.5
11H-3, 46-47	89.96	1.54	12.8	7.31	5.77	0.43	2.25	15.6
11H-5, 46-47	92.86	0.79	6.6	5.49	4.70	0.38	2.28	14.4
12H-1, 46-47	96.46	0.58	4.9	7.95	7.37	0.55	3.42	15.6
12H-3, 46-47	99.46	0.39	3.3	6.84	6.45	0.48	2.64	15.6
12H-5, 46-47	102.36	0.13	1.1	7.02	6.89	0.52	3.52	15.4
13H-1, 46-47	105.96	0.74	6.1	4.58	3.84	0.35	2.37	12.9
13H-3, 46-47	108.96	1.08	9.0	5.74	4.66	0.42	2.45	13.0
13H-5, 46-47	111.96	0.88	7.3	6.24	5.36	0.45	2.83	13.9
14H-1, 46-47	115.46	0.19	1.5	6.74	6.56	0.51	3.22	15.2
14H-3, 46-47	118.46	0.15	1.3	6.00	5.85	0.45	3.18	15.2
14H-5, 46-47	121.46	0.12	1.0	8.20	8.09	0.56	3.15	16.9
15H-1, 46-47	124.96	0.41	3.4	5.28	4.87	0.41	2.94	13.8
15H-3, 46-47	127.96	0.24	2.0	4.48	4.24	0.36	2.03	13.8
15H-5, 46-47	131.02	0.56	4.7	5.11	4.55	0.39	2.62	13.7
17X-1, 40-41	137.40	0.16	1.3	8.37	8.21	0.61	3.42	15.8
17X-3, 45-46	140.41	0.12	1.0	7.18	7.05	0.55	2.71	15.0
17X-5, 46-47	143.42	0.21	1.8	6.08	5.87	0.49	2.90	14.1
18H-1, 46-47	146.46	1.09	9.1	5.32	4.23	0.38	2.37	13.2
18H-3, 46-47	149.46	0.14	1.2	6.56	6.42	0.49	2.85	15.4
18H-5, 46-47	152.41	0.70	5.8	5.60	4.90	0.41	2.61	14.0
19X-1, 46-47	154.96	0.55	4.6	5.88	5.33	0.43	2.89	14.5
19X-3, 46-47	157.96	1.20	10.0	6.19	4.99	0.43	2.09	13.6
19X-5, 46-47	160.96	2.40	20.0	5.38	2.98	0.28	1.74	12.4
20X-1, 46-47	164.56	0.16	1.3	4.44	4.28	0.36	1.83	13.7
20X-5, 46-47	170.56	1.08	9.0	4.88	3.79	0.33	1.70	13.3
21X-1, 46-47	174.26	0.15	1.3	6.83	6.68	0.50	2.78	15.5
22X-1, 45-46	183.95	1.96	16.3	5.71	3.75	0.36	1.82	12.3
22X-4, 45-46	188.45	2.00	16.6	5.97	3.97	0.36	1.87	12.9
23X-1, 45-46	193.55	0.46	3.8	7.80	7.34	0.55	2.42	15.8
23X-4, 45-46	198.05	0.44	3.7	4.41	3.97	0.36	1.70	13.0
24X-1, 45-46	203.25	1.18	9.8	4.39	3.21	0.31	1.37	12.2
24X-4, 45-46	207.75	0.21	1.7	4.84	4.63	0.42	2.17	13.0
25X-1, 45-46	212.85	2.15	17.9	6.67	4.52	0.39	1.85	13.7
25X-5, 45-46	218.85	1.29	10.7	6.04	4.75	0.40	2.06	14.0
26X-2, 45-46	223.95	1.55	12.9	4.92	3.36	0.35	2.03	11.3
Subunit IC - Miocene-Pliocene nannofossil-rich clay								
27X-1, 45-46	231.95	0.77	6.4	4.77	3.99	0.36	1.77	12.9
27X-5, 45-46	237.95	0.87	7.2	5.03	4.16	0.38	1.80	12.8
28X-1, 45-46	241.65	1.32	11.0	5.89	4.57	0.40	2.01	13.4
28X-5, 45-46	247.65	2.14	17.9	5.42	3.28	0.31	1.38	12.3
29X-1, 45-46	251.25	0.90	7.5	5.31	4.42	0.37	1.85	13.8
29X-5, 45-46	257.25	1.88	15.7	5.56	3.68	0.33	1.63	13.1
30X-1, 45-46	260.85	1.79	14.9	5.59	3.80	0.35	1.75	12.6
31X-2, 51-52	272.11	0.80	6.7	6.98	6.18	0.48	2.59	15.1
32X-3, 50-51	283.20	2.51	20.9	5.96	3.45	0.32	1.65	12.4
33X-1, 52-54	289.82	2.89	24.1	5.85	2.96	0.29	1.40	11.8
33X-4, 45-46	294.25	4.15	34.6	6.34	2.19	0.27	1.43	9.5
34X-2, 53-54	301.03	1.01	8.4	4.82	3.80	0.30	1.60	14.6
35X-2, 46-47	310.56	1.55	12.9	4.29	2.74	0.29	1.88	11.2
36X-2, 46-47	319.11	2.16	18.0	5.45	3.29	0.34	1.88	11.3
36X-4, 50-51	322.15	1.83	15.3	4.51	2.68	0.31	1.97	10.2
37X-1, 46-47	328.26	1.52	12.6	4.92	3.41	0.36	1.96	11.0
38X-1, 43-44	337.93	3.30	27.5	5.59	2.29	0.25	1.25	10.8
39X-1, 44-45	347.54	4.51	37.6	7.10	2.58	0.28	1.53	11.0
40X-1, 63-64	357.43	4.68	39.0	6.05	1.37	0.20	2.06	7.8
41X-1, 46-47	366.86	2.67	22.3	5.70	3.03	0.32	1.65	11.2
42X-1, 47-48	376.47	3.36	28.0	6.31	2.95	0.30	1.72	11.4
43X-1, 43-44	386.03	1.77	14.7	4.50	2.73	0.30	2.14	10.8

**Table 11 (continued).**

Core, section, interval (cm)	Depth (mbsf)	IC (wt%)	CaCO <sub>3</sub> (wt%)	TC (wt%)	TOC (wt%)	TN (wt%)	TS (wt%)	C/N (atomic)
Unit II - Miocene clayey nannofossil ooze								
44X-1, 47-48	395.77	4.22	35.1	6.35	2.13	0.24	1.53	10.3
45X-1, 42-43	405.32	3.62	30.2	6.60	2.97	0.29	1.35	11.9
46X-1, 50-51	415.10	5.60	46.7	7.12	1.51	0.20	1.05	8.8
47X-1, 44-46	424.64	3.99	33.2	6.00	2.01	0.23	1.09	10.3
48X-1, 42-44	434.22	2.12	17.7	4.39	2.27	0.27	2.33	9.9
49X-1, 45-47	443.95	1.98	16.5	4.18	2.20	0.24	1.37	10.6

Notes: IC = inorganic carbon; CaCO<sub>3</sub> = calcium carbonate; TC = total carbon; TOC = total organic carbon; TN = total nitrogen; TS = total sulfur; and C/N = carbon/nitrogen ratio. TOC concentrations are calculated from the difference between IC and TC concentrations. C/N ratios are calculated from TOC and TN concentrations and are given as atom/atom ratios.

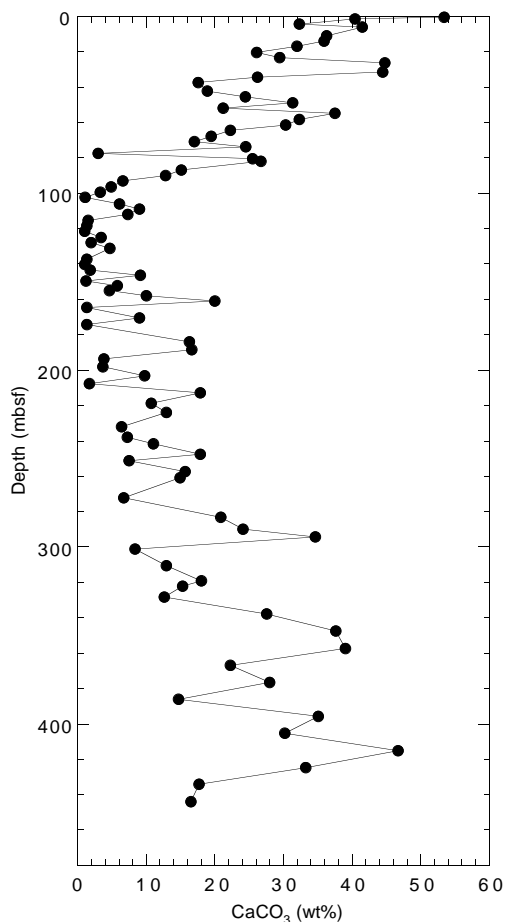


Figure 35. Concentrations of CaCO<sub>3</sub> in sediments from Hole 1081A. Variations reflect light–dark color cycles and different lithologic units.

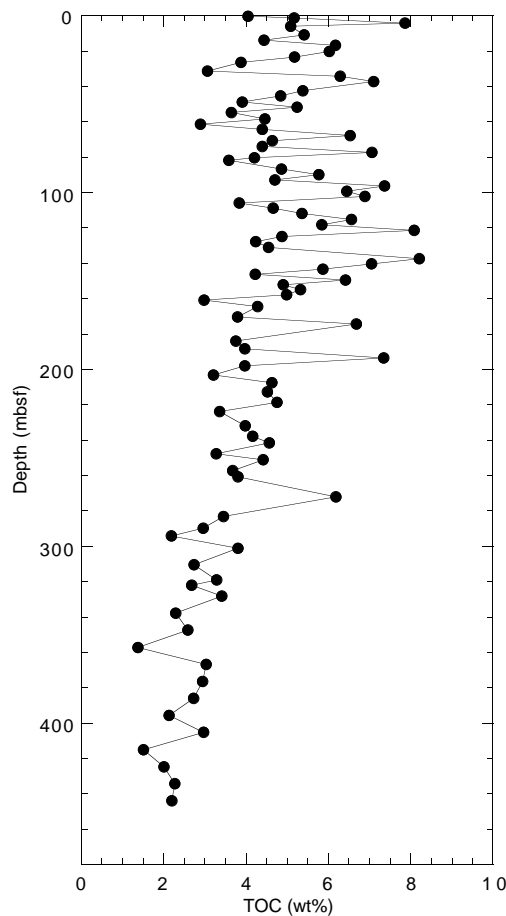


Figure 36. Concentrations of TOC in sediments from Hole 1081A. Variations reflect light–dark color cycles.

### Logging Operations

Hole 1081A was logged with four different tool strings. The first tool string (seismostratigraphy) included the NGT, LSS, DITE, and TLT sondes. The second tool string (lithoporosity) included the NGT, neutron porosity, gamma density, and TLT sondes. The third tool string (FMS, 2 passes) included the NGT, inclinometry, and FMS sondes. The fourth tool string (GHMT) included the NGT, magnetic susceptibility, and vertical component magnetometer sondes. The logs were run uphole from 454 mbsf (total depth) to pipe at 71 mbsf; the two first runs were logged to the seafloor. The natural gamma is the only parameter measurable through the pipe, but it should be interpreted only qualitatively in this interval. For each run, the pipe was set at 101 mbsf and pulled up to ~71 mbsf during logging. The wire-

line logging heave compensator was started immediately upon entering the hole.

### Data Quality and General Results

Hole 1081A is characterized by a very regular hole size (~10-in diameter) from 454 to 290 mbsf (Fig. 46). Although the hole conditions are slightly degraded above 290 mbsf, the hole size retains an average diameter of 10.5 in (with very few enlargements) to 13 in at the top of the logged interval. Consequently, logging measurements are not affected by hole conditions, and records are of excellent quality.

The lithologic succession recovered from Hole 1081A is controlled mainly by changes in the nature and intensity of biogenic production vs. type and amount of detrital input and is characterized by

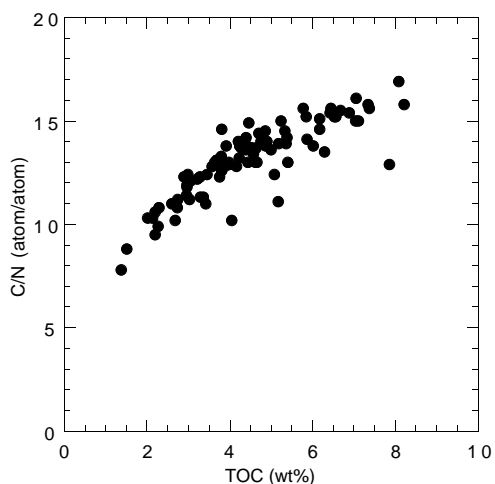


Figure 37. Comparison of organic matter C/N ratios and TOC concentrations of sediments from Hole 1081A. The correspondence between increases in both parameters indicates that preservation of marine organic matter during early diagenesis is important to enhancing the organic carbon richness of sediments on the Walvis Ridge.

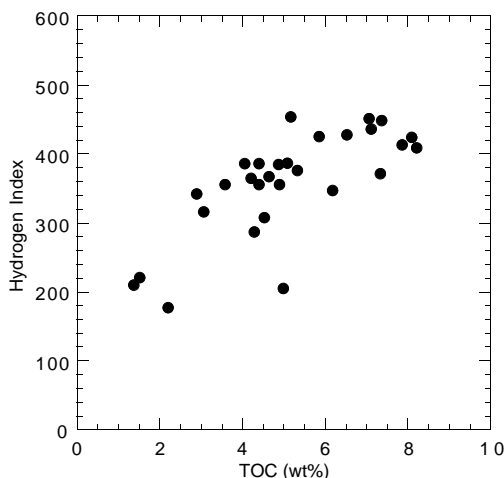


Figure 39. Comparison of Rock-Eval HI values and TOC concentrations of sediments from Hole 1081A. The correspondence between increases in both parameters indicates that preservation of marine organic matter is important to enhancing the organic carbon richness of sediments on the Walvis Ridge.

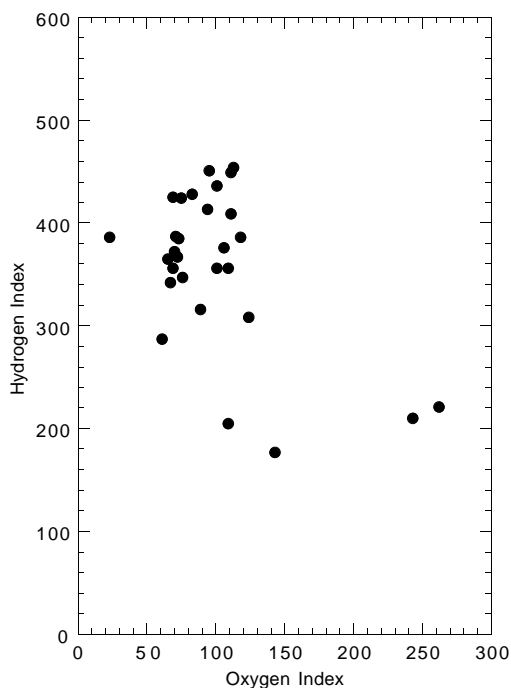


Figure 38. Rock-Eval Van Krevelen-type diagram of sediments from Hole 1081A. Organic matter appears to be type II algal material that has been variably oxidized. HI is in milligrams of hydrocarbons per gram of organic carbon; OI is in milligrams of CO<sub>2</sub> per gram of organic carbon.

large changes in sediment composition and compaction, which should be reflected in the log physical properties measurements. The lithostratigraphic boundaries defined from core observation and smear-slide studies (see “Lithostratigraphy” section, this chapter) partially fit with the main features observed in the downhole measurements. The boundary between Subunits ID and IC near 390 mbsf is identified in the log data as a sharp increase in gamma-ray intensity (K and thorium [Th]), magnetic susceptibility, and resistivity at 400 mbsf (Fig. 46). Similarly, the sharply increased opal content of litho-

**Table 12. Results of Rock-Eval pyrolysis analyses of sediments from Hole 1081A.**

Core, section, interval (cm)	Depth (mbsf)	TOC (wt%)	S <sub>1</sub>	S <sub>2</sub>	S <sub>3</sub>	T <sub>max</sub> (°C)	HI	OI
175-1081A-								
1H-1, 47-48	0.47	4.05	1.78	15.66	4.60	417	386	23
2H-1, 46-47	1.46	5.17	3.10	23.49	4.90	411	454	113
2H-3, 46-47	4.46	7.86	8.13	32.54	5.63	405	413	94
2H-4, 46-47	5.96	5.08	2.19	19.66	4.53	411	387	71
5H-2, 46-47	31.46	3.06	0.64	9.70	3.10	415	316	89
5H-6, 46-47	37.36	7.11	1.90	31.07	4.77	413	436	101
8H-3, 46-47	61.46	2.89	0.67	9.90	2.93	412	342	67
8H-5, 46-47	64.36	4.40	1.03	15.68	3.68	418	356	101
9H-1, 46-47	67.96	6.53	1.62	27.99	4.75	416	428	83
9H-3, 46-47	70.96	4.64	0.96	17.05	5.48	414	367	72
9H-5, 46-47	73.86	4.40	1.10	17.00	4.18	413	386	118
10H-1, 46-47	77.46	7.06	2.59	31.89	4.59	401	451	95
10H-3, 46-47	80.46	4.21	0.88	15.38	4.60	415	365	65
10H-4, 46-47	81.86	3.58	0.71	12.77	4.00	415	356	109
12H-1, 46-47	96.46	7.37	3.44	33.14	5.13	391	449	111
14H-3, 46-47	118.46	5.85	2.28	24.88	4.41	394	425	69
14H-5, 46-47	121.46	8.09	2.40	34.36	5.92	393	424	75
15H-1, 46-47	124.96	4.87	1.38	18.77	5.42	401	385	73
17X-1, 40-41	137.40	8.21	4.04	33.64	5.70	392	409	111
18H-5, 46-47	152.41	4.90	1.81	17.46	5.21	403	356	69
19X-1, 46-47	154.96	5.33	2.14	20.08	5.84	401	376	106
19X-3, 46-47	157.96	4.99	1.77	10.23	5.86	396	205	109
20X-1, 46-47	164.56	4.28	1.06	12.31	2.63	404	287	61
23X-1, 45-46	193.55	7.34	2.03	27.33	5.16	402	372	70
25X-1, 45-46	212.85	4.52	0.71	13.93	5.63	427	308	124
31X-2, 51-52	272.11	6.18	0.92	21.49	4.75	414	347	76
40X-1, 63-64	357.43	1.37	0.21	2.89	3.34	421	210	243
46X-1, 50-51	415.10	1.51	0.31	3.35	3.96	415	221	262
49X-1, 45-47	443.95	2.20	0.37	3.90	3.16	416	177	143

Notes: TOC = total organic carbon; HI = hydrogen index; and OI = oxygen index. Units of the various Rock-Eval parameters are given in the “Organic Geochemistry” section of the “Explanatory Notes” chapter (this volume).

logic Subunit IB is reflected in the downhole measurements at ~190 mbsf. This depth corresponds to the LO of nannofossils, whereas the Subunit IC/IB boundary at 230 mbsf was established by the FO of diatoms (see “Biostratigraphy and Sedimentation Rates” section, this chapter). The high uranium (U) content (5–11 ppm) suggests a high content of organic carbon. The U content is relatively low at the bottom of Subunit IB.

Besides agreement with lithologic boundaries, the physical measurements show two specific changes that are independent of the observed lithology. At 340 mbsf, the velocity, density, and resistivity logs exhibit a slight decrease uphole, which may result from differ-

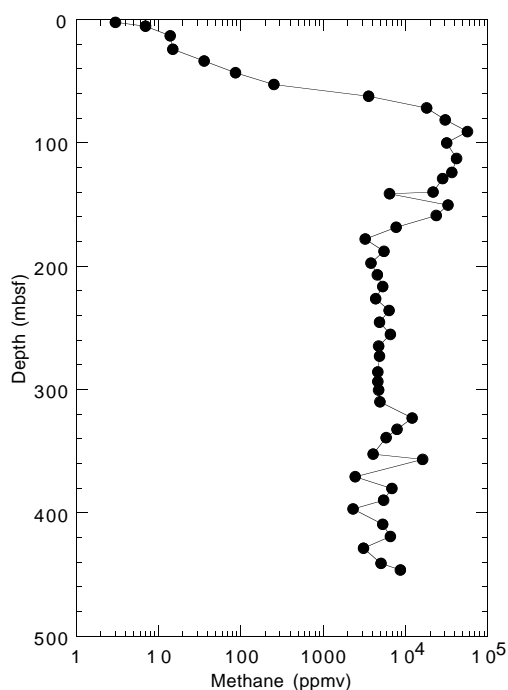


Figure 40. Headspace methane concentrations in sediments from Hole 1081A.

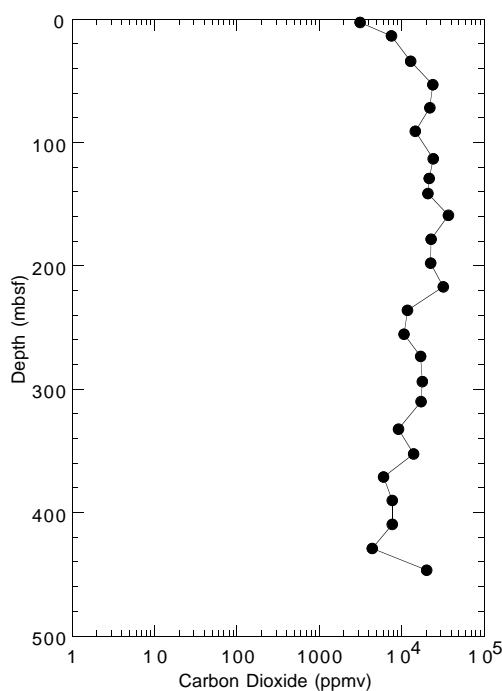


Figure 41. Headspace CO<sub>2</sub> concentrations in sediments from Hole 1081A.

ences in diagenesis. All three parameters show an increase downhole caused by progressive compaction of the sediment. At 275 mbsf, the measurements show sharp increases in gamma-ray intensity and magnetic susceptibility, possibly caused by a change in clay content.

Twenty-five layers with anomalous physical properties were identified (Fig. 46), characterized by high velocity (5 km/s), resistivity (2 Ωm), and density (2.4 g/cm<sup>3</sup>) and were tentatively described as dolomitic layers. Some of them could be observed in the cores (see "Lithostratigraphy" section, this chapter) because of incomplete re-

Table 13. Results of headspace gas analyses of sediments from Hole 1081A.

Core, section, interval (cm)	Depth (mbsf)	C <sub>1</sub> (ppmv)	CO <sub>2</sub> (ppmv)	C <sub>2</sub> = (ppmv)	C <sub>2</sub> (ppmv)	C <sub>3</sub> = (ppmv)	C <sub>3</sub> (ppmv)	C <sub>1</sub> /C <sub>2</sub>
175-1081A-								
2H-2, 0-5	2.50	3	3,121					
2H-4, 0-5	5.50	7			0.1			122
3H-3, 0-5	13.40	14	7,560	0.3	0.4			36
4H-4, 0-5	24.40	15			0.3			44
5H-4, 0-5	33.90	36	12,879	0.2	0.9			40
6H-4, 0-5	43.40	87		0.2	1.7			51
7H-4, 0-5	52.90	252	24,148	0.0	1.6			158
8H-4, 0-5	62.40	3,602		0.1	2.0			1,801
9H-4, 0-5	71.90	18,258	21,872	0.1	0.1			182,580
10H-4, 0-5	81.40	30,671		0.2	5.0		0.9	6,134
11H-4, 0-5	90.90	57,166	14,839	0.3	9.9		2.5	5,774
12H-4, 0-5	100.40	31,856		0.6	9.0		3.4	3,540
13H-6, 0-5	113.05	42,073	24,404	0.3	8.5		3.0	4,950
14H-7, 0-5	124.00	36,868		0.4	9.4		4.2	3,922
15H-4, 0-5	129.04	28,578	21,694	0.5	9.4		4.6	3,040
16H-7, 0-5	140.21	21,705		0.4	7.5		3.6	2,894
17X-4, 0-5	141.46	6,463	20,914	0.3	3.9		2.0	1,657
18H-4, 0-5	150.45	32,924		0.6	9.6		4.4	3,430
19X-4, 0-5	159.00	23,623	37,330	0.3	10.0		4.9	2,362
20X-4, 0-5	168.60	7,721		0.3	4.6		2.9	1,678
21X-4, 0-5	178.30	3,252	22,832	0.2	2.0		1.3	1,626
22X-4, 0-5	188.00	5,515		0.3	4.5		2.8	1,226
23X-4, 0-5	197.60	3,844	22,566	0.4	4.7		3.3	818
24X-4, 0-5	207.30	4,597		0.3	5.2		3.4	884
25X-4, 0-5	216.90	5,294	31,951	0.4	5.9		4.5	897
26X-4, 0-5	226.50	4,365		0.4	4.7		3.1	929
27X-4, 0-5	236.00	6,380	11,876	1.3	13.0	0.9	9.8	491
28X-4, 0-5	245.70	4,892		0.4	8.6		6.1	569
29X-4, 0-5	255.30	6,573	10,735	0.5	10.7		7.9	614
30X-4, 0-5	264.90	4,741		0.6	8.2		5.9	578
31X-3, 0-5	273.10	4,889	17,050	0.4	10.0		7.1	489
32X-5, 0-5	285.70	4,635		0.3	7.4		5.3	626
33X-4, 0-5	293.80	4,644	17,938	0.2	4.5		3.6	1,032
34X-2, 0-5	300.50	4,765		0.2	6.5		1.7	733
35X-2, 0-5	310.10	4,932	17,380	0.2	8.8	0.1	6.2	560
36X-5, 0-5	323.15	12,146		0.9	21.9		14.9	555
37X-4, 0-5	332.30	7,925	9,196	0.9	9.4	0.4	9.2	843
38X-2, 0-5	339.00	5,834		1.3	10.4		10.9	561
39X-5, 0-5	352.42	4,092	14,001	0.3	4.3	0.1	3.6	952
40X-1, 0-5	356.80	16,290		0.2	6.6		3.7	2,468
41X-4, 0-5	370.90	2,461	6,025	1.0	6.1	0.1	7.6	403
42X-4, 0-5	380.50	6,870		0.7	16.6		17.8	414
43X-4, 0-5	390.10	5,417	7,713	2.0	23.8		31.6	228
44X-2, 0-5	396.80	2,312		0.9	6.4		9.5	361
45X-4, 0-5	409.40	5,290	7,743	1.6	13.6	0.2	18.4	389
46X-4, 0-5	419.10	6,565		0.9	10.0		11.4	656
47X-4, 0-5	428.70	3,129	4,422	1.1	9.4		13.5	333
48X-6, 0-5	441.30	5,035		1.8	10.4	0.8	13.7	484
49X-3, 0-5	446.50	8,698	20,145	0.5	13.0		15.5	669

Notes: C<sub>1</sub> = methane; CO<sub>2</sub> = carbon dioxide; C<sub>2</sub>= = ethene; C<sub>2</sub> = ethane; C<sub>3</sub>= = propene; and C<sub>3</sub> = propane. Dominance of C<sub>1</sub> over C<sub>2</sub> indicates that the gases originate from in situ microbial degradation of organic matter.

covery. All 25 high-resistivity (dolomitic) layers are clearly identified on FMS images that allow for the positions and thicknesses of the layers to be determined (Fig. 47). Dolomitic layers are present in the entire logged interval but are particularly concentrated between 360 and 340 mbsf and 320 and 300 mbsf. The deeper of these concentration levels appears to be related to the changes in physical parameters observed at 340 mbsf (Fig. 46).

The temperature tool measures borehole fluid temperature, which can be used to estimate downhole thermal gradients provided that the data reflect borehole, rather than in situ formation, temperature. The results (Fig. 48) suggest a downhole thermal gradient of 22°C/km, an estimate that is low because of the cooling effect of circulation during drilling.

### Log-Core Correlations

The core MST and log measurements of natural gamma-ray intensity are similar, but fine-scale (<1 m) correlations between the core and log data sets are difficult because of the lower vertical resolution of the log data and because of core disturbance (Fig. 49). XCB coring disturbance particularly affected the volume-dependent MST core

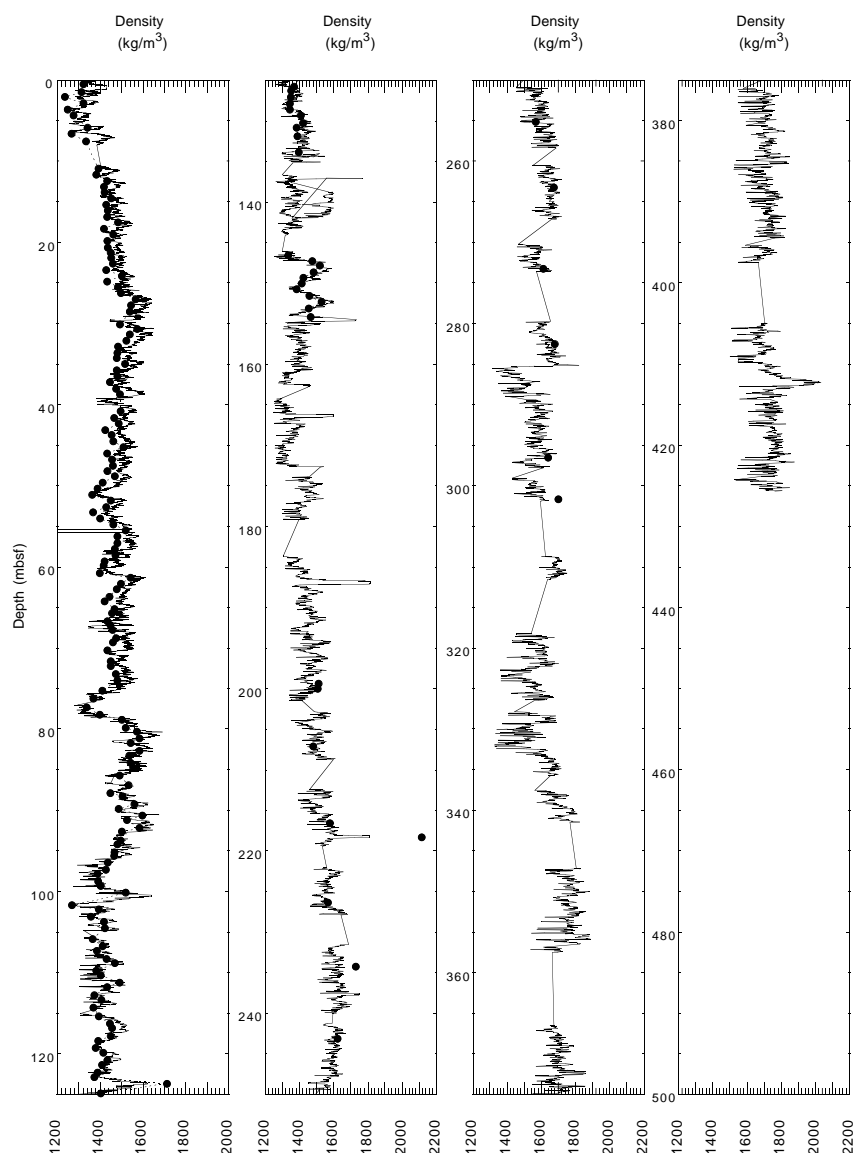


Figure 42. Gravimetric wet bulk density (solid circles) compared with GRAPE density (solid line) at Hole 1081A.

measurements of gamma-ray activity. At Hole 1081A, log depth is similar to core depth. Core data are recorded in counts per second (cps), whereas log data are presented in API (Oil Industry Standard) units. The switch from APC to XCB coring (at 137 mbsf), the concomitant appearance of sediment slurry in core liners, and the reduced recovery adversely affect the quality of the gamma-ray measurements on the core. The intervals of poor core recovery correspond to low gamma-ray intensity in the log, which suggests that XCB coring had problems recovering microfossil-rich sediments.

#### REFERENCES

- Barron, J.A., 1985. Miocene to Holocene planktic diatoms. In Bolli, H.M., Saunders, J.B., and Perch-Nielsen, K. (Eds.), *Plankton Stratigraphy*: Cambridge (Cambridge Univ. Press), 763–809.
- , 1995. High-resolution diatom paleoclimatology of the middle part of the Pliocene of the Northwest Pacific. In Rea, D.K., Basov, I.A., Scholl, D.W., and Allan, J.F. (Eds.), *Proc. ODP, Sci. Results*, 145: College Station, TX (Ocean Drilling Program), 43–53.
- Berger, W.H., and Wefer, G., 1996. Expeditions into the past: paleoceanographic studies in the South Atlantic. In Wefer, G., Berger, W.H., Siedler, G., Webb, D.J. (Eds.), *The South Atlantic: Present and Past Circulation*: Berlin (Springer-Verlag), 363–410.
- Berggren, W.A., Kent, D.V., Swisher, C.C., III, and Aubry, M.-P., 1995. A revised Cenozoic geochronology and chronostratigraphy. In Berggren, W.A., Kent, D.V., Aubry, M.-P., and Hardenbol, J. (Eds.), *Geochronology, Time Scales and Global Stratigraphic Correlation*. Spec. Publ.— Soc. Econ. Paleontol. Mineral. (Soc. Sediment. Geol.), 54:129–212.
- Bleil, U., and Shipboard Scientific Party, 1996. Report and preliminary results of METEOR cruise M34/1, Capetown-Walvis Bay, 3.1.1996–26.1.1996. *Ber. Fachber. Geowiss., Univ. Bremen*, 77.
- Bolli, H.M., Ryan, W.B.F., et al., 1978. *Init. Repts. DSDP*, 40: Washington (U.S. Govt. Printing Office).
- Caulet, J.-P., 1991. Radiolarians from the Kerguelen Plateau, Leg 119. In Barron, J., Larsen, B., et al., *Proc. ODP, Sci. Results*, 119: College Station, TX (Ocean Drilling Program), 513–546.
- Claypool, G.E., and Kvenvolden, K.A., 1983. Methane and other hydrocarbon gases in marine sediment. *Annu. Rev. Earth Planet. Sci.*, 11:299–327.
- Clement, B.M., and Kent, D.V., 1986. Geomagnetic polarity transition records from five hydraulic piston core sites in the North Atlantic. In Ruddiman, W.F., Kidd, R.B., Thomas, E., et al., *Init. Repts. DSDP*, 94: Washington (U.S. Govt. Printing Office), 831–852.
- Cragg, B.A., Harvey, S.M., Fry, J.C., Herbert, R.A., and Parkes, R.J., 1992. Bacterial biomass and activity in the deep sediment layers of the Japan Sea, Hole 798B. In Pisciotto, K.A., Ingle, J.C., Jr., von Breyman, M.T.,

- Barron, J., et al., *Proc. ODP, Sci. Results.*, 127/128 (Pt. 1): College Station, TX (Ocean Drilling Program), 761–776.
- Diester-Haass, L., 1985. Late Quaternary sedimentation on the eastern Walvis Ridge, southeast Atlantic (HPC 532 and four piston cores). *Mar. Geol.*, 65:145–189.
- , 1988. Sea-level changes, carbonate dissolution and history of the Benguela Current in the Oligocene–Miocene off SW Africa (DSDP Site 362, Leg 40). *Mar. Geol.*, 79:213–242.
- Diester-Haass, L., Meyers, P.A., and Rothe, P., 1990. The Benguela Current: glacial/interglacial fluctuations during its Miocene northward migration across the Walvis Ridge. *Paleoceanography*, 5:685–707.
- Diester-Haass, L., and Rothe, P., 1987. Plio–Pleistocene sedimentation on the Walvis Ridge, SE Atlantic (DSDP Leg 75, Site 532): influence of surface currents, carbonate dissolution and climate. *Mar. Geol.*, 77:53–85.
- Dingle, R.V., and Robson, S.H., 1992. Southwestern Africa continental rise: structural and sedimentary evolution. In Poag, C.W., and Graciansky, P.C. (Eds.), *Geologic Evolution of Atlantic Continental Rises*: New York (Van Nostrand), 62–76.
- Eisma, D., and Van der Gaast, S.J., 1971. Determination of opal in marine sediments by X-ray diffraction. *Neth. J. Sea Res.*, 5:382–389.
- Emerson, S., and Hedges, J.I., 1988. Processes controlling the organic carbon content of open ocean sediments. *Paleoceanography*, 3:621–634.
- Emery, K.O., and Uchupi, E., 1984. *The Geology of the Atlantic Ocean*: New York (Springer-Verlag).
- Fenner, J.M., 1991. Late Pliocene–Quaternary quantitative diatom stratigraphy in the Atlantic sector of the Southern Ocean. In Ciesielski, P.F., Kristoffersen, Y., et al., *Proc. ODP, Sci. Results*, 114: College Station, TX (Ocean Drilling Program), 97–121.
- Gartner, S., 1977. Calcareous nannofossil biostratigraphy and revised zonation of the Pleistocene. *Mar. Micropaleontol.*, 2:1–25.
- Gerrard, I., and Smith, G.C., 1984. Post-Paleozoic succession and structures of the southwestern African continental margin. In Watkins, J.S., and Drake, C.L. (Eds.), *Studies in Continental Margin Geology*. AAPG Mem., 34:49–74.
- Hartl, P., and Tauxe, L., 1996. A precursor to the Matuyama/Brunhes transition: field instability as recorded in pelagic sediments. *Earth Planet. Sci. Lett.*, 138:121–135.
- Hay, W.W., and Brock, J.C., 1992. Temporal variation in intensity of upwelling off southwest Africa. In Summerhayes, C.P., Prell, W.L., and Emeis, K.C. (Eds.), *Upwelling Systems: Evolution Since the Early Miocene*. Geol. Soc. Spec. Publ. London, 64:463–497.
- Hay, W.W., Sibuet, J.-C., et al., 1984. *Init. Repts. DSDP*, 75: Washington (U.S. Govt. Printing Office).
- Kennett, J.P., and Srinivasan, M.S., 1983. *Neogene Planktonic Foraminifera: A Phylogenetic Atlas*: Stroudsburg, PA (Hutchinson Ross).
- Lazarus, D., 1992. Antarctic Neogene radiolarians from the Kerguelen Plateau, Legs 119 and 120. In Wise, S.W., Jr., Schlich, R., et al., *Proc. ODP, Sci. Results*, 120: College Station, TX (Ocean Drilling Program), 785–809.
- Little, M.G., Schneider, R.R., Kroon, D., Price, B., Bickert, T., and Wefer, G., 1997. Rapid paleoceanographic changes in the Benguela Upwelling System for the last 160,000 years as indicated by abundances of planktonic foraminifera. *Paleogeogr., Paleoclimatol., Palaeoecol.*, 130:135–161.
- Martini, E., 1971. Standard Tertiary and Quaternary calcareous nannoplankton zonation. In Farinacci, A. (Ed.), *Proc. 2nd Int. Conf. Planktonic Microfossils Roma*: Rome (Ed. Tecnosci.), 2:739–785.
- Meyers, P.A., 1994. Preservation of elemental and isotopic source identification of sedimentary organic matter. *Chem. Geol.*, 144:289–302.
- , 1997. Organic geochemical proxies of paleoceanographic, paleolimnologic, and paleoclimatic processes. *Org. Geochem.*, 27:213–250.
- Meyers, P.A., and Brassell, S.C., 1985. Biogenic gases in sediments deposited since Miocene times on the Walvis Ridge, South Atlantic Ocean. In Caldwell, D.E., Brierley, J.A., and Brierley, C.L. (Eds.), *Planetary Ecology*: New York (Van Nostrand Reinhold), 69–80.
- Meyers, P.A., and Shaw, T.J., 1996. Organic matter accumulation, sulfate reduction, and methanogenesis in Pliocene–Pleistocene turbidites on the Iberian Abyssal Plain. In Whitmarsh, R.B., Sawyer, D.S., Klaus, A., and Masson, D.G. (Eds.), *Proc. ODP, Sci. Results*, 149: College Station, TX (Ocean Drilling Program), 705–712.
- Millero, F.J., and Sohn, M.L., 1992. *Chemical Oceanography*: Boca Raton (CRC Press).
- Moore, T.C., Jr., 1995. Radiolarian stratigraphy, Leg 138. In Pisias, N.G., Mayer, L.A., Janecek, T.R., Palmer-Julson, A., and van Andel, T.H. (Eds.), *Proc. ODP, Sci. Results*, 138: College Station, TX (Ocean Drilling Program), 191–232.
- Motoyama, I., 1996. Late Neogene radiolarian biostratigraphy in the subarctic Northwest Pacific. *Micropaleontology*, 42:221–260.
- Oberhänsli, H., 1991. Upwelling signals at the northeastern Walvis Ridge during the past 500,000 years. *Paleoceanography*, 6:53–71.
- Okada, H., and Bukry, D., 1980. Supplementary modification and introduction of code numbers to the low-latitude coccolith biostratigraphic zonation (Bukry, 1973; 1975). *Mar. Micropaleontol.*, 5:321–325.
- Peters, K.E., 1986. Guidelines for evaluating petroleum source rock using programmed pyrolysis. *AAPG Bull.*, 70:318–329.
- Quidelleur, X., and Valet, J.-P., 1996. Geomagnetic changes across the last reversal recorded in lava flow from La Palma, Canary Islands. *J. Geophys. Res.*, 101:13755–13773.
- Sanfilippo, A., Westberg-Smith, M.J., and Riedel, W.R., 1985. Cenozoic radiolaria. In Bolli, H.M., Saunders, J.B., and Perch-Nielsen, K. (Eds.), *Plankton Stratigraphy*: Cambridge (Cambridge Univ. Press), 631–712.
- Shannon, L.V., and Nelson, G., 1996. The Benguela: large scale features and processes and system variability. In Wefer, G., Berger, W.H., Siedler, G., Webb, D.J. (Eds.), *The South Atlantic: Present and Past Circulation*: Berlin (Springer-Verlag), 163–210.
- Shipboard Scientific Party, 1990. Site 767. In Rangin, C., Silver, E.A., von Breymann, M.T., et al., *Proc. ODP, Init. Repts.*, 124: College Station, TX (Ocean Drilling Program), 121–193.
- , 1996. Explanatory notes. In Comas, M.C., Zahn, R., Klaus, A., et al., *Proc. ODP, Init. Repts.*, 161: College Station, TX (Ocean Drilling Program), 21–49.
- , in press. Site 1071. In Christie-Blick, N., Austin, J.A., et al., *Proc. ODP, Init. Repts.*, 174A: College Station, TX (Ocean Drilling Program).
- Sibuet, J.-C., Hay, W.W., Prunier, A., Montadert, L., Hinz, K., and Fritsch, J., 1984. The eastern Walvis Ridge and adjacent basins (South Atlantic): morphology, stratigraphy and structural evolution in the light of the results of Legs 40 and 75. In Hay, W.W., Sibuet, J.-C., et al., *Init. Repts. DSDP*, 75: Washington (U.S. Govt. Printing Office), 483–508.
- Weaver, P.P.E., 1993. High resolution stratigraphy of marine Quaternary sequences. In Hailwood, E.A., and Kidd, R.B. (Eds.), *High Resolution Stratigraphy*. Geol. Soc. Spec. Publ. London, 70:137–153.

Ms 175IR-109

**NOTE: Core-description forms (“barrel sheets”) and core photographs can be found in Section 4, beginning on page 581. Forms containing smear-slide data and shore-based log processing data can be found on CD-ROM. See Table of Contents for materials contained on CD-ROM.**

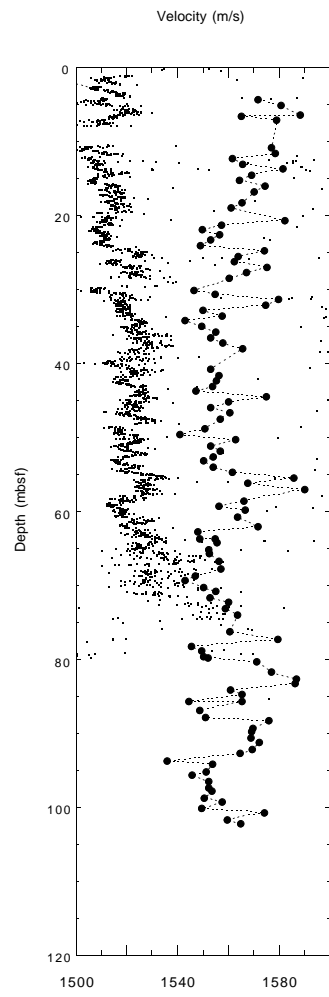


Figure 43. Discrete velocity profile (solid circles) compared with MST velocity data (dots) measured at Hole 1081A.

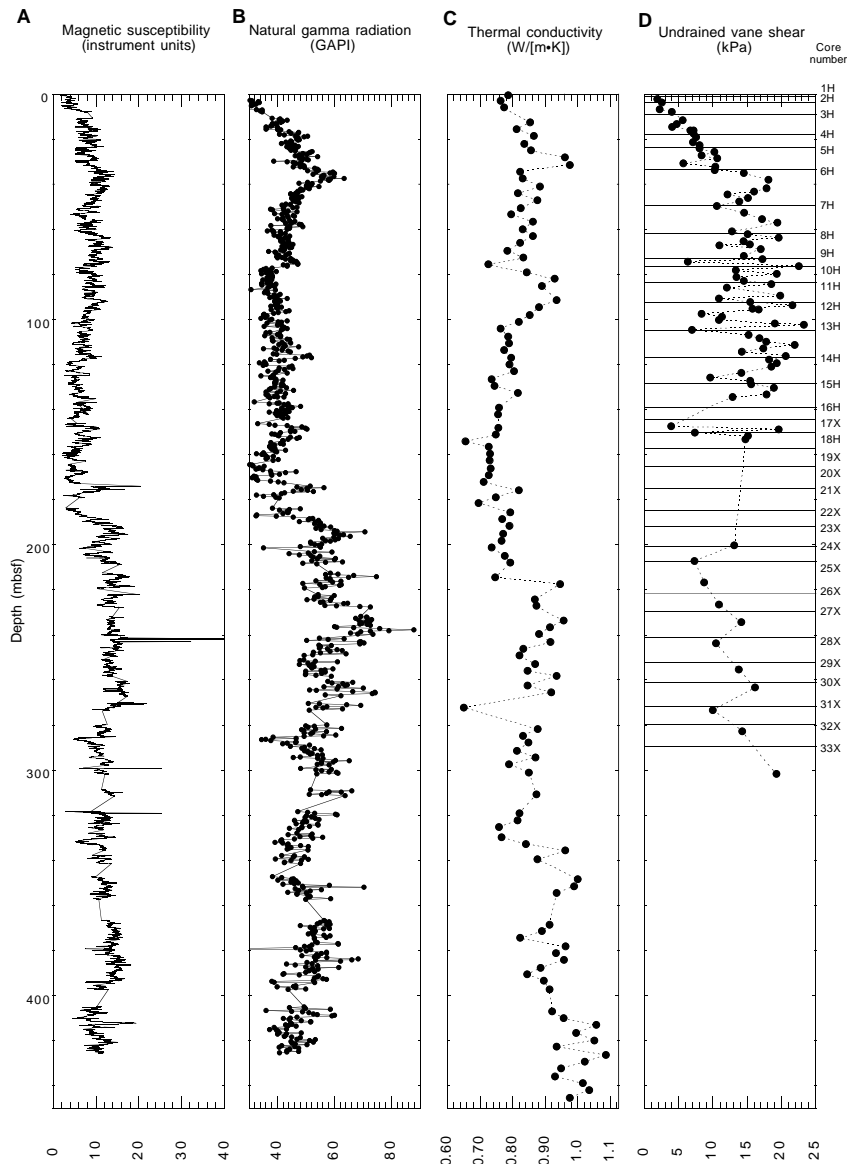


Figure 44. Comparison of (A) magnetic susceptibility with (B) natural gamma radiation from MST measurements, and discrete values of (C) thermal conductivity and (D) undrained vane shear strength at Hole 1081A.

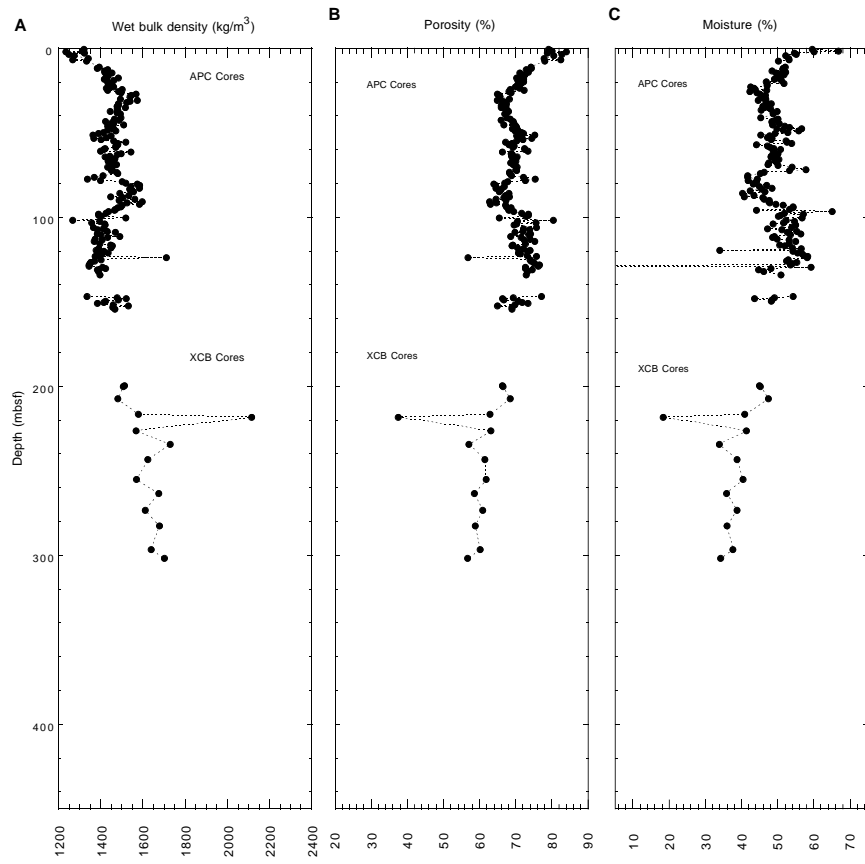


Figure 45. Plots of (A) gravimetric wet bulk density, (B) porosity, and (C) moisture content derived from index properties measurements for Hole 1081A.

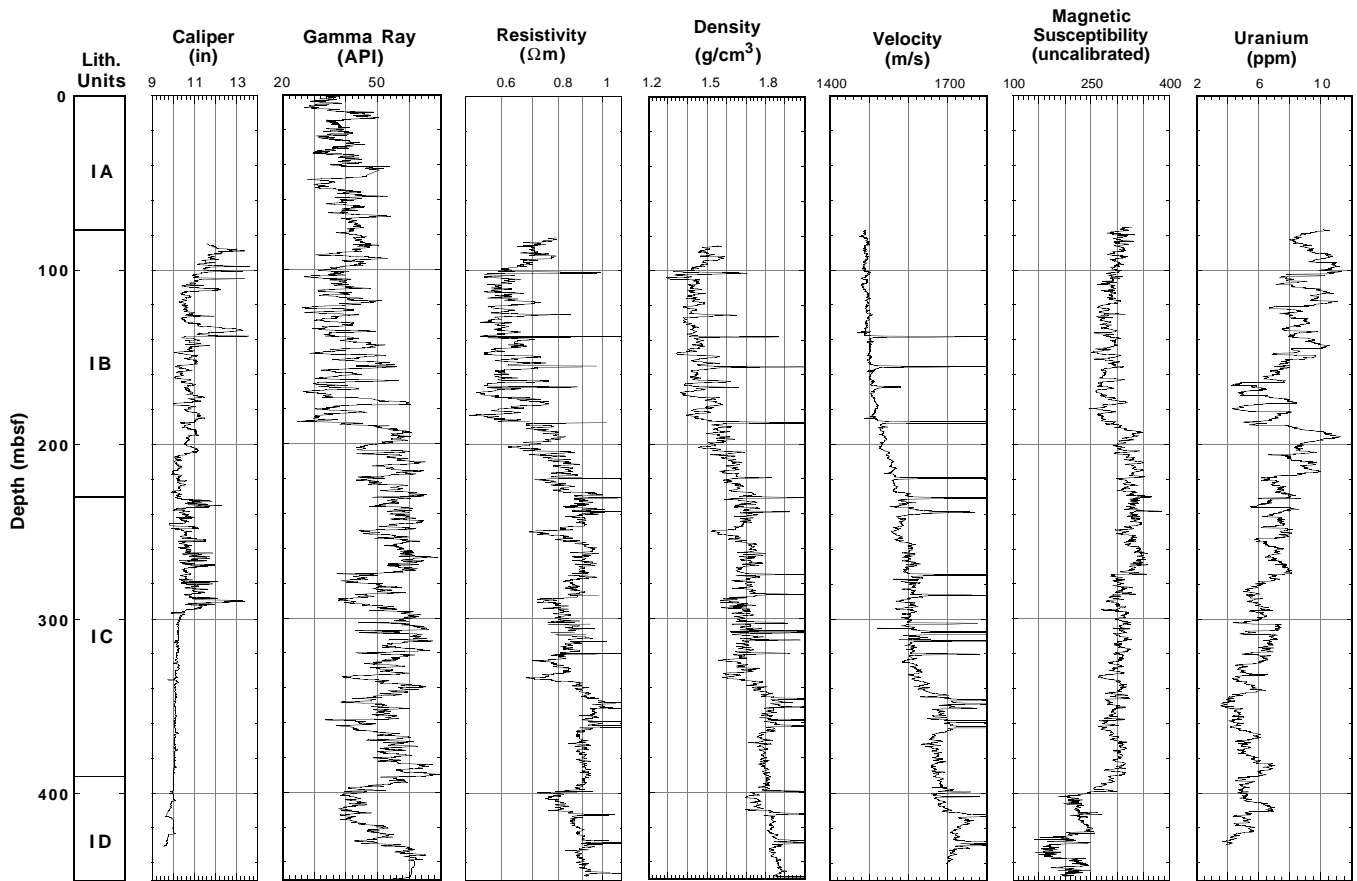


Figure 46. Downhole logs of caliper, natural gamma-ray, resistivity, velocity, density, magnetic susceptibility, and uranium content for Hole 1081A.

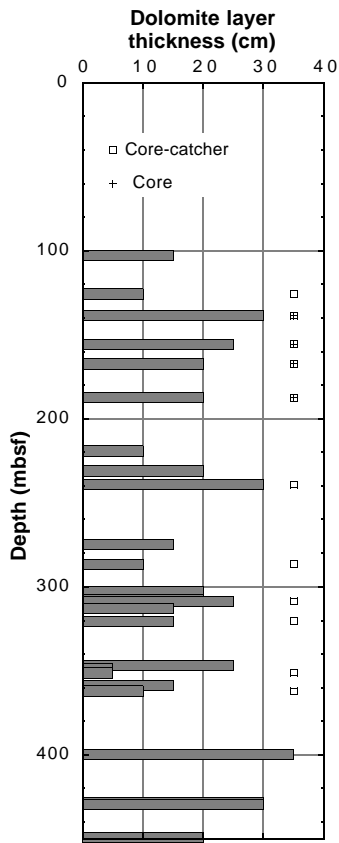


Figure 47. Thickness of the dolomitic layers with depth, as identified from logs for Hole 1081A. Core and core-catcher observations also are mentioned.

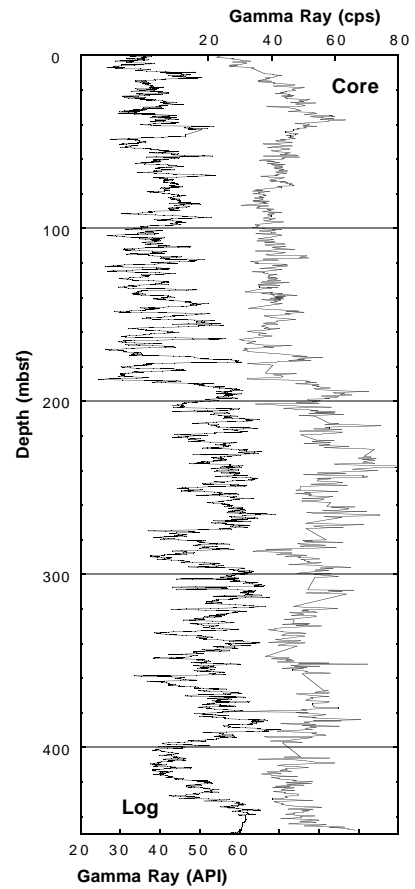


Figure 49. Comparison of core (MST) and log natural gamma data for Hole 1081A.

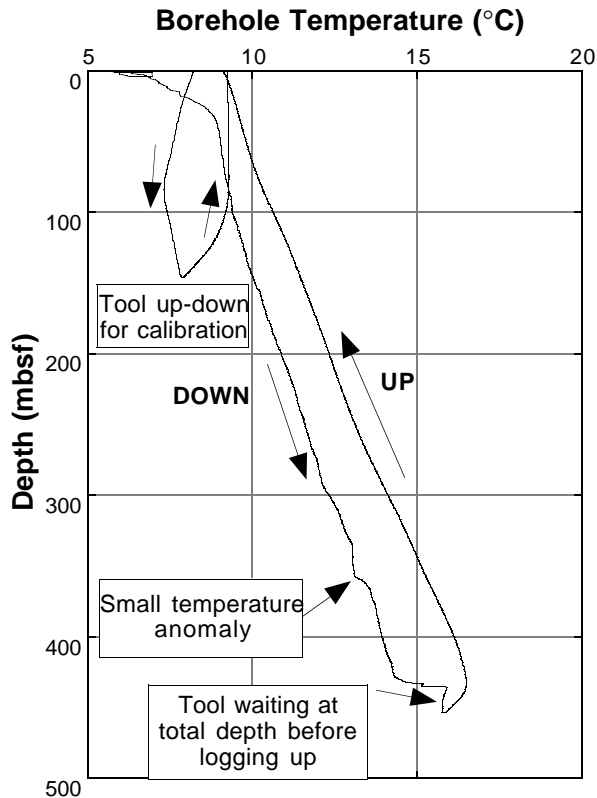


Figure 48. Borehole temperature measurements for Hole 1081A.